FUNCTIONAL AND STRUCTURAL MAGNETIC RESONANCE IMAGING OF HUMANS AND MACAQUES

Thesis by

KYLE ALAN BERNHEIM

In Partial Fulfillment of the Requirements for the

degree of

Doctor of Philosophy

CALIFORNIA INSTITUTE OF TECHNOLOGY

Pasadena, California

2004

(Defended May 14, 2004)

DEDICATION

For Harty, Dante and the rest of the real heroes.

ACKNOWLEDGEMENTS

My first thanks must and do go to my friend and mentor David Dubowitz. David's teachings were important in the fact that the scientific background of MRI and fMRI in which he instructed me were tempered always with the common sense and experience that came from his years as a radiologist. Indeed, there is much about him that I can only hope to carry with me through my future, both in career and private life. As a scientist he gave me knowledge; as a friend he gave me advice. Here's to you, Dubie.

I thank Richard Andersen, my advisor, for taking me on as a young second year medical student and giving me the chance to perform in his laboratory. The atmosphere and camaraderie he welcomed me to was, simply, fantastic. I can only hope my further experiences in science will be so fine. With his help and guidance I was able to select a further group of gentlemen: Igor Fineman, Scott Fraser, Mark Konishi and Shin Shimojo – my thesis committee. While thanking them before my defense may be premature, I can safely say they were, all of them, fine role models for a young scientist.

I thank all the members of the Andersen lab, past and present, for all the little niceties I've experienced over the years. Thanks to the quality of each and every one of you, we became something great and fine – something to be remembered in all our lives. Thank you Betty, Kelsie and Lea; Cierina and Tessa, and my comrade Viktor for all your work in front and behind the scenes. Thank you Hans, for the tea and long talks. Thank you Boris, for the

fun and the games. Thank you Bijan, for insight and wit. Thank you Daniella and Brian, Marina and Igor, for smiles that sweetened the days. Thank you Brian (another!) and Sam, Mike and Grant, Dan and Jason, Rodrigo and Liz, Bradley and Chris, Shauming and Zoltan, Alex – and Alex! – whether in lab, or across the hall at SFN, we'll always remember. We were the Andersen Lab.

ABSTRACT

Magnetic resonance imaging (MRI) is a technique which finds use in the neurosciences both as an anatomical and functional localization tool. The traditional uses of MRI for structural analysis, such as are commonly found in medicine, can be adapted to serve in place of histological studies for identifying areas of interest in the cortex. Functional MRI (fMRI) is a rapidly developing tangent of MRI which can be used alone or in tandem with classical electrophysiological experiments to investigate neural activity. Although developed intensely for clinical and scientific studies in human subjects, MRI and fMRI have been used increasingly in the non-human primate. This document contains work exemplifying the use of fMRI in both species and methods for pre- and post-surgical anatomical MRI in the non-human primate. Serving as a solid foundation for learning the principles of block-design fMRI, a classic visual illusion, the motion aftereffect, is studied in the human by means of a hemifield visual stimulus using conventional blood oxygen level dependent (BOLD) fMRI. Primary response and levels of motion aftereffect are analyzed in visual cortex, areas pMT and pMST. A novel use of iron oxide nanoparticles as an intravascular contrast agent in the non-human primate is investigated as a method of boosting fMRI contrast, yielding an ultimate gain in contrast-to-noise at the expense of temporal resolution. While anatomical imaging served as a necessary tool for the localization of functional response in the human, further novel techniques were investigated in the non-human primate. A technique for MRI-guided implantation of multiple electrode arrays is considered, to aid the localization of sites of interest in the cortex. The use of

MRI as a replacement for histological preparations for purposes of reconstructing electrode penetration sites is documented. These studies exist to aid in bridging the gap between human and non-human MRI and fMRI. Further application of these principles could be extended to the eventual placement of intracortical recording devices in the human, to benefit a patient population needing devices such as a neural prosthesis.

TABLE OF CONTENTS

LIST OF FIGURES

Number Page

LIST OF TABLES

Number Page

CHAPTER I: Introduction

I.1 MAGNETIC RESONANCE IMAGING

The essence of magnetic resonance imaging (MRI) is spectroscopy, specifically nuclear magnetic resonance (NMR) spectroscopy. The technique as a whole has had enormous influence and has generated more than one Nobel prize. From the first development in NMR awarded to Felix Bloch (Bloch, 1946) and Edward Mills Purcell (Bloembergen, 1948) in the 1952 Physics prize to the latest recognition of Paul C. Lauterbur (Lauterbur, 1986) and Sir Peter Mansfield (Mansfield and Maudsley, 1977) in the 2003 prize for Physiology or Medicine. At its core, NMR utilizes the absorption and emission of radiofrequency electromagnetic radiation (RF) by nuclei made susceptible by placement in a magnetic field. If the nuclei of interest has a non-zero quantum of nuclear spin, its placement into a magnetic field will cause it to align either with or against the applied field, as it approximates a rotating charge. This applied magnetic field then forces the particular nuclei of interest into one of several energy levels, the proton, by way of example, falls into one of two energy levels. The difference in energy levels, termed Zeeman splitting (after Pieter Zeeman, 1902 Nobel Laureate in Physics), provides for the possibility of radiative absorption or emission by the nuclei as they are passed from one energy level to another. By slight modulation of the applied field using the magnetic field gradient coils present in the scanner, it is possible to measure a different specific absorption and emission frequency and phase for many small volumes within the bore of the scanner. These small volumes are commonly termed voxels, to specify a three-dimensional unit of resolution similarly as the

term pixel specifies a two-dimensional unit of resolution.

While the precise physics of nuclear spin resonance are deserving of a treatise in and of themselves (Lambert and Mazzola, 2004), it is useful to have some specific understanding of the concepts central to MRI. When a suitable RF pulse is applied to the nuclei within the magnetic field, the populations at the susceptible energy levels are altered. Due to the slight predominance of nuclei in the lower energy state, as predicted by the Boltzmann distribution, a net absorption of radiation occurs. Depending on the length of the RF pulse, the precession frequencies of the nuclei are brought into phase and deflected all or partially into the magnetization plane transverse to the applied field. As time passes, various effects contribute to the eventual relaxation of this magnetic moment back to equilibrium. The two types of relaxation commonly measured by MRI are termed T1 and T2 relaxation. T1, or longitudinal, relaxation is governed by so-called spin-lattice interactions. That is, the inverted susceptible nuclei transfer their energy to the surrounding milieu, or lattice, thereby relaxing back into a lower energy state. Classically, this may be conceived of as the angles of the spin axis of the nuclei gradually realigning with the direction of the applied magnetic field. The energy of the nuclei is absorbed by the lattice often in the form of increased molecular rotational or vibrational energy, which, if sustained for an excessive period, can be observed as an increase in temperature. T2, or transverse, relaxation is governed by so-called spin-spin interactions. In spin-spin interactions, energy is transferred directly between two susceptible nuclei with similar precession frequencies. As the spins simply reverse orientation relative to the external magnetic field, no net change in T1 occurs. The drop in T2 is due to the loss of phase coherence when the transfer occurs.

In discussion of MRI pulse sequences, particularly the gradient echo which finds common use in fMRI, the term T2* is often encountered. In actual measurement, the signal decays much faster than would normally be predicted by T2 relaxation. The source of this additional speed is relaxation from the spins of the individual nuclei dephasing as they encounter local fluctuations in the magnetic field, and is designated as the T2* rate of relaxation.

I.1.1 Structural MRI

Structural MRI makes use of the small differences between voxels to differentiate neighboring types of tissue. For instance, the juxtaposition of a water-rich and water-poor tissue will lead to the eventual resolution of distinct voxel intensities as the T1 relaxation rates differ. In the particular example of a T1 image, it is illustrative to examine the different relaxation rates of nuclei in each of three environments commonly encountered in a scan of a neuroscience subject: bone, brain, and cerebral-spinal fluid (CSF.) In bone, the surrounding lattice is a solid with few protons to begin with, and those that are present have a long T1 relaxation time due to the scarcity of spin-lattice interactions in the rigid material. In brain, the mobility and molecular absorption frequencies of the tissue now provides for such relaxation events, leading to a shortening of the T1 relaxation time, and a presence of signal on the image. In CSF, the milieu is so mobile, suitable absorption frequencies are thinly distributed through a broad range causing the probability of an appropriate transfer event to fall, once again lengthening T1 relaxation time. Due to this relationship, CSF appears with the same low image intensity as bone. While imaging of the T1 susceptibility

of tissue is common in anatomical studies, it is not unusual to acquire a T2 image as well, due to certain types of pathology being more readily discernable in a T2 image.

Acquisition time in an anatomical study is usually only constrained by fatigue of the patient within the bore or clinical concerns. Essentially, only one measurement of each voxel volume needs to be made, although scans are often repeated for purposes of signal averaging. The resolution of such scans can therefore be very high to accommodate clinical discrimination of tissue features, with any drop in signal being overcome by lengthening the acquisition time of the scan. Contrast this method with the need for rapid whole volume acquisition in functional imaging, as discussed below.

I.1.2 Functional MRI

Differing from anatomical imaging, functional imaging requires speed and sensitivity of acquisition, usually at the expense of resolution. There is nothing fundamentally different about the signal which is acquired in a functional imaging scan, theoretically any type of anatomical imaging protocol could be used, however the main concern is now not anatomical discriminability, but change in tissue properties over time. T2 weighted images are almost universally used due to the reliance on imaging a changing local magnetic field due to various effects arising from functional activation. Although still a much debated topic, the foundation of functional MRI rests on the observation that activated neural tissue experiences a vascular change (Ogawa et al., 1990). The volume and flow of blood to an activated area of cortex can increase dynamically, with an accompanying change in oxygen consumption, over a period of several seconds following stimulation (Leniger-Follert and

Lubbers, 1976). Whether this activation truly represents an increase in neuronal activity is a current subject of investigation by means of combined electrophysiology and fMRI (Silva et al., 2000; Attwell and Iadecola, 2002; Logothetis, 2002, 2003; Logothetis and Wandell, 2004). Such comparative studies have shown a correlation between the increase of fMRI signal and spiking activity during a variable-coherence motion task (Rees et al., 2000) and the direct correlation of the fMRI response to the local field of simultaneously recorded neurons (Logothetis, 2002). Fundamentally, multiple low-resolution images of the area of interest are acquired in rapid succession, with a volume being completed typically on the order of two seconds. These images can then be compared in series to produce a time series of intensities for each voxel. The nature of the signal thus produced is dependent on the method of investigation, mainly differing in method of contrast used, as discussed below. This time series may then be used for experimental evaluation of response to an applied stimulus, in either a block design or event related paradigm. In a block design experiment, the subject performs two or more differing tasks, each individually and constantly for an extended period of time. The relative levels of activation during each task are then compared to gain insight into the differential activation of a cortical region. For an event related experiment, a single task is performed multiple times, and the ensuing responses are aligned upon the onset of the task and averaged in order to measure the time course of activation in a given cortical region. Hence, the strength of a block design paradigm is localization of functionally responsive areas, while the strength of an event-related experiment is insight into the nature of the ensuing response.

I.1.2.1 Blood Oxygen Level Dependent (BOLD) Contrast

It is the magnetic properties of hemoglobin itself which make a truly noninvasive functional imaging technique possible with MRI. Ever since the local blood oxygenation state was linked to signal intensity changes (Ogawa et al., 1990), the BOLD contrast method has been nothing short of a revolution in functional imaging. The technique depends on the fact that deoxyhemoglobin is weakly paramagnetic, and thus causes a local decrease in signal strength in vasculature and surrounding tissue. Specifically, as blood oxygenation decreases, its T2* shortens as well. However, when an area of cortex becomes active, cerebral blood flow and blood volume increase leading to an eventual lowering of the oxygen extraction fraction of the blood – that is, the blood supply increases beyond the demand, causing an eventual decrease in the level of deoxyhemoglobin. As the amount of deoxyhemoglobin diminishes, the paramagnetic effects are removed, and a rise in signal intensity is measured. In BOLD imaging, therefore, an activated area of cortex would demonstrate an elevation in signal intensity.

I.1.2.2 Exogenous Contrast

Much like the BOLD method described above, the use of an exogenous contrast agent in functional imaging depends on the eventual change in local concentration of a magnetically active substance. A wide variety of contrast agents are used clinically for diagnostic purposes, with gadolinium – a compound long known to affect magnetic relaxation rates(Bernheim et al., 1959) – perhaps being the most common (Gries and Miklautz, 1984; Villringer et al., 1988). Superparamagnetic iron oxide agents, such as Ferridex, also have

use in the imaging of organ tissue, but can be readily adapted as a functional contrast as well. Recently, the agent MION has been developed specifically for fMRI and demonstrates improvements over other iron oxide contrasts in terms of spatial and temporal resolution (Shen et al., 1993; Mandeville et al., 1998). In this case, when an areas of cortex becomes active, the local vasculature expands with an increase in cerebral blood volume, resulting in a given volume of brain having relatively more of the iron oxide agent. This local concentration of iron oxide produces a focal inhomogeneity in the magnetic field of the scanner. Nuclei affected by this inhomogeneity dephase quickly producing a drop in T2*. Much like the effects then of deoxygenated blood, a drop in signal intensity is observed. It is important to note that this is the opposite effect of the BOLD signal: with an iron oxide contrast agent, an increase in activation yields a decrease in signal intensity.

I.2 THE VISUAL MOTION AFTEREFFECT

The visual motion aftereffect (MAE) is a striking visual phenomenon experienced upon presentation of a static scene after prolonged viewing of a motion stimulus. An example of such an effect appearing in the early literature (Addams, 1834) is the viewing of a moving waterfall for several seconds followed by a gaze shift to the surrounding landscape. Although mentioned by such historical figures as Aristotle and Lucretius (Mather et al., 1998) it was not until the early 20th century that a comprehensive analysis of the psychophysics of the MAE was undertaken (Wohlgemuth, 1911). This treatment of the MAE established many of the fundamental parameters of the phenomenon, such as the direction, duration and additivity of the MAE to real motion. Furthermore, the storage of

the MAE is also considered. Storage occurs when the eyes are shut or the visual field is darkened immediately after viewing of the moving stimulus. Subsequent presentation of a static field will revive the MAE at a period when it normally would have faded.

I.2.1 Electrophysiology of the Motion Aftereffect

The earliest single unit study of the effect of prolonged viewing of a motion stimulus was performed in rabbit retina by Barlow and Hill (Barlow and Hill, 1963). The initial increase in firing rate of the retinal ganglion cells gradually decayed over a period of several seconds in an exponential manner. When the stimulus ceased moving, the spiking rate was suppressed below the initial baseline rate, leading to the suggestion that this suppression was the foundation of the MAE. This observation was further investigated in visual cortex in the cat (Maffei et al., 1973; Vautin and Berkley, 1977) with similar findings. The post-adaptation activity of motion-sensitive neurons in the owl monkey by Petersen and Allman demonstrated modulation of spike rate based on the orientation of the adapting stimulus (Petersen et al., 1985). If the subject was adapted to the preferred direction of movement for a given neuron, a subsequent presentation of motion in the preferred direction would elicit a lower spiking rate than normal. Conversely, if the subject was adapted in the anti-preferred direction, a subsequent presentation of movement in the preferred direction would elicit a higher spiking rate than normal. Spike rate suppression after adaptation was also demonstrated in the macaque and shown to cause a perceptual shift to favor the anti-adapted direction (Van Wezel and Britten, 2002). Ultimately the single unit studies, while still ongoing, seem to suggest that adaptation or fatiguing of direction sensitive neurons

contribute to the perception of illusory motion in the visual MAE.

I.2.2 fMRI Investigation of the Visual Motion Aftereffect

Similar to the electrophysiology, investigation of the time course of fMRI activation during a MAE task shows a correlation between perceived strength of motion and the MR signal strength (Tootell et al., 1995). Furthermore, this technique allowed the anatomical localization of an area in human cortex which responded similarly to the macaque motion-sensitive areas MT and MST (Tanaka et al., 1986). This early study did not have the spatial resolution to separate the two regions functionally, and the area was therefore termed the MT+ complex in human. More recent investigations involving hemifield stimuli similar to those used here were able to functionally dissect human MT+ into putative MT (pMT) and MST (pMST) regions posteriorly and anteriorly, respectively (Dukelow et al., 2001). A separate study has linked the effects of selective attention to an upregulation of the response during the MAE (Huk et al., 2001).

I.3 FUNCTIONAL IMAGING IN THE MACAQUE

While functional imaging in human subjects has become commonplace in the neurosciences, the use of non-human primates, such as the macaque, is a novel development. It is an aspect of functional imaging with many unique concerns and requirements. The maintenance of a colony of macaques in proximity to an available research magnet prevents this technique from being investigated currently at more than a few sites worldwide. Additionally, all the difficulties of maintaining the animal and many

of the concerns of electrophysiology in the macaque now must be dealt with in the cramped, isolated and potentially dangerous bore of an imaging system. However, this has not prevented investigation and development of methods for acquiring fMRI data in both the awake and anesthetized monkey.

I.3.1 Early Experiments

The earliest functional imaging experiments conducted in the macaque used positron emission tomography (Takechi et al., 1994), but it was not long before the use of fMRI was proposed (Westergaard et al., 1997) and ultimately accomplished (Dubowitz et al., 1998; Stefanacci et al., 1998). Initial results in visual cortex demonstrated that fMRI and the BOLD contrast method of imaging were viable tools for neurophysiologic investigation of the macaque. Early work was done entirely in clinical and research magnets all with a common horizontal bore. This confined the animal to be positioned in the "sphinx" position – prone with the head raised – a technique which is still used today. Development of vertical bore magnets at a handful of facilities now enables natural upright positioning of the animal.

I.3.2 Mapping Visual Cortex

The next step from observing the BOLD response evoked in visual cortex was comparing the results to human data (Dubowitz et al., 2001b) and mapping these effects in an ordered fashion such as retinotopy or motion selectivity. By presenting a stimulus in subregions of the visual field, the retinotopy of macaque visual cortex was determined and found to be

well conserved between monkey and human. In particular the early areas V1 and V2 are virtually identical, with variations of shape and cortical area beginning at the level of V3 (Vanduffel et al., 2001). Further along the visual pathway in V4, anatomical differences start to predominate, although the areas may be similarly functionally identified in human and macaque by color selectivity (Tootell et al., 2004). Current research has focused on more clearly defining the boundaries of these and other areas in the visual pathway (Brewer et al., 2002).

I.3.3 Current Studies

As the technique begins to proliferate, macaque cortex beyond the primary visual areas is currently being investigated. Anterior regions in the ventral stream of object and shape recognition are being described (Denys et al., 2004) and are demonstrated to show selective activation for the presentation of intact versus scrambled objects. Similarly, these areas have also been found to respond to images of faces (Tsao et al., 2003). Beyond passive viewing experiments, areas of cortex responsive to the execution and direction of saccades have been functionally imaged in frontal eye fields and posterior parietal cortex (Koyama et al., 2004).

I.4 SURGICAL PLANNING

Secondary only to primary diagnostic imaging, MRI finds clinical use as a surgical planning tool. Whether the procedure demands the targeting of a structure for repair or stimulation, or the demarcation of the extent of a region to be excised, as in the case of a

tumor, the high-resolution of MRI clearly provides a major aid. Indeed, beyond investigation in humans, anatomical imaging has been used for localization and differentiation in species useful in experimentation, such as the rhesus monkey (Price et al., 1997). Adapted to the neuroscience laboratory, medical uses may still be prevalent, but in the case of single and multiple cell electrophysiology a prime concern is the targeting of implanted electrodes or recording chambers (Asahi et al., 2003; Scherberger et al., 2003). Precise drug delivery, necessary in lesioning, also benefits from image-based targeting (Blaizot et al., 1999). While use of a magnet-compatible and visible stereotaxic device has been developed for surgical planning in the macaque (Saunders et al., 1990), such a technique requires specialized equipment that may not be readily available. Fortunately, anatomical landmarks commonly used in stereotaxic positioning, such as the internal auditory meati, can be visualized by imaging. The acquired image can be modified by computational methods (Cox, 1996a) to any alignment, in this case orthogonal to a stereotaxic setup. Using anatomical or functional landmarks to identify the structures of interest on the MRI image, the surgeon is then able to position chambers and/or electrodes by using the coordinate frame of the stereotaxic device inside the operating theatre (Dubowitz, 2002a). Such precise targeting helps to ensure that neurons of interest fall near subsequent electrode penetrations, sparing the time and effort of the experimenter and subject.

I.5 DETERMINING ELECTRODE PENETRATION SITES

In a neuroscience setting, particularly in single cell electrophysiology, it is vital to know the

precise location at which data was acquired. Classically, this was accomplished by histological preparation of the brain, which required euthanizing the animal, and microscopic evaluation of tissue. With the advent of high-resolution MRI, neuroimaging can supply this information for all but the most demanding localizations. While not a substitute for microscopic evaluations such as single cell cytoarchitecture investigation, MRI can resolve electrode locations on a millimeter scale (Hamel et al., 2002). MRI provides for adequate resolution for determining the position of a given site in the brain relative to surrounding cortical landmarks, such as sulci, gyri and subcortical nuclei. Furthermore, the use of metallic electrodes produces easily visualized tracks within neural tissue, likely due to microscopic sloughing of susceptible electrode material (Pezaris and Dubowitz, 1999a). Location of these sites, seen as dark artifacts on a MRI image, correlates well with penetration sites as reported by the experimenter. Additionally, if a recording chamber is used, its position may be visualized by a variety of methods and then overlaid on the image of cortex to provide a direct map of where a given penetration was performed. When generating such a map, it is beneficial to use an image of cortex up to a centimeter deeper than the actual recording site, particularly if the site was at the surface of cortex. This allows the clear visualization of surrounding structures, whereas a surface image would often show only a miniscule portion of cortex and be difficult to orient and interpret. Maximum utility is gained if the images are resliced such that the plane of each image lies perpendicular to the long axis of the recording electrode position, ensuring that perspective along the recording track is preserved.

CHAPTER II: Human Functional Imaging

This study served as my true introduction to the process of designing and implementing a fMRI experiment. Ultimately, the use of a human population as subjects for an experiment is easier in terms of task design, and is perhaps best suited to a non-invasive technique such as fMRI. Although, for purposes of length, examples of computer code produced to make these experiments possible are presented later in the appendices, such exercises were integral to the understanding of how fMRI data is acquired and processed.

II.1 ABSTRACT

The activation of motion-sensitive cortical areas in the human lateral occipital complex to a hemifield visual motion aftereffect (MAE) stimulus was investigated using blood oxygen level dependent functional magnetic resonance imaging. A central visual field stimulus spanning 16 degrees of visual arc consisting of radially expanding and contracting concentric circles was used. The region of interest was functionally differentiated into regions responding preferentially to contralateral stimulation and regions responding equally to ipsilateral and contralateral stimulation. Due to previous similarities observed between human and macaque visual motion processing, the areas are suggested to correspond to human pMT and pMST. Both areas responded to an adaptive and nonadaptive motion stimulus. The response of pMT to real motion differed significantly between ipsilateral and contralateral stimulation while pMST did not. The contribution of the visual MAE to functional activation was determined by subtracting the response

following the nonadaptive stimulus from that of the adapting stimulus. While both areas demonstrated a residual MAE response, the activation following ipsilateral versus contralateral stimulation in pMT was not statistically different. This suggests that while pMT may contain a MAE response, it is weak relative to the downstream area pMST.

II.2 INTRODUCTION

Visual motion is an integral and vital facet of sensory perception. While information may certainly be conveyed by a static scene, it is changing or moving scenes which are most prevalent in daily life. A simple, yet striking, illustration of the cortical processing of motion is the visual motion aftereffect (MAE), an early subject of psychophysics (Addams, 1834; Wohlgemuth, 1911). After viewing a scene with a constant direction of motion for several seconds, the opposite of that motion is perceived upon subsequent viewing of a static image. The percept of the aftereffect can be extended by the placement of an intervening dark, or storage, period between the two phases of the stimulus. Investigation of motion and its aftereffect has been pursued in many species, with fundamental studies of neuronal activity performed using single unit electrode recordings (Barlow and Hill, 1963; Maffei et al., 1973; Petersen et al., 1985). The MAE has also served as the subject of previous fMRI investigations (Tootell et al., 1995; He et al., 1998; Culham et al., 1999; Culham et al., 2000; Seiffert et al., 2003). A human homologue of macaque cortex area MT and MST, fundamental in motion processing, has been identified and is commonly referred to as V5, MT+, or the MT+ complex. Both areas respond to motion in the visual field with MT responding preferentially to simple motion, while MST has a role in more

complex processing such as object motion (Tanaka et al., 1993; Vanduffel et al., 2002) and the perception of heading and self-motion (Andersen et al., 2000). When functionally identified, this area typically is found on the lateral aspect of the occipital lobe, within or about the posterior reaches of the inferior temporal sulcus. Like macaque MT and MST, the area responds to stimuli such as first- or second-order motion, and shares anatomical similarities with the macaque region (Seiffert et al., 2003). Recently, further functional subdivision of this area has been possible using fMRI, such that putative homologues of the specific areas MT and MST, dubbed pMT and pMST in the human, can be identified based on their response to partial visual field stimuli (Dukelow et al., 2001). The areas differ in the important aspect that receptive fields of area MST are much larger than those of area MT, reaching 30 degrees or more across the vertical visual meridian into the contralateral visual field (Desimone and Ungerleider, 1986; Tanaka et al., 1986; Raiguel et al., 1997). Tootell et al. (1995) demonstrated that human visual areas from V2 to MT+ have an increasing activation during a MAE stimulus but did not differentiate between pMT and pMST. Towards that end, this study combines the investigation of the MAE with the use of a hemifield stimulus to attempt the analysis of the aftereffect in both subdivisions of the human MT+ complex. Storage of the MAE is known to occur when a blank field is presented between the moving and static stimuli (Thompson and Wright, 1994; Verstraten et al., 1994), and has been shown to prolong and postpone the functional activation during fMRI investigation (Culham et al., 1999). A storage period is used in this study to aid in the separation of activity resulting from real motion vs. perceived motion.

II.3 MATERIALS AND METHODS

II.3.1 Subjects

All subjects gave informed consent prior to participation and the study was performed under the approval of the Long Beach Memorial MRI facility. Six subjects (male, ages 25-44) are included in the study, imaging data was acquired from each subject for 8 to 10 repetitions of the paradigm.

II.3.2 Stimulus

A custom stimulus generation routine was coded in Visual C, using OpenGL routines for graphical rendering. The stimulus began with an 8 sec presentation of a central fixation point, which remained for all but the last ten seconds of the trial. Four 46 sec epochs followed, consisting of a 20 sec moving hemifield stimulus, a 6 sec "storage" period, and a 20 sec static stimulus (Figure II.1). In all cases the stimulus was based around the presentation of 7 concentric rings of equal width about the central fixation point spanning a visual arc of 16 degrees. Subjects viewed the screen through a mirror positioned at a 45% angle above the volume of the head coil. During a moving epoch, one visual hemifield (right or left) displayed contracting or expanding and contracting rings, while the opposing hemifield contained motionless rings. The speed of motion was fixed at 8 deg/sec and alternated every 2.5 sec in the case of expanding and contracting epochs. The static stimulus was a series of 7 motionless rings spanning both hemifields. This was back-projected onto white parchment within the bore of the scanner by an LCD projector operating at the foot of the magnet table at a resolution of 800x600. The ability of subjects

to accurately fixate on the central point was determined in an offline session using an infrared eye tracking device (Iscan Inc., Cambridge, MA.)

II.3.3 MR Imaging

All data was collected on a 1.5 T Magnetom Vision clinical MRI scanner (Siemens, Erlangen, Germany) with 25 mT/m (300 μs rise time) gradients. A conventional "birdcage" head coil was used for all measurements. Anatomical imaging was performed using a magnetization prepared rapid acquisition gradient echo sequence (TR 14 ms, TE 4 ms, 30 degree flip angle) with a 256 x 256 mm field of view on a 256 x 256 matrix yielding a native in plane resolution of 1 x 1 mm. 150 slices were acquired sagittally at 1 mm spacing to preserve voxel isotropy. Functional imaging was performed using a custom low-bandwidth (833 Hz/Px) echo-planar gradient echo sequence (TE 50 ms, TR 2 s effective, 90 degree flip angle) with a 256 x 256 mm field of view on a 64 x 64 matrix yielding an in plane resolution of 4 x 4 mm. 16 slices were acquired coronally at 4 mm spacing giving a final isotropic voxel resolution of 4 mm.

II.3.4 Image Analysis

All image processing was accomplished using the AFNI software package (Cox, 1996a) running on a Linux system. Functional data across trials was spatially aligned and averaged for each subject using AFNI routines. Active areas of cortex were determined using a voxel-wise cross-correlation against a boxcar waveform corresponding to motion epochs. Three such waveforms were used: all four motion epochs, right visual field only

epochs, and left visual field only epochs. The correlation map thus provided were thresholded at a $p < 0.05$ (corrected via the Bonferroni method for multiple measurements) and plotted as a cubic-interpolated overlay on the aligned anatomical images.

II.3.5 Time course Analysis

The time course of signal intensities in bilateral regions of interest along the posterior reaches of the infratemporal sulcus was recorded from voxels meeting the thresholding requirements described above. To begin to distinguish pMT from pMST, voxels with a significantly different ($p < 0.05$, 2-tailed paired t-test) average maximum intensity during the ipsilateral moving stimulus versus the contralateral moving stimulus were designated pMT/pMST while the remainder were designated pMST. Data was then averaged across subjects by area of interest calculating each hemisphere separately. To compute the residual signal corresponding to the motion aftereffect, the signal intensities for the expanding and contracting epochs were subtracted from the contracting only epochs. Peak intensity measurements were recorded from the acquisition yielding the highest BOLD signal response following motion stimulus presentation (in the case of real motion) or following the offset of subtracted motion periods (in the case of the motion aftereffect.)

II.4 RESULTS

II.4.1 Localization of Motion Sensitive Areas

Five human subjects were functionally imaged on a 1.5T clinical MRI system while performing a central fixation task with an adaptive and nonadaptive visual motion stimulus

(Figure II.1). The moving stimulus consisted of a series of concentric rings about the fixation point which contracted in the adaptive presentation or expanded and contracted in the nonadaptive presentation. To separate areas of cortex in each hemisphere responsive to motion in the ipsilateral and contralateral visual fields, only one hemifield of the stimulus was in motion at a given time. A similar whole field stimulus has been used previously to elicit response to motion from a variety of visual areas (Tootell et al., 1995). The stimulus used here had a common effect, and functional activation was demonstrated in visual cortex and the lateral occipital complex (LOC). By performing a cross correlation analysis of voxels responsive to a stimulus during all, ipsilateral only or contralateral only epochs of real motion, the extent and lateralization of active areas is visible (Figure II.2).

II.4.2 Separation of pMT and pMST

The active areas of the LOC along the posterior reaches of the infratemporal sulcus were designated as a region of interest previously shown to be a functional homologue of macaque areas MT and MST (Dukelow et al., 2001). A purely functional method of separating the voxel populations into putative MT (pMT) and putative MST (pMST) volumes was used to avoid inconsistencies that may be introduced into an anatomical separation, e.g., on a flattened cortex, by low-resolution functional acquisitions. Voxels with a significantly differing ($p<0.05$, two-tailed paired t-test) response to ipsilateral versus contralateral motion stimulation were designated as pMT volumes, while the remainder were designated pMST volumes. Of a total 270 functionally active voxels analyzed from all subjects 135 (52 left hemisphere, 83 right hemisphere) were found to have a pMST

response (Figure II.3) and 127 (78 left hemisphere, 49 right hemisphere) were found to have a pMT response (Figure II.4). Voxels with pMT effects also displayed activation during ipsilateral motion presentation likely due to pMT receptive fields slightly crossing the vertical visual meridian and contamination by pMST effects.

II.4.3 The Motion Aftereffect Response

Determination of the residual activation during the stationary or motion aftereffect stage of the stimulus was accomplished by subtracting the response of the nonadaptive stimulus from that of the adaptive stimulus (Figure II.5) as was described previously (Tootell et al., 1995). Peak response to real motion or the motion aftereffect was determined from the time point acquisitions having the greatest functional activation in the period following motion stimulation presentation or termination, respectively. A six second delay was allowed for lag of the hemodynamic response, but did not affect selection.

II.4.4 Differential Activation in pMT and pMST

For pMST volumes the response to moving stimuli was similar across visual hemifields and cortical hemispheres. In contrast, pMT voxels displayed a significantly greater response to contralateral versus ipsilateral stimulation for both adaptive and nonadaptive motion, while responses to the same type of real motion were similar across hemispheres. Voxel intensities during the motion aftereffect were similar across all conditions and achieved a peak response of ~40% of the response to real motion in the same visual field. Summary statistics for pMT and pMST are presented in Figures II.6 and II.7 and Table II.1.

II.5 DISCUSSION

II.5.1 Distinguishing Human pMT and pMST

Motion-sensitive areas in human LOC were determined using BOLD contrast fMRI. Subregions in the posterior infratemporal sulcus have been shown previously to correspond to macaque MT and MST (Tootell et al., 1995; Dukelow et al., 2001). Electrophysiology in the macaque shows that areas MT and MST contain receptive fields which span the midline of visual space, crossing the vertical meridian by 10-15% in the case of MT and 30-40% in the case of MST (Raiguel et al., 1997). In order to separate the areas entirely by eccentricity of receptive fields, a large central portion of the visual field could be left dark during stimulation (Dukelow et al., 2001). The presentation equipment used for this study allowed for only central visual field stimulation, so incomplete separation of the areas was anticipated. Despite this crosstalk, it was possible to separate the functional volumes into two distinct populations: those with and without a difference in level of activation for stimulus presentation in the ipsilateral and contralateral visual hemifields. While voxels having no significant difference suggest a representation of pMST, the remainder are a combination of pMT and pMST like volumes. However, for purposes of this study, the contribution of the pMT effects towards activation during real and illusory movement may be determined.

II.5.2 Contributions of pMT and pMST to the Motion Aftereffect

Both human areas pMT and pMST responded to presentation of real visual motion, in

keeping with numerous previous functional studies. Activation during subsequent static image viewing was found to peak at approximately 40% of the response to real motion, the attenuation possibly due to the delay in presentation from the storage period. The time course of the MAE response was similar to that published in a previous study of storage of the motion aftereffect (Culham et al., 1999). Human pMT, which demonstrated greater activation for stimulus presentation in the contralateral than the ipsilateral visual hemifield, did not show a significant difference in activation during the MAE period in the two hemifields although the trend was preserved. This effect was consistent across hemispheres. As a relatively smaller MAE response has been found in areas upstream in the visual pathway (Tootell et al., 1995) it is unlikely that pMT does not contribute to the activation entirely. This data suggests that the response of pMT to the motion aftereffect is on the order of the response of pMST.

II.6 CONCLUSION

Human MT+ was functionally subdivided into regions responding preferentially to contralateral visual motion stimuli (pMT/pMST) and regions responding equally to ipsilateral and contralateral visual motion stimuli (pMST). Both regions responded to real motion and the motion aftereffect. While pMT/pMST regions demonstrated a significant difference in response between ipsilateral and contralateral stimulation, the activation during the motion aftereffect period was the same. In agreement with previous work documenting MAE sensitivity in the human MT+ complex, this suggests that the contribution of human pMT to the MAE response is on the order of that of pMST. For the

first time the presence of a MAE signal has been shown in functionally identified human pMST.

II.7 ACKNOWLEDGEMENT

Thanks to Dar-Yeong Chen for technical assistance during scanning sessions and to the volunteer subjects for their time and effort. This work was funded in part by a James G Boswell Professorship, and a medical scientist training program grant from the National Institutes of Health and the UCLA Aesculapians.

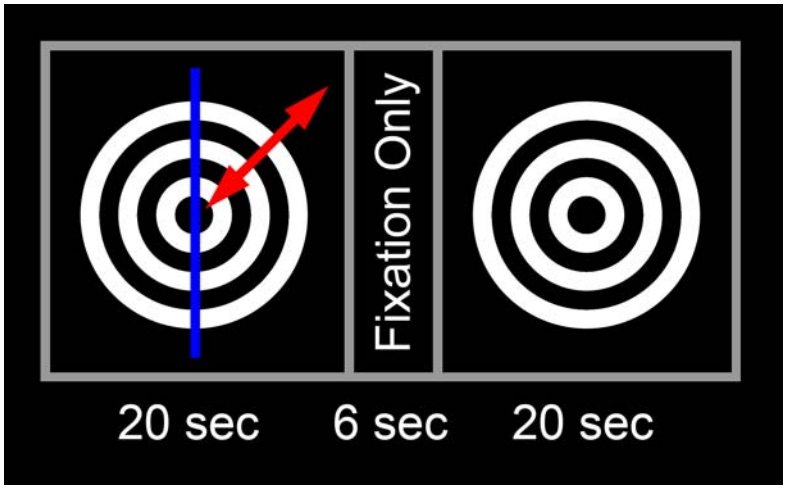

Figure II.1

Schematic of a stimulus epoch of motion, storage and static phases. A moving stimulus consisting of 7 concentric circles spanning 16 degrees of the visual field was presented centrally. The stimulus contained one moving and one stationary hemifield separated at the blue vertical meridian (shown here for diagrammatic purposes but not present in the actual stimulus). The moving hemifield either contracted or expanded and contracted, reversing direction every 2 seconds (right visual field expansion and contraction shown here.) A storage period was then presented containing only a central fixation point. Finally, 7 wholly stationary concentric rings were shown as a static stimulus.

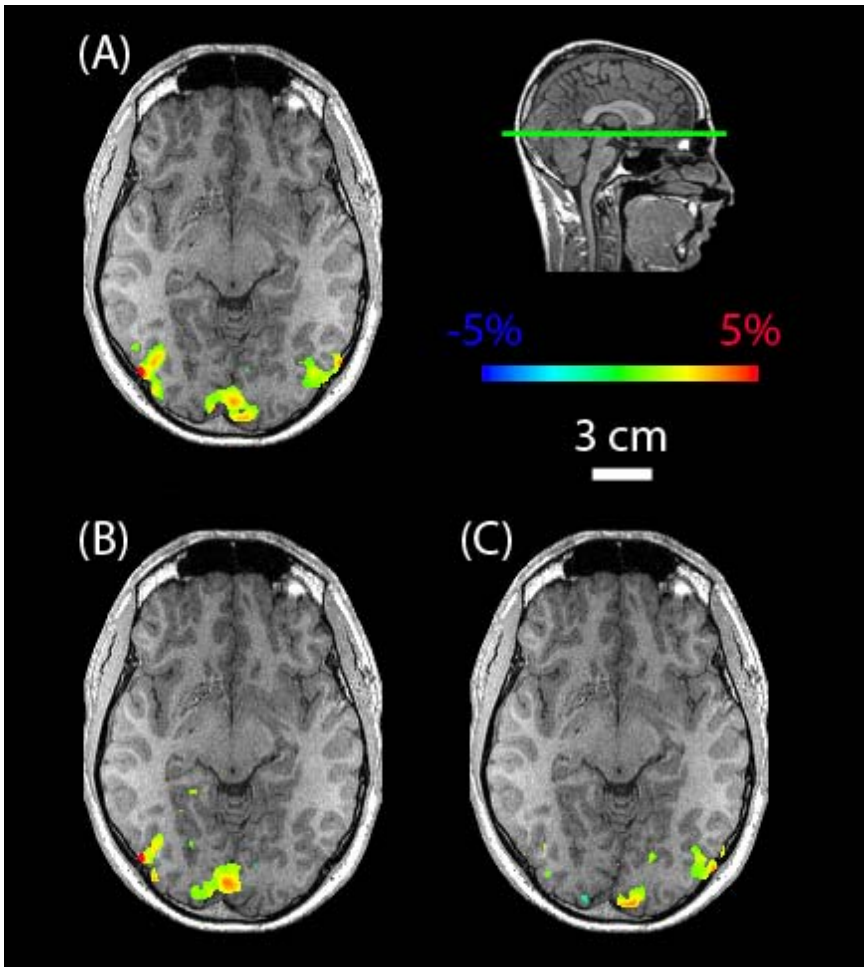

Figure II.2

Functional activation of correlated voxels ($p < 0.05$, Bonferroni corr. for multiple measurements) with bicubic interpolation overlaid on a spatially registered anatomical image. Planes are in radiological presentation with the subject's right on the left of the image. Voxels correlated with motion in both (A), left (B) and right (C) visual fields are shown. Note activation of primary visual cortex (medial) and posterior reaches of the infratemporal sulcus (lateral). Inset shows level of the scan on a mid-sagittal plane.

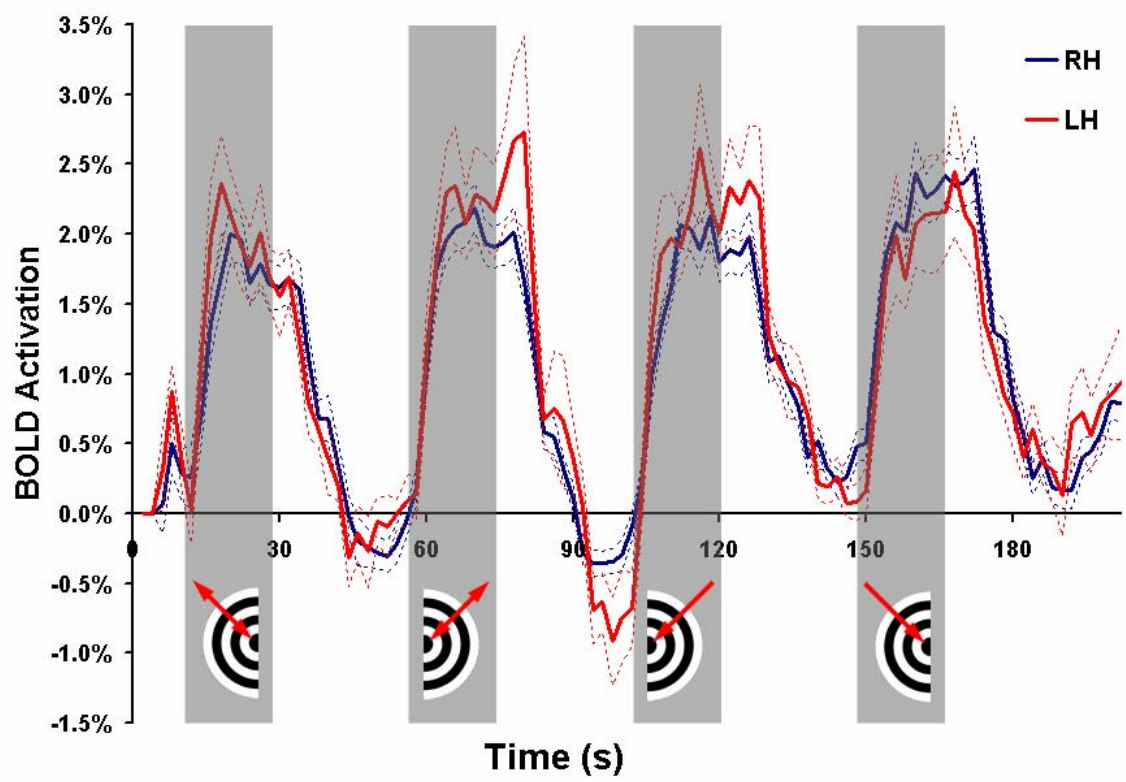

Figure II.3

Time course of BOLD activation in pMST voxels in right (blue) and left (red) hemispheres. All data from all subjects is included. Shaded gray areas represent periods of real motion. Stimulus location of the moving hemifield is represented diagrammatically below each epoch. Initial two acquisitions are omitted due to T1 weighting effects inherent in the EPI pulse sequence. Dashed lines indicate one standard error of the mean for each acquisition.

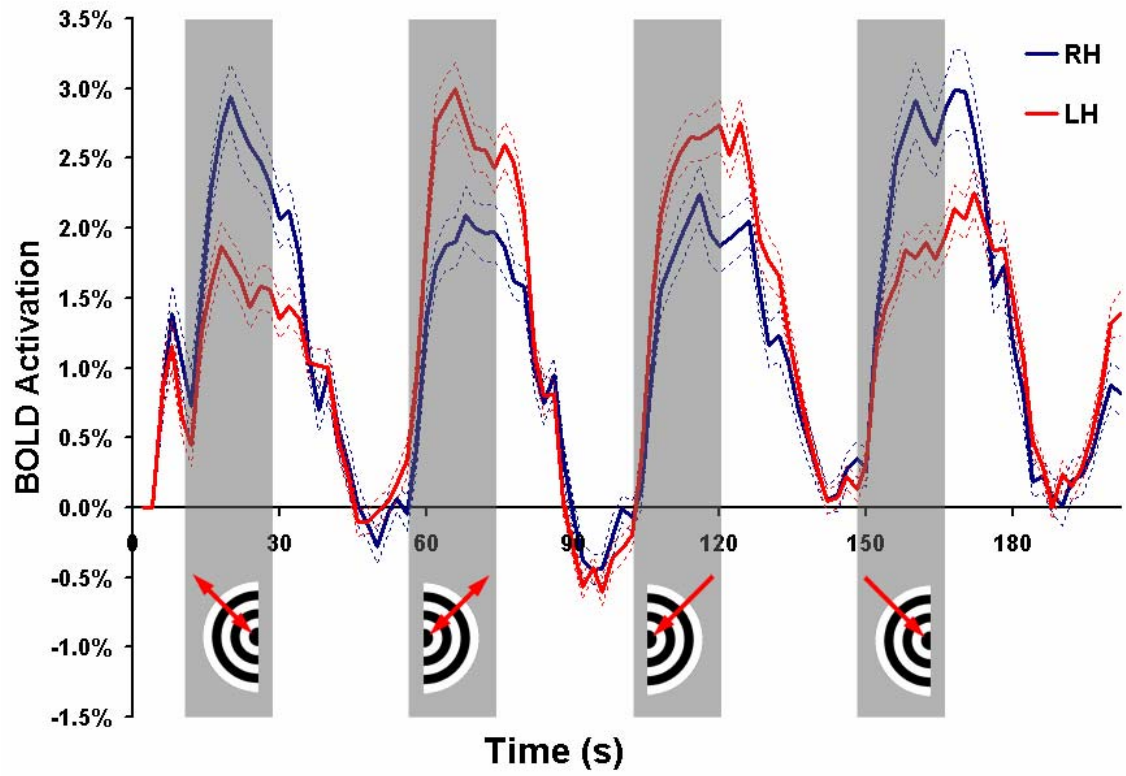

Figure II.4

Time course of BOLD activation in pMT voxels in right (blue) and left (red) hemispheres. All data from all subjects is included. Shaded gray areas represent periods of real motion. Stimulus location of the moving hemifield is represented diagrammatically below each epoch. Initial two acquisitions are omitted due to T1 weighting effects inherent in the EPI pulse sequence. Dashed lines indicate one standard error of the mean for each acquisition.

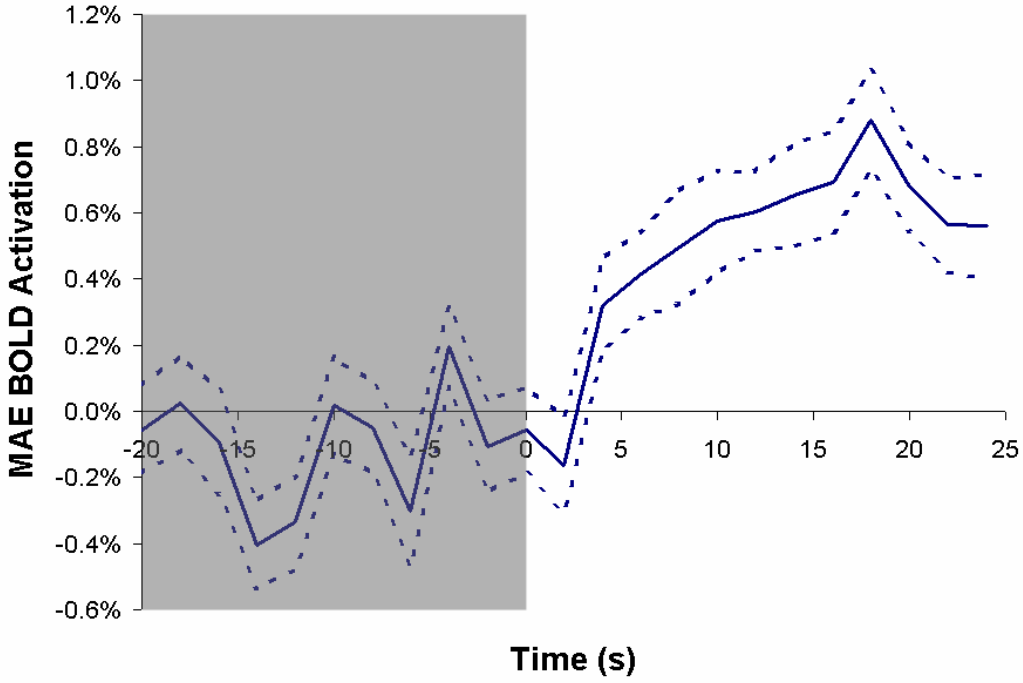

Figure II.5

Representative residual activation during the motion aftereffect period obtained from pMST voxels in the right hemisphere. Residuals are calculated as the activation during a contracting only stimulus epoch less the activation during an expanding and contracting epoch. All data from all subjects is included. Shaded gray area represents period of real motion. Dashed lines indicate one standard error of the mean for each acquisition.

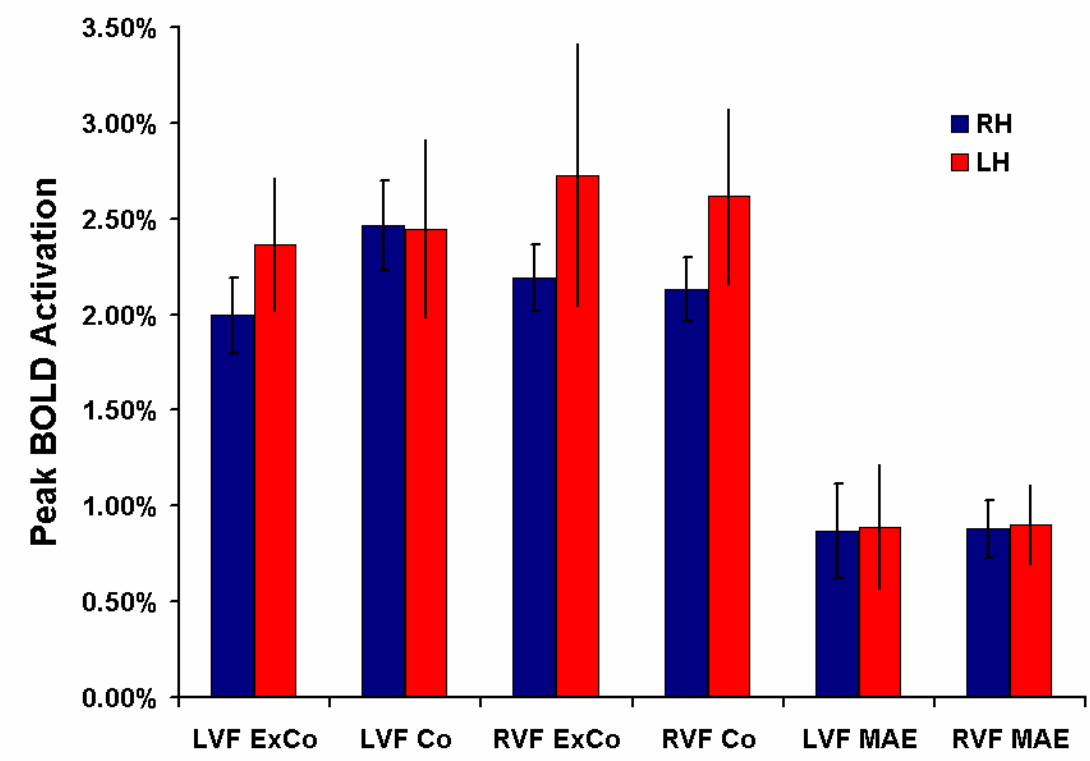

Figure II.6

Summary statistics for pMST voxels in left (red) and right (blue) hemispheres. All data from all subjects is included. Measurements were taken from the acquisition with maximum activation subsequent to motion presentation. Error bars represent one standard error of the mean for each stimulus type at the peak BOLD response.

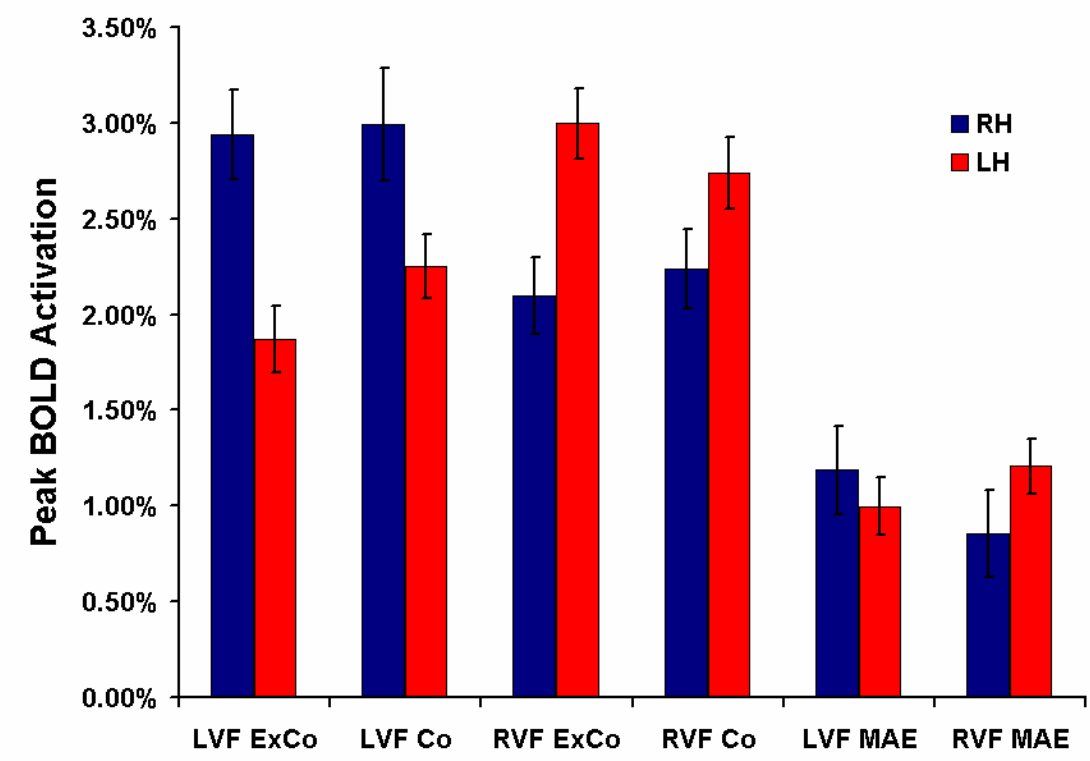

Figure II.7

Summary statistics for pMT voxels in left (red) and right (blue) hemispheres. All data from all subjects is included. Measurements were taken from the acquisition with maximum activation subsequent to motion presentation. Error bars represent one standard error of the mean for each stimulus type at the peak BOLD response.

Area	RH pMT					
Response Type	LVF Co	LVF ExCo	LVF MAE	RVF Co	RVF ExCo	RVF MAE
Peak Activation	2.99%	2.94%	1.19%	2.24%	2.10%	0.86%
SEM (+/-)	0.29%	0.23%	0.23%	0.21%	0.20%	0.23%
Area	RH pMST					
Response Type	LVF Co	LVF ExCo	LVF MAE	RVF Co	RVF ExCo	RVF MAE
Peak Activation	2.47%	2.00%	0.87%	2.13%	2.19%	0.88%
SEM (+/-)	0.23%	0.20%	0.25%	0.17%	0.17%	0.15%
Area	LH pMT					
Response Type	LVF Co	LVF ExCo	LVF MAE	RVF Co	RVF ExCo	RVF MAE
Peak Activation	2.25%	1.87%	1.00%	2.74%	3.00%	1.21%
SEM (+/-)	0.17%	0.17%	0.15%	0.19%	0.19%	0.14%
Area	LH pMST					
Response Type	LVF Co	LVF ExCo	LVF MAE	RVF Co	RVF ExCo	RVF MAE
Peak Activation	2.45%	2.37%	0.89%	2.62%	2.73%	0.90%
SEM (+/-)	0.46%	0.35%	0.32%	0.46%	0.69%	0.21%

Table II.1

Summary statistics for areas of interest in left (LH) and right (RH) hemispheres according to peak response to contracting only (Co) or expanding and contracting (ExCo) real motion and the motion aftereffect (MAE) in left (LVF) and right (RVF) visual fields.

CHAPTER III: Macaque Functional Imaging

This experiment was my first experience working with non-human primates. I owe much of my knowledge of macaque training and experimentation to David Dubowitz, who was quick to enable me to work with the animal on my own. This work was originally published under the title of "Enhancing fMRI Contrast in Awake Behaving Primates Using Intravascular Magnetite Dextran Nanoparticles" (Dubowitz et al., 2001a). All fMRI data was acquired jointly, I was responsible for the analysis of the fMRI data, while David Dubowitz acquired and analyzed the spectrometer data. Dar-Yeong Chen provided technical assistance at the scanning facility, which was graciously lent to us by William Bradley.

III.1 ABSTRACT

Functional MRI in awake behaving primates is an emerging tool for bridging the gap between human functional MRI (fMRI) and neurophysiology information from non-human primates. We report the use of magnetite dextran nanoparticles (Feridex) as a blood-pool agent to enhance fMRI contrast-to-noise (CNR) in primate fMRI. Intravascular half-life of the magnetite dextran was long compared to lanthanide chelates ($T_{½}$=198 minutes) with shortened T_2 relaxation observed in blood and cerebral cortex. Greater than 3-fold enhancement in the percentage MR signal change was observed using nanoparticles (13%) compared with conventional BOLD fMRI (3.8%). The calculated regional cerebral blood volume in macaque primary visual cortex increased 32% with photic stimulation. The

increased CNR allows greater flexibility in the design of awake behaving primate fMRI studies with the potential for improvements in resolution and significantly shortened imaging times.

III.2 INTRODUCTION

fMRI is a rapidly emerging tool in the study of primate physiology. Previous studies have addressed the potential value of fMRI in awake macaque monkeys for investigating visual neuroscience (Dubowitz et al., 1998; Stefanacci et al., 1998; Logothetis et al., 1999a; Paradiso, 1999; Dubowitz et al., 2001b) and basal ganglia function (Zhang et al., 2000). One major limitation in performing monkey fMRI at 1.5T is the limited signal-to-noise and consequently low contrast-to-noise ratio (CNR) from Blood Oxygen Level-Dependent (BOLD) Contrast. As with all imaging techniques, there is a compromise between resolution and sensible imaging time. Monkeys are challenging subjects to study. They need to be meticulously trained to remain still for awake MRI studies (thus shorter imaging sessions facilitate behavioral compliance). However, the brain of a macaque monkey is approximately 1/5th of the size of a human brain (Allman, 1999), so there is also a need for higher resolution compared with human fMRI studies. One approach to this has been to do macaque imaging at higher applied magnetic field (Logothetis et al., 1999a). While improving the CNR, this also increases the unfavorable susceptibility gradients and artifacts which scale proportionately with the applied magnetic field. Another approach has been to restrict imaging to anesthetized animals. This allows longer imaging times and reduces movement artifacts, but may also diminish BOLD effect due to the vasodilator

effects by anesthetic agents, and consequent changes on cerebral blood flow (CBF) (Seifritz et al., 2000). The use of anesthesia also excludes cognitive studies for which awake behaving subjects are required.

We investigated the effect of a blood-pool T_2 contrast agent on CNR compared with conventional BOLD contrast in awake behaving primate fMRI experiments. Previous studies have demonstrated the utility of such agents for MRI in rats (Mandeville et al., 1998), cats (White et al., 1992) and human subjects (Scheffler et al., 1999).

The use of contrast agents has not found much favor in human cognitive studies because this makes the study more invasive, but holds promise for awake animal studies. This is the first time this technique has been applied to awake primate imaging. Techniques that employ a T_2 contrast agent provide images sensitive to changes in regional cerebral blood volume (CBV). This has been shown in rats to change by 20% with neural activation (Kennan et al., 1998; Mandeville et al., 1998) and by 25% (Scheffler et al., 1999) to 32% (Belliveau et al., 1991) in humans. Unlike deoxyhemoglobin susceptibility, the CBV change is not dependent on applied magnetic field (Mandeville et al., 1998), and thus this technique provides great scope for improved fMRI contrast even at conventional magnetic fields (1.5 T).

III.3 MATERIALS AND METHODS

III.3.1 Animal Subjects

Approval for this research was obtained from the Institutional Animal Care and Use Committee, Epidemiology and Biosafety Committees. All imaging was done on a 1.5 T Siemens Vision MR scanner with 23 mT/m gradients (300 μs rise time). Awake behaving studies were done on a 8.5 kg male rhesus macaque monkey (*macaca mulatta*) lying in a "sphinx" position within the scanner using a 19 cm circularly polarized knee coil. Contrast excretion measurements were done outside the MR scanner on the same animal. Relaxometry studies were also performed on this monkey and on two additional male macaque monkeys (5.5 kg and 10.5 kg) under isoflurane anesthesia. The technique has been previously described (Dubowitz et al., 1998; Dubowitz et al., 2001b), but in brief: The animal was transported to the MRI facility in a custom designed cage. For awake studies he crawled into a short tube so that his legs were accessible for intravenous administration of T_2 contrast agent. The monkey was trained to present his leg to the animal handler and accept an intravenous line into a saphenous veins without sedation or general anesthesia. The monkey then crawled into a larger tube which was transferred to the MRI scanner. His head was secured to the transmit/receive coil and a screen placed 57.3cm in front of him (providing a ±22º visual field of view). Eye-position tracking was performed using a custom built shielded video camera placed at the bore of the scanner which was sensitive in the infrared range, and eye illumination from a circular array of 28 MRI compatible IR light emitting diodes emitting at 810nm (Dubowitz et al., 1999). Digital signal processing involved a system from ISCAN (Iscan Inc. Cambridge, MA) integrated into a computer running a custom program written with Labview software (National Instruments Corporation, Austin, TX). This setup allowed eye tracking in complete darkness to an

accuracy of within 1º of arc. The animal was trained to remain motionless in the scanner for the duration of the imaging experiment (i.e., while gradient noise was audible) and to fixate on a central fixation point to an accuracy of <4º visual angle for the duration of the stimulus. He was provided a fruit juice reward at the end of each imaging run. For anesthetized studies, the animal was sedated with 10mg/kg ketamine and maintained on 2% isoflurane using an anesthetic setup modified for MRI compatibility.

III.3.2 Contrast Agent

For functional imaging studies with T_2 contrast agent we used magnetite dextran nanoparticles (Feridex, Advanced Magnetics Inc, Cambridge, MA) infused intravenously. This was given as 4.2 mgFe/kg (750 μMol/kg) diluted into 25ml and infused over 5 minutes through a 5μm filter. Imaging was started within 10 minutes of completing the infusion (ensuring equilibrium state concentration). For assessment of whole blood clearance, a dose of 2.8 mgFe/kg (500 μMol/kg) was used.

III.3.3 MR Imaging

BOLD and magnetite-enhanced functional images were acquired using a gradient-echo echo planar imaging (GE-EPI) mosaic sequence. The effective echo time (TE_{eff}) of 50ms was chosen to approximate the T_2* of monkey cortex (Dubowitz et al., 2001b). Isotropic 4mm resolution was achieved with a FOV of 256 x 256mm and a 64 x 64 matrix. Fourteen, 4mm thick axial slices of the entire monkey's brain were acquired per repetition of 2000ms (effective TR = 2000ms). Forty-five repetitions of the 14 slices were acquired for BOLD

experiments and 60 repetitions for magnetite dextran experiments. The first repetition was not used in data analysis allowing 2 seconds to ensure steady state. Anatomical images used a 3D Magnetization Prepared Rapid Acquisition Gradient Echo sequence (3D-MPRAGE) with TR/TE = 11.4 / 4.4 ms, flip angle 12 degrees, inversion time (preparation time) 250 ms and delay time (magnetization recovery time) 600ms. A 141 x 141mm field of view (FOV) was acquired with a 128 x 128 matrix (zero-padded to 256 x 256), and 118 phase encode steps made through a 130mm slab (1.1mm isotropic resolution). Relaxometry measurements for T_2* (R_2*) in cortex used a 2D Fast Low Angle Shot (FLASH) sequence (TR 1000 ms, TE 5, 7, 10, 12, 15, 18, 20ms) as previously described (Dubowitz et al., 2001b). Relaxometry measurements on in-vitro venous blood were performed using a CPMG spectroscopy sequence on a Bruker minispec mq60 at 60Mhz (Bruker Analytik GmbH, Rheinsteffen, Germany).

III.3.4 Stimulus Paradigm

The stimulus consisted of a six second black and white polar checker-board alternating at 8Hz, which subtended a visual angle of ±20º. The stimulus was preceded by a 1º fixation point visible for 8 seconds. Following the fixation dot and checker board stimulus the animal remained in the dark for a further 76-106 seconds to allow acquisition of the full recovery of the hemodynamic response.

III.3.5 Image Post-processing

Functional imaging data using BOLD and magnetite dextran contrast were analyzed off-

line using AFNI software running on a UNIX workstation (Cox and Hyde, 1997). Functional images were co-registered using a volume-registration algorithm under AFNI. A weighted linear least squares fit of the images was employed with Fourier interpolation used for resampling (Cox and Jesmanowicz, 1999). Images with excessive motion artifact not corrected by the registration algorithm were excluded. The remaining runs were averaged together to create a single dataset for BOLD imaging and a single dataset for magnetite-enhanced imaging. A representative region of interest was chosen in primary visual area V1 (Figure III.1). The time course of the percent change in MRI signal in this volume was plotted for BOLD and magnetite-enhanced fMRI (Figure III.2).

For cerebral relaxometry measurements following magnetite dextran infusion, regions of interest were drawn around anatomically defined gray matter using Scion Image software (http://www.scioncorp.com). R_2* transverse relaxation rate was calculated by assuming an exponential relationship between the MR signal, S(TE), the echo time, TE, and the initial signal S(0) described by Equation 1:

$$S(TE) = S(0)e^{-TE \cdot R_2^*} \qquad [1]$$

The fit optimization was implemented in Matlab (The Mathworks Inc., Natick, MA) using a proprietary large-scale subspace trust-region algorithm based on an interior-reflective Newton method (Coleman and Li, 1996). The algorithm allows specification of upper and lower bounds on each optimized parameter.

Relaxivity data on whole blood to assess clearance of contrast media was assumed to follow first order kinetics and was modeled with monoexponential decline described by Equation 2.

$$[Fe]_{Blood} = C_0 \cdot e^{-bt} \quad [2]$$

$[Fe]_{Blood}$ is the concentration of Fe in blood, C_0 is the instantaneous concentration at time zero. Dividing the injected dose by the instantaneous concentration of contrast media, C_0, yields the volume of distribution of the agent within the animal. The constant, b, is an excretion constant from which the half life of elimination from blood can be calculated.

There is a linear relationship between the transverse relaxation rate of the magnetite dextran contrast media in blood and the concentration of Fe. The main components of the measured R_2* are components from blood itself, R_2*_{Blood}, and from exogenous magnetite, R_2*_{Fe}. (Equation 3):

$$R_2*_{Blood} + R_2*_{Fe} = k \cdot [Fe]_{Blood} \quad [3]$$

The unknown contribution to transverse relaxation rate from Fe, $R_2*_{Fe,}$ used in Equation 3 was calculated by making serial dilutions of a known concentration of Feridex with water as described in Equation 4 (Figure III.3a).

$$R_2{}^*_{water} + R_2{}^*_{Fe} = k \cdot [Fe]_{water} \quad [4]$$

Using Equations 4 and 5, the actual concentration of Fe was quantified from measurements of R_2* for whole blood drawn at regular intervals following injection of the contrast agent (Figure III.3b).

To compare the magnitude, duration and onset delay of the positive MR signal change for BOLD with the negative signal change for magnetite-enhanced fMRI, the data was fitted to a gamma-variate function of the form in Equation 5 using the same Matlab routine described above.

$$S(t) = A(t - t_0)^r e^{-(t-t_0)/a} \quad [5]$$

A, r, and a are fit constants and t_0 defines the onset delay following the neuronal stimulus. The maximum signal change was the peak of the curve. The duration of activity was compared during the period when the MR signal exceeded 10% of its maximal value.

We calculated the percentage change in the regional cerebral blood volume following photic stimulation. This model assumes that the effect of the decreased transverse relaxation rate due to BOLD is negligible compared to the increase due to CBV changes with the intravascular contrast agent. Previous studies have shown the rate of change in

transverse relaxation rate with blood iron concentration is proportional to the cerebral blood volume (i.e., the cerebral blood volume CBV(t) can be calculated from the slope of a plot of R_2* change with $[Fe]_{blood}$ (Scheffler et al., 1999)).

$$\frac{R_2*(t) - R_2*(0)}{[Fe]_{blood}(t) - [Fe]_{blood}(0)} = K \cdot CBV(t) \qquad [6]$$

Where R_2*(t) is the transverse relaxation rate during activation or rest, R_2*(0) is the relaxation rate prior to injection of magnetite dextran, $[Fe]_{blood}(t)$ is the blood concentration of Fe during the photic stimulation experiment, $[Fe]_{blood}(0)$ is the blood concentration of Fe due to magnetite dextran prior to injection (i.e., zero) and K is a proportionality constant.

The fractional change in blood volume following photic stimulation, ΔCBV, can thus be calculated from the CBV during rest, CBV(r), and during activation, CBV(a), from Equation 8.

$$\Delta CBV = \frac{CBV(a) - CBV(r)}{CBV(r)} = \frac{R_2*(a) - R_2*(r)}{R_2*(r) - R_2*(pre)} \qquad [7]$$

From Equation 1, this can be written in terms of the ratio of MR signal during photic stimulation and at rest.

$$\%CBV = \frac{\frac{-1}{TE}.\ln\left(\frac{S(a)}{S(r)}\right)}{R_2*(r) - R_2*(pre)} * 100\% \qquad [8]$$

R_2* in brain was measured before injection of magnetite dextran, R_2*(pre), and at regular time points during the experiment, R_2*(t). This value of R_2*(t) was interpolated to the actual time point of the photic stimulation measurement, R_2*(r), to allow for changes in R_2* due to hepatic elimination of Fe (see Equation 2). The MR signal change, S(t), following photic stimulation was fitted to the gamma-variate function described by Equation 5 (Figure III.2). S(r) was the value of the function at t <5 seconds and S(a) was the maximum value of the function (t= 48 seconds).

III.4 RESULTS

Nine runs of BOLD contrast and 5 runs of magnetite-enhanced contrast, which were free from any motion artifact, were acquired in an awake behaving monkey with eye traces confirming he was fixating for the duration of the experiment. The distribution of fMRI activation for the checker-board stimulus is seen in visual cortex in the correlation map in Figure III.1. The hemodynamic response curves for conventional BOLD fMRI and magnetite-enhanced fMRI are shown in Figure III.2. The positive BOLD effect and negative magnetite-induced MR signal changes were fitted to independent gamma-variate functions. Following photic stimulation, the MR signal in macaque visual cortex is modulated by up to 3.8% for BOLD imaging and follows a characteristic time course – similar to that routinely described in human fMRI at 1.5T. Increase in BOLD MR signal occurred in primary visual cortex almost immediately following stimulus onset. The peak BOLD signal change was observed 10 seconds following the stimulus onset. The response showed a typical rise followed by an undershoot, returning to baseline by 50 seconds. The

duration of the positive BOLD change (measured between the rise above 10% maximum signal change to the fall below 10% maximum) was 24 seconds (4-28 seconds after stimulus onset). Using intravenous magnetite dextran, there is a 13% negative MR signal change in the same area of primary visual cortex following photic stimulation. Maximum effect was seen at 48 seconds. The modulation in MR signal persisted for 88 seconds (20 – 108 seconds between the 10%-of-maximum points). The intravenous magnetite dextran increased the R_2* (and R_2) relaxation rates in resting gray matter. The change in transverse relaxation rate of blood over time was measured in the same animal used for the fMRI study, and is presented in Figure III.3b. This shows an elimination $T_{½}$ from blood of 198 minutes. The volume of distribution (instantaneous blood concentration divided by dose injected) was 825ml. The percentage change in regional cerebral blood volume in macaque primary visual cortex following photic stimulation was 32%.

III.5 DISCUSSION

Feridex (ferumoxide solution) is an aqueous colloid of magnetite iron oxide nanoparticles (60-150 nm diameter) associated with dextran having an average chemical composition of $FeO_{1.44}$. Excretion of Feridex is 98% hepatic (its primary use in diagnostic imaging is as a T_2 liver contrast agent). In this study we have used it as a blood-pool contrast agent, taking advantage of its slow excretion kinetics and prolonged blood half-life. The blood volume of a 8.5kg macaque monkey is approximately 10% of body weight (Butler et al., 1995), thus the calculated volume of distribution (825ml) confirms that Feridex is a true blood-pool agent.

Functional MRI provides an indirect map of neuronal activation by demonstrating changes in cerebral blood dynamics that accompany neural activity. These temporally correlated changes may be seen as changes in blood flow (Kwong et al., 1992), blood volume (Belliveau et al., 1991) or changes in the deoxygenation of hemoglobin (Turner et al., 1993). Imaging the changes in blood volume is well established – the first fMRI descriptions of neuronal activity in humans mapped changes in CBV (Belliveau et al., 1991). For human studies, it has become more popular to use fMRI studies with endogenous contrast based on changes in the oxygenation of hemoglobin thus making the study entirely non-invasive. The use of iron oxide T_2 contrast agents with a long intravascular half-life has been shown to be a valid method to track CBV changes during neuronal stimulation in rats (Mandeville et al., 1998) and human subjects (Scheffler et al., 1999). The increase in transverse relaxation rate ($\Delta R_2^* = 1/\Delta T_2^*$) due to increased blood volume competes with the decrease in relaxation rate due to changes in deoxyhemoglobin accompanying neuronal activation. It is necessary to use a sufficient intravascular concentration of contrast agent to ensure that the signal changes induced by the contrast agent and increased CBV dominate concurrent BOLD changes. At 1.5T these relaxivity changes due to hemoglobin susceptibility effects are relatively small, however the observed MR signal changes due to the T_2 agent are less than the theoretical maximum, as these competing effects reduce the magnitude of the MR signal change (Mandeville et al., 1998).

The calculated CBV change with stimulation was 32%. This is in good agreement with

previous measurements of between 25% (Scheffler et al., 1999) and 32% (Belliveau et al., 1991) in human subjects. This concordance in CBV changes between human and macaque highlights a similarity in their neurovascular physiology which underscores the value of macaque fMRI as a model for better understanding human neurophysiology.

It is important to consider the decay in R_2* over time due to hepatic elimination of contrast medium as well as the R_2* modulation due to changes in blood volume. The elimination half-life of Feridex (198 mins) is of the same order of magnitude as the duration of many primate physiology studies. Closer inspection of the intravascular iron concentration during a typical 3.5 hour primate imaging session using a dose of 4.2 mgFe/kg (750 μMol/kg) shows it ranged from 36.75 μgFe/ml (659 μMol) instantaneously following injection to 19.5 μgFe/ml (350 μMol). Comparison with previous studies using the same T_2 contrast agent in humans indicates that the BOLD effect due to auditory stimulation is completely negated by the iron-oxide enhanced CBV effect at a concentration of 8.4 μgFe/ml (150 μMol). Extrapolating our elimination curve (Figure III.3) to this point where the BOLD effect completely opposes signal due to exogenous magnetite, indicates that signal would be lost 7 hours after injection. During a typical primate study, the opposing effects on transverse relaxation from BOLD may be assumed to be negligible. Under ideal conditions, the signal change with neuronal stimulation could reflect the whole 32% increase in CBV, thus CNR improvements of 8-fold could theoretically be achieved over our 3.8% BOLD MR signal change. There is thus scope to improve the MR signal response above the threefold enhancement demonstrated here. The use of higher doses is under review. Our TE

of 50 ms was initially set for maximum tissue contrast during BOLD studies, and was held constant during the study. Reducing the TE to the T_2* of grey matter following magnetite dextran infusion would further improve SNR and the CNR observed during magnetite-enhanced fMRI. Additionally, using other iron oxide agents with smaller particle size than Feridex (and a longer elimination half-life and higher T_2 relaxivity characteristics (Mandeville et al., 1997)) would further improve the signal benefit over conventional BOLD imaging.

In non-human primates, the temporal dynamics of the CBV changes are slower than the BOLD effect (similar to that described in rats (Mandeville et al., 1998)). This may place some constraints on paradigm design. For block design paradigms, the time-course of each state may need to be longer than the minimum times typically possible for BOLD studies; however, superposition calculations may be used to reduce this increase in experimental time. The use of event-related techniques (currently used in BOLD fMRI to observe temporal changes which are fast relative to the prolonged hemodynamic response (Dale, 1999)) can potentially be applied to CBV imaging as well. For most primate studies, the 3-fold increase in CNR (with theoretically further increase possible) outweighs many limitations that the slower return to baseline may place on the choice of paradigm. To achieve a comparable 3-fold increase in CNR using BOLD fMRI at 1.5T would require a 9-fold increase in experiment time or 3-fold increase in voxel size.

The added CNR by using magnetite-enhanced fMRI can be used to improve resolution or

shorten total experimentation time. Motion artifact is the major difficulty in imaging awake behaving primates, and the ability to reduce the number of runs (and the overall length of an experiment) will have dramatic and positive benefits on experimental success. Non-human primate functional neuroanatomy has been used as a model for better understanding the human brain. The smaller brain size may equate to smaller functional units within the cortex for which higher resolution is required (although the exact scaling factor of functional units across species remains to be determined (Ahrens and Dubowitz, 2001)). The ability to achieve higher resolution in primate fMRI also adds to its utility when comparing with neurophysiology data.

The BOLD effect scales between linearly and quadratically with applied field strength (Gati et al., 1997). Thus high field imaging at 4.7 Tesla (Logothetis et al., 1999a) could be expected to afford at least a threefold increase in CNR. This theoretical gain needs to be offset by increased bulk-susceptibility artifacts at higher applied magnetic fields. Using magnetite-enhanced fMRI for primate imaging at 1.5T allows a comparable increase in CNR (with further CNR improvement anticipated with the use of alternate contrast agents), but without the increase in bulk susceptibility distortions induced by higher field. Similar improvements in resolution seen by increasing the applied field strength to 4.7T are thus achievable using magnetite-enhanced fMRI at 1.5T.

III.6 CONCLUSION

We describe a modification of conventional BOLD fMRI applied to awake behaving

primates. Intravenous infusion of magnetite dextran nanoparticle T_2 contrast agent produces an 3-fold increase in CNR. Opportunities for further optimization are also discussed. Considerably faster overall experiments involving fewer sampling repetitions may now be performed, with the potential for higher resolution imaging compared with existing fMRI techniques at 1.5T. Regional cerebral blood volume increases by 32% in macaque visual cortex, which is comparable to the neuronally-induced vascular changes previously described in humans.

III.7 ACKNOWLEDGEMENT

We gratefully acknowledge J Michael Tyszka for enlightened discussion and Betty Gillikin for help with animal handling and health care. This work was funded in part by a James G Boswell Professorship (RAA), a medical sciences training program grant (KAB) and a grant from National Institutes of Health (EY07492).

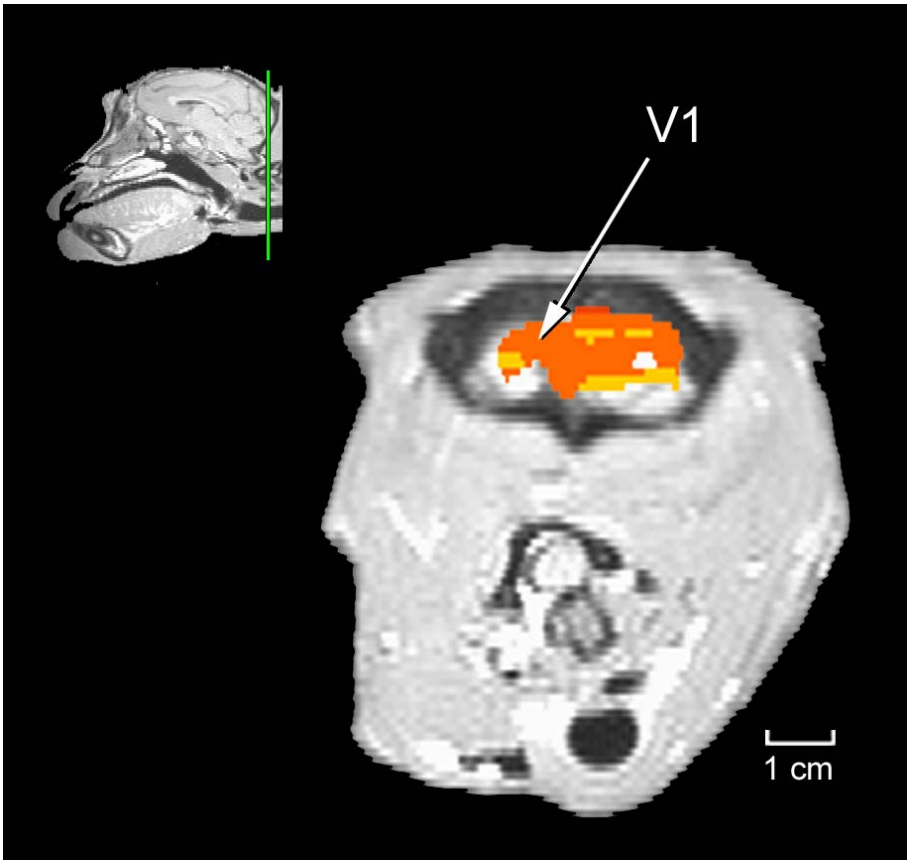

Figure III.1

Coronal image showing functional activation in primary visual cortex (V1) during photic stimulation in a macaque monkey following intravenous T_2 magnetite dextran contrast agent. The plane of section is indicated by the vertical bar on the sagittal image. The area of V1 used to plot MR signal responses is indicated. (Subjects right is on the left of the image.)

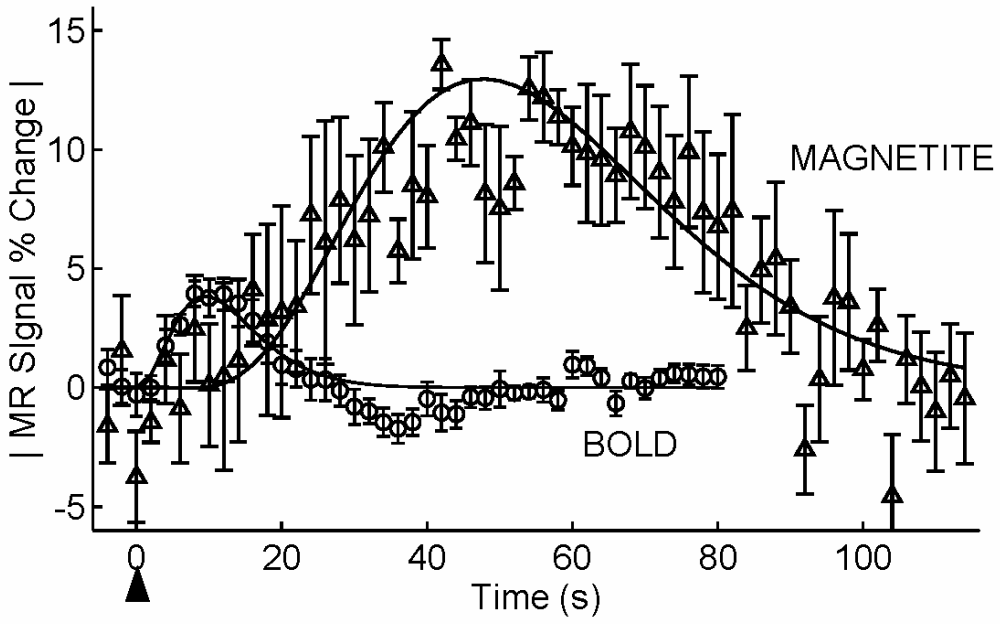

Figure III.2

The time course of the percentage change in MR signal following 6 seconds photic stimulation is shown for BOLD (o) and magnetite-enhanced (Δ) fMRI. Stimulus onset is indicated by the arrow. Negative MR signal changes for magnetite-enhanced fMRI are shown as positive absolute changes for comparison. Error bars indicate ± 1 standard error for BOLD (n=9) and magnetite dextran (n=5) studies. Solid line is the gamma-variate function fitted to the data for the positive BOLD and negative magnetite dextran responses.

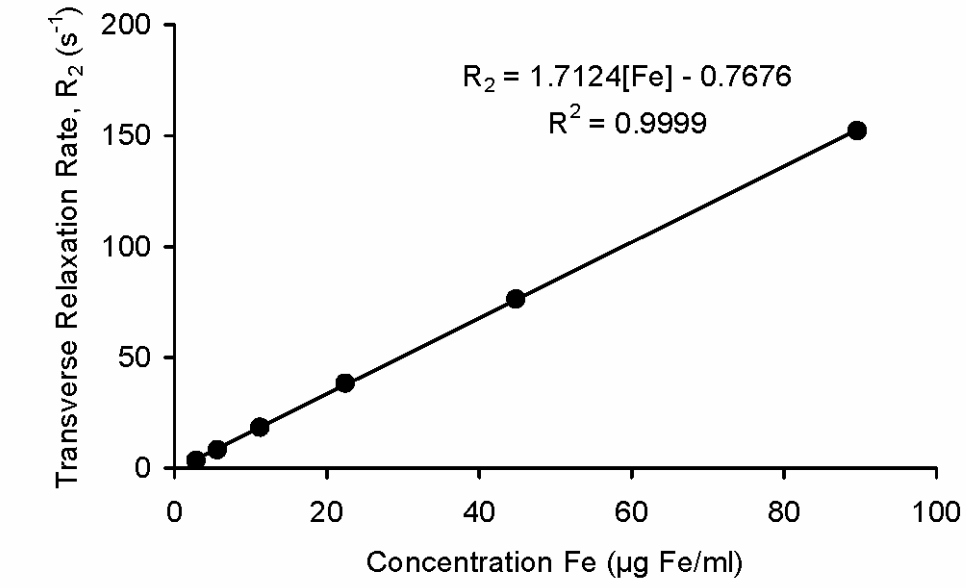

Figure III.3

Figure III.3 shows the linear relationship between magnetite dextran concentration in water and transverse relaxation rate used to calibrate the absolute blood concentration of Fe.

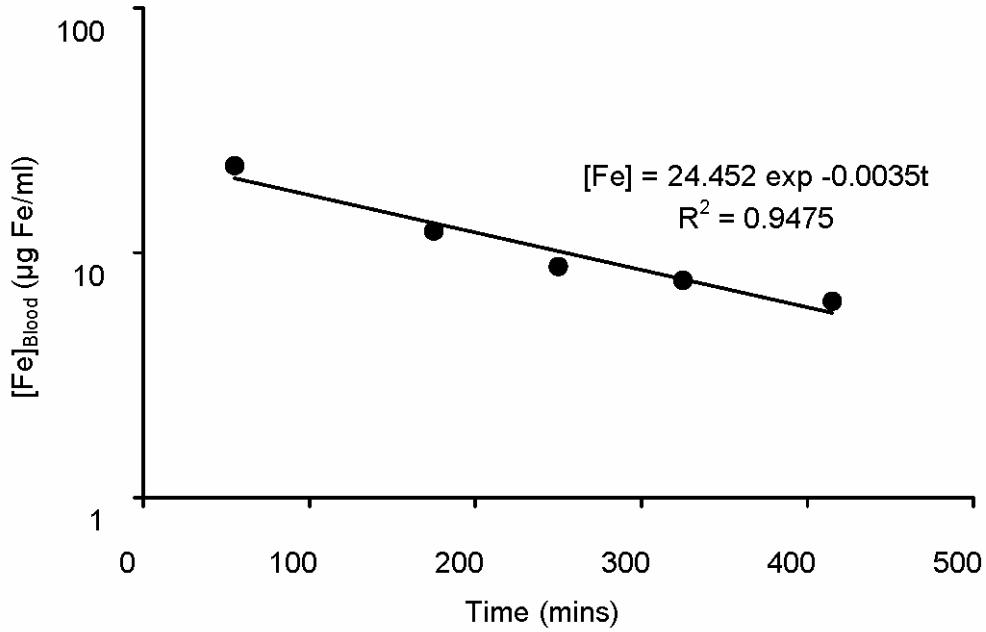

Figure III.4

Figure III.4 shows the calibrated blood concentration of Fe (semi log scale) following administration of 2.8 mgFe/kg (750 µMol/kg) magnetite dextran. Excretion follows monoexponential kinetics with a blood half-life of 198 minutes.

CHAPTER IV: Macaque Anatomical Imaging

IV.1 MICROWIRE PLACEMENT

A major facet of the use of anatomical MRI in a neuroscience setting is the planning of surgical procedures – specifically the guidance of electrode and recording chamber positioning. In cases typified by the following study, I was responsible for acquiring and analyzing all imaging data, formatting it for use in surgical planning, and working with the surgeons in determining the cortical areas of interest. This work was originally published under the title of "Magnetic resonance image-guided implantation of chronic recording electrodes in the macaque intraparietal sulcus" (Scherberger et al., 2003). Hans Scherberger and Igor Fineman served as the chief surgeons during these implantations, with the handler of the particular animal assisting. All electrode recording and analysis was performed by the handler of the monkey: Sam Musallam, Bijan Pesaran or Brian Corneil. Betty Gilliken was involved heavily with the design and set up of both the surgical theatre and procedures, and in several MRI recording sessions.

IV.1.1 Abstract

The implantation of chronic recording electrodes in the brain has been shown to be a valuable method for simultaneously recording from many neurons. However, precise placement of these electrodes, crucial for successful recording, is challenging if the target area is not on the brain surface. Here we present a stereotaxic implantation procedure to chronically implant bundles of recording electrodes into macaque cortical sulci, employing

magnetic resonance (MR) imaging to determine stereotaxic coordinates of target location and sulcus orientation. Using this method in four animals, we recorded simultaneously the spiking activity and the local field potential from the parietal reach region (PRR), located in the medial bank of the intraparietal sulcus, while the animal performed a reach movement task. Fifty percent of all electrodes recorded spiking activity during the first two post-operative months, indicating their placement within cortical gray matter. Chronic neural activity was similar to standard single electrode recordings in PRR, as reported previously. These results indicate that this MR image-guided implantation technique can provide sufficient placement accuracy in cortical sulci and subcortical structures. Moreover, this technique may be useful for future cortical prosthesis applications in humans that require implants within sulci.

IV.1.2 Introduction

Recording electrodes have been implanted in the mammalian brain for the purpose of chronic recording of neural activity since the late 1950's (Strumwasser, 1958; O'Keefe and Bouma, 1969; Kruger and Bach, 1981; for a review see: Schmidt, 1999). Chronic multiple single unit recording has been applied for studying the correlation of neural activity within one or more different brain areas and has provided a new means of recording neural activity under less behaviorally restrained conditions (Humphrey et al., 1970; Fryer and Sandler, 1974; Gray et al., 1989; Fee and Leonardo, 2001). Recent technological progress made it possible to record the spiking activity and the local field potential simultaneously from many tiny electrodes that have been surgically implanted into the brain, while

progress in computer technology and digital signal processing allowed analysis of neuronal population signals virtually in real time with a delay of only a few tenths of a second (Donoghue et al., 1998; Isaacs et al., 2000b; Kralik et al., 2001). Such rapid decoding of neuronal signals is essential for systems that will control an effector in real time, such as a motor neural prosthesis, which must allow instant interpretation of neural commands in order to effectively interface with a device such as a cursor on a computer screen or a robotic arm (Chapin et al., 1999; Wessberg et al., 2000; Serruya et al., 2002; Taylor et al., 2002).

The majority of research groups working in this field are currently focusing on motor and premotor cortical areas to decode limb movements in real time. In contrast to motor and premotor areas, it has been shown that the motor planning activity in the posterior parietal cortex (PPC) could provide additional, and perhaps superior signals for the online decoding of limb movements (Buneo et al., 2002; Meeker et al., 2002; Pesaran et al., 2002; Shenoy et al., 2003). For example, the parietal reach region (PRR) in the PPC, seems to represent reach endpoint positions of upcoming limb movements in visual coordinates, rather than the movement trajectory, and plays a prominent role for sensorimotor transformation (Andersen et al., 1998; Scherberger and Andersen, 2003). In contrast to motor cortical areas, the PPC may be less prone to cortical reorganization in patients with spinal cord injuries that suffer from loss of somatosensory feedback (Merzenich et al., 1984; Lotze et al., 1999; Wu and Kaas, 1999), since vision, the dominant sensory input and error correction signal for this area, remains intact.

Surgically, chronic electrode implantation is harder for areas located in the cortical sulcus than for areas on the cortical surface. For chronic recording from PRR, electrode arrays need to be implanted into the medial bank of the intraparietal sulcus (IPS) to a depth of 4-5 mm below the cortical surface (Fig. IV.1.1). To target PRR, we have developed a novel microwire electrode implantation technique that employs: magnetic resonance (MR) imaging for stereotaxic electrode placement, electrode arrays specifically designed for PRR, the use of alginate gel to protect the exposed cortex, and a neuro-anesthesia protocol that allows a procedure lengths of 8-10 hours. The improved accuracy of this technique allowed us to place a substantial number of recording electrodes into PRR. In the following, we describe the methods and recording results of four implanted animals.

IV.1.3 Methods

All surgical and animal care procedures were in accordance with the National Institute of Health guidelines and were approved by the California Institute of Technology Institutional Animal Care and Use Committee.

To prepare for animal training, a custom-made titanium head post and a dental acrylic head cap (Coralite Duz-All; Bosworth Co., Skokie, Ill) were implanted on each animal in a first surgical procedure. The head cap was secured using titanium bone screws (Synthes, Paoli, PA, USA) for strength in the periphery of the cap and with ceramic screws (Thomas Recording, Germany) around the future skull opening to avoid MR imaging artifacts.

IV.1.3.1 Animal Training

Animals were habituated to sit in a primate chair with their heads fixed in front of a back-projected touch-sensitive screen. They were trained to fixate targets on the screen that were illuminated in red and to reach out and touch targets that were illuminated in green, while their eye position was monitored with an infrared video tracking system (Iscan Inc., Cambridge, MA, USA). Using this paradigm, animals performed a delayed center-out reach movement task, in which the animals first touched and fixated a central fixation position and, after a delay period, reached out and touched one of eight peripheral targets at a distance of 20° visual angle. A juice reward was given after each successfully completed trial.

IV.1.3.2 MR Imaging

MR imaging was performed using a 1.5 T Siemens Magnetom Vision clinical scanner with a conventional knee coil. A 3D Magnetization Prepared Rapid Acquisition Gradient Echo (MPRAGE) sequence (TR 11.4 ms, TE 4.4 ms, 12 deg flip angle, 250 ms inversion time, 600 ms delay time) with a 128x128 matrix (256x256 with zero-padding) and 141x141 mm field of view was used to acquire 118 sections over a distance of 130 mm encompassing the entire head of the subject (Dubowitz et al., 2001b). Four such runs were signal-averaged and refitted to stereotaxic zero as defined by Reid's plane (intersecting the outer openings of both bony ear canals and the lower rims of both orbits). This rotated composite volume was resliced at 0.5 mm spacing, yielding a final image of voxel size 0.55x0.55x0.5 mm

(native resolution: 1.1x1.1x1.0 mm) (Pezaris and Dubowitz, 1999b; Dubowitz, 2002b). Post-acquisition image analysis was carried out using the AFNI software package (Cox, 1996b).

Coronal sections were evaluated, in 2 mm steps from 10 mm posterior to 10 mm anterior of stereotaxic zero, to determine the stereotaxic position and orientation of the IPS. Figure IV.1.2 shows an example of a coronal section (at 6 mm posterior) with the right IPS hitting the cortical surface at 9 mm lateral to the medial plane and at an inclination angle of 30°. In each coronal section, a possible electrode position was then determined, such that the entry point at the cortical surface was located 1–2 mm medial to the sulcus to prevent dimpling and the tip of the electrode targeted PRR 4.5 mm below the cortical surface within the medial bank of the IPS (white line).

IV.1.3.3 Electrode Arrays

For chronic implantation, electrode arrays were constructed from 75 μm Parelene-C insulated tungsten wire with a sharp tip (diameter: 3 μm) and an impedance of 300 kΩ (MicroProbe Inc., Potomac, MD, USA). 32 such electrodes were arranged in four rows of eight (spacing: 0.4 mm) and attached to two miniature connectors (double row 18-contact, Omnetics Inc., Minneapolis, MN, USA). In addition, one ground and one reference electrode (low impedance) were placed at each end of the array. All electrodes were rigidly attached to the connector using epoxy glue. Figure IV.1.3 shows an electrode array before and during implantation.

IV.1.3.4 Electrode Implantation

IV.1.3.4a Anesthesia

Two days before surgery, the animal was started on anticonvulsants (phenytoin 3 mg/kg daily after 6 mg/kg initially) and oral antibiotics (ampicillin 14 mg/kg and clavulanic acid 2.8 mg/kg).

General anesthesia was induced using ketamine (10 mg/kg IM) and atropine (0.04 mg/kg SC) and maintained using isoflurane (1-2%) after endotrachial intubation. Heart rate, respiratory rate, ECG, non-invasive blood pressure, O_2-saturation, expiratory CO_2, and rectal temperature were continuously monitored throughout the procedure. Venous blood gases were analyzed every 1-2 hours using a tabletop blood gas analyzer (I-STAT, East Windsor, NJ, USA). Fluids were continuously replaced through an IV line at the animal's saphenous vein (lactate Ringer's or saline solution at 50 ml/kg/hour). At the beginning of anesthesia, IM antibiotics (amoxicillin 22 mg/kg), steroids (dexamethasone 1 mg/kg), and analgesics (buprenorphene 0.01 mg/kg IM/ 8 hours) were administered. Additional drugs to control for blood pressure (atropine, dopamine), brain swelling (mannitol, flurosemide), and seizure activity (diazepam, phenytoin) were kept at hand. The animal was mechanically ventilated and moderately hyperventilated (end-tidal CO_2 about 30 mmHg) to reduce brain swelling while the cortical surface was exposed.

IV.1.3.4b Procedure

The surgical procedure was performed under sterile conditions. After placing the animal in a stereotaxic head holder (David Kopf, Tununga, CA, USA), the existing head cap was removed to expose the skull overlying the parietal cortex. Using a pneumatic drill (Black Max, Anspach Inc., UK), a 2x4 cm hole was made in the skull over the posterior portion of the IPS based on stereotaxic positions from the MR image. The Dura was opened in a 2x5 mm patch determined from the MR images to lie over the most posterior part of medial bank of the IPS, just anterior to the parieto-occipital sulcus, (approximate stereotaxic coordinates: centered on 8 mm posterior, 5 mm lateral). To protect the cortical surface, the dural patch was elevated with a suture before being opened. The stereotaxic positions of the IPS in situ and in the MR images were then compared and in all cases found to be aligned within 2 mm in the axial plane.

To prevent CSF loss, the dural opening was covered with calcium alginate by dropping equal amounts of alginate (Pronova UP LVG: 20mg in 2ml sterile water; Pronova Biomedical, Norway) and calcium chloride solution (1M) on the exposed cortex, which formed a thin layer of protective gel (Becker et al., 2001).

The electrode array was mounted on a stereotaxic arm and positioned above the dura opening. The array was tilted in the coronal plane according to the guidance angle of the corresponding (coronal) MR image (Fig. IV.1.2) and rotated about the insertion axis, such that the length of the array was aligned with the IPS along the cortical surface.

Figure IV.1.3 shows an intra-operative view of the mounted array during insertion. The array was lowered to the cortical surface and then slowly inserted (0.2 mm/min) until the target depth was reached (4-4.5 mm below cortical surface). The cortical surface and the dura around the electrode were covered with a layer of dural replacement (DuraGen, Integra LifeSciences, Plainsboro, NJ, USA) and a layer of calcium alginate. The inserted array was then fixed to the skull and head cap using dental acrylic before the stereotaxic arm was disconnected from the array. By repeating this procedure, a second electrode array could also be inserted into the medial bank of the IPS. The remainder of the exposed dura was then covered with DuraGen, sealed with calcium alginate against CSF loss, and the skull defect closed with dental acrylic. All arrays were completely embedded in dental acrylic, except for the connector ends. Connectors were protected against dirt and impact by a connector plug and a removable plastic lid that was placed over the arrays and anchored in dental acrylic.

IV.1.3.4c Post-operative Care

After the procedure, the animal was closely monitored for vital and neurological signs. All animals recovered without complications. Systemic analgesics (buprenorphine 0.01 mg/kg SC/8 hours) were administered for several days as needed, to supplement oral analgesia (ibuprophen 5 mg/kg) that was given for 1-2 weeks. Antibiotic medication was administered for two days parenterally (amoxicillin 22 mg/kg IM), then continued orally (ampicillin 14 mg/kg and clavulanic acid 2.8 mg/kg) for 10-14 days. Anticonvulsants were tapered off within the first post-operative week. Animals were allowed to recover

completely from surgery (10-14 days) before experiments began.

IV.1.3.5 Recordings

Spiking activity and LFPs were recorded simultaneously from 32 electrodes using a multichannel acquisition processor (MAP, Plexon Inc., Dallas, TX, USA): single units were isolated online using time-voltage windows and their timing and spike waveforms stored on disk. LFP signals were amplified, low-pass filtered (90 Hz), and digitized as a continuous signal at a sampling rate of 1000 Hz.

IV.1.4 Results

Four animals (T, Z, S, C) were implanted with chronic electrode arrays using the surgical technique described above. After full recovery from the procedure, identifiable single unit spiking activity could be recorded from every implanted electrode array. Overall, 50% of all electrodes (T: 31%, Z: 53%, S: 60%, C: 50%) had identifiable spiking activity during the first two months after implantation, indicating that these electrodes were placed within the gray matter of the IPS. On any given experimental day, clearly identifiable spiking activity was recorded on average from 28% of all electrodes (T: 22%, Z: 25%, S: 35%, C: 32%).

The spatial distribution of electrodes exhibiting spiking activity is given in Fig. IV.1.4. Two out of seven arrays (T and Z anterior) showed a strong medio-lateral patterning with many electrodes presenting spiking activity in the two rows adjacent to the IPS while

electrodes in the two distant rows had almost no spiking activity. This suggests that these two arrays were only partially inserted into the gray matter of the medial bank of the IPS. In the five other arrays (S, C, and Z posterior), the distribution of electrodes with spiking activity did not show such patterning, suggesting that these arrays were more completely inserted into the target area.

The spiking activity of many units was modulated and showed spatial tuning during a delayed center-out reaching task to 8 peripheral locations (Fig. IV.1.5A). Figure IV.1.5B shows an example of nine simultaneously recorded single units that were spatially tuned. The spiking activity of these units show significant, and in some cases even dramatic, differences between reaches to the preferred and the non-preferred target direction, in accordance with previous studies of this area that used the standard single unit recording technique (Kalaska, 1996; Andersen et al., 1997; Snyder et al., 1997).

In addition to spiking activity, we also recorded the LFP activity from the vast majority of the implanted electrodes (>95 %). The spectral power of the LFP signals was analyzed using multi-taper estimates (Percival and Walden, 1993; Pesaran et al., 2002) and, for many recording sites, showed modulation and directional tuning in the reach movement task, in agreement with a previous report using standard single unit recording techniques (Scherberger et al., 2001).

IV.1.5 Discussion

Using a novel approach to implant multiple electrode arrays with stereotaxic MR imaging guidance, we chronically inserted multiple microwire electrode arrays into the medial bank of the IPS 4-5 mm below the cortical surface with a minimal dural opening. Subsequent simultaneous recordings revealed identifiable spiking activity at about 50% of all implanted electrodes within the first two post-operative months. The pattern of active channels within most of the arrays suggested that the arrays were completely inserted within cortex (the lack of spiking activity on some electrodes being due to their distance from a particular cell rather than being outside of cortex). More generally, our method could be applied to microwire implantation in other brain structures, such as subcortical areas and other cortical sulci (Deadwyler et al., 1996; Nicolelis et al., 1997; Baker et al., 1999).

Key elements for the success of this method are the MR imaging guidance, the design of electrode arrays, particularly sharp electrode tips and an optimized array geometry, as well as the use of alginate gel to protect the exposed cortex against damage and to minimize brain shift associated with loss of cerebro-spinal fluid. In addition, a neuro-anesthesia protocol similar to human neurosurgical practice allowed us to safely extend the procedure to 8-10 hours. During the procedures the animals were intubated and blood gases, fluid balances, and electrolytes were carefully monitored and controlled (Logothetis et al., 1999b; Kralik et al., 2001).

Verification of electrode placement with histology was not part of this study, since all

animals are currently alive and part of ongoing studies. We are nonetheless convinced that the majority of electrodes are implanted in the proper target location (PRR) for the following reasons: First, Dubowitz (2002b) showed that the use of MR image-guided stereotaxic coordinates has an accuracy of 1.3±0.3 mm. Second, our technique involves the direct visualization of the IPS during surgery, which further improves the placement accuracy. Finally and most importantly, our recordings confirm physiologically that the electrodes are in the target area: spiking activity identifies 50% of all electrodes to lie in gray matter and many of those signals show significant directional tuning for reaching. Furthermore, we tested the neural activity in two animals (C, S) using both delayed saccade and delayed reach tasks and found the neural responses significantly larger for reach movements than for saccades, as expected for PRR (Snyder et al., 1998). While we are therefore confident that our electrodes are accurately placed in PRR, we nevertheless plan to develop a positive placement verification method, like post-surgical MR imaging, which will become important in particular for implantations in less explored brain areas.

IV.1.6 Neural Prosthesis

The ability to accurately place a substantial number of electrodes into a specified cortical area is particularly important in the emerging field of neural prosthetics, where large populations of neurons need to be decoded online to predict the trajectory or end-position of impending limb movements. Several groups have chronically implanted electrode arrays in motor areas predominantly on the cortical surface and were able to use the simultaneously recorded single- and multi-unit activity to control a robotic or a virtual arm:

Nicolelis and colleagues implanted blunt microwires both in the rat and in new-world (owl) monkeys (Chapin et al., 1999; Nicolelis et al., 1999; Wessberg et al., 2000; Kralik et al., 2001), while Schwartz and colleagues implanted microwire arrays with sharp tips into the cortical surface of old-world monkeys (macaques) (Isaacs et al., 2000b; Taylor et al., 2002). Similar results were also found by Donoghue and colleagues using micro-machined silicon 100-electrode arrays (Bionics Inc, Utah, USA) that were pneumatically inserted into the macaque premotor and motor areas (Hatsopoulos et al., 1998; Serruya et al., 2002).

Our approach allows us to record reach-movement related spiking activity and the LFP simultaneously from many electrodes in PRR of old world monkeys, which is located within a cortical sulcus. This method could be advantageous in general for electrode implantation in primates with a high degree of encephalization, where a substantial amount of cortex is localized in cortical sulci, and for human implants, where the encephalization is even greater. We have used the signals from the array implants to successfully decode online the intended reach trajectories without the animals emitting any behavior. These results will be reported in a subsequent publication.

IV.1.7 Acknowledgement

We thank K. Weaver for animal care, R. Bhattacharyya, B. Greger and V. Shcherbatyuk for technical support, and A. Schwartz, and J. Williams for early, helpful discussions. This work was supported by the Christopher Reeve Paralysis Foundation (HS), the Human Frontier Science Program (BDC), the James G. Boswell Foundation, the Defense

Advanced Research Projects Agency, and the National Eye Institute.

IV.2 ELECTRODE LOCALIZATION

The production of imaging data for purposes of determining the specific area of a neruophysiological electrode recording accounted for the broadest experience at different MRI systems. Acquisition of data from different animals led to the use of no less than six different MRI magnets, ranging from a rather unique and somewhat outmoded 0.5 T mobile scanner housed in a semi trailer, to the current advanced 3 T whole body unit present at Caltech's Moore facility. Similarly, constant advances in processing software continuously changed and expanded the methods available for visualization and presentation of the anatomical data. Truly, this opportunity provides a sound foundation for any further career in neuroimaging.

IV.2.1 Abstract

Magnetic resonance imaging is of use in the neurosciences for determining the sites from which electrophysiological recordings have been measured. Imaging the anesthetized animal provides a high-resolution image with minimal motion clearly demonstrating the orientation and position of the recording chamber(s) and many electrode penetrations. Acquisition time can be adjusted to accommodate handling of the animal without sacrificing the quality of the image. Multiple animals used in the same experiment can be compared for similarities and differences in recording sites. Recording sites can be identified relative to other cortical landmarks, or to the physiology of the animal when used

in conjunction with a 3D rendering technique.

IV.2.2 Introduction

For in vivo electrophysiology of the brain, the site of recording is as important as the recordings themselves. Classically, the location of electrode penetrations has been established by viewing histological preparations of the area in question, at times with the aid of a preinjected radioactive tracer. While providing accuracy limited only by the resolving power of microscopy, this technique required the sacrifice of the subject and an end to data acquisition. With the application of magnetic resonance imaging (MRI), the subject may now be spared while still maintaining a high level of resolution for localization. A single session can produce a three dimensional image of the whole head of a typical macaque at submillimeter resolution within minutes. Preparing the animal with general anesthesia ensures no gross motion will interfere with the quality of the scan. Care must be taken to limit the amount of magnetically susceptible metal involved in the recording apparatus involved in the animal's implantations. Particularly, if any screws or posts are included, the use of a ceramic material or plastic will limit the distortion caused to the scan. If metal must be used, titanium is suggested as it causes a far smaller image artifact than a ferromagnetic material such as iron or steel.

To localize the site of electrode penetrations, it is most useful to reference the position of the area relative to surrounding landmarks or the stereotaxic position of the site for comparison to a standard atlas. Stereotaxic positioning may be accomplished by rotating

the image volume to be orthogonal with a plane defined by the center of each inner ear canal and one or both inferior margins of the bony orbit (Reid's plane.) This will put the image in an orientation common with stereotaxic coordinates. Zeroing the coordinate frame to the midpoint of the line defined by the two ear canal locations then allows measurements to be read off the image in an isometric fashion. This method has a drawback in that the axis of an electrode penetration rarely lies orthogonal to the stereotaxic positioning. While a point along the path of the electrode may be referenced in this manner, it is rarely used, in favor of positioning the images parallel to the long axis of the electrode or chamber.

To perform such an orientation, it is necessary to visualize the orientation of the chamber on the anatomical image. This presents a difficulty in that a plastic or other common chamber material will not appear on a MRI image. Fluid within the chamber may be discernable, but the volume may not be sufficient. Filling the chamber with a solution of a highly visible contrast agent, such as a gadolinium salt, will enable the easy visualization of this volume. Should axial orientation require aligning the image to a point other than the most anterior aspect of the chamber, additional references such as a MRI fiducial marker or specialized chamber plug may be used.

When an image aligned with the chamber walls is produced, care must be taken to faithfully represent the visualization of the penetration site. For a recording site deep within a sulcus, the plane of the image is often such that surrounding structures are easily

discernable. However, if the recording was preformed on the surface of cortex, visualization with a cross section or a plane deep to the site may be appropriate. A cross-sectional view will allow the length of the electrode track to be seen along with the precise point of intersection with the surface of the brain. Choosing a plane deep to the site of recording perpendicular with the track will reference the site to surrounding landmarks, such as sulci, ventricles and nuclei, with minimal distortion of the actual area under investigation.

IV.2.3 Materials and Methods

IV.2.3.1 Animal Subjects

Anesthesia was induced by ketamine (10 mg/kg IM) and atropine (0.04 mg/kg SC) and maintained using 1-2% isoflurane. Pulse and arterial oxygen saturation were measured using a magnet-compatible pulseoximeter. Blood pressure was determined on demand using a remotely triggerable pediatric cuff (Invivo Research, Orlando, FL). Respiration was monitored by direct sight of the animal's chest and by observation of a respiration bladder placed in line with the endotrachial tube. Cortical recording chambers were filled with a solution of 5 mg/mL gadopentetate dimeglumine (trade name Magnevist from Berlex Laboratories, Wayne, NJ).

IV.2.3.2 MR Imaging

Magnetic resonance (MR) imaging was performed on a 3 T Siemens Trio scanner with 40 mT/m gradients (200 μs rise time) using an 8-channel high-resolution head array coil (MRI

Devices, Waukesha, WI) as a transceiver. Anatomical images were acquired using a slice-selective saturation recovery magnetization-prepared rapid-acquisition gradient echo sequence (TR 1400 ms, TE 3.49 ms, TI 670 ms, 12 deg flip angle, 170 Hz/Px bandwidth.) 160 images were acquired sagittally with 0.7 mm slice thickness using an in plane field of view of 168 x 168 mm on a 256 x 256 base matrix, yielding a final native voxel resolution of 0.656 x 0.656 x 0.7 mm. These images were realigned via multi-planar reformat to recording chamber landmarks using Siemens Syngo software (version MR 2003T DHHS.) This rotated volume was resliced at 0.7 mm spacing along the z-axis of the chamber and visualized using the AFNI software package (Cox, 1996a). 3D rendering was accomplished using the BrainVoyager software suite (Brain Innovation, Netherlands.)

IV.2.4 Results

Magnetic resonance imaging of three macaque monkeys (R, S and T) was performed after each animal had been a subject in multiple electrophysiological recording experiments. Monkey T was imaged to determine the orientation of electrodes placed within a single lateral recording chamber. Monkeys R and S each had two recording chambers, a midline chamber placed anterior to the intra-aural line and a parietal chamber. Here, the relative position of each animal's midline/anterior chamber is compared. Although all animals had numerous metallic implants, not limited to anchor screws, headposts and electrical connectors, all artifacts produced by these materials were sufficiently far from the chamber to produce little or no difficulty in interpreting the images. All image volumes were aligned to the long axis of the recording chamber and zeroed to the chamber center to

facilitate use by the researcher in determining chamber coordinates of a single penetration.

For monkey T, an image was chosen deep (~7 mm) to the surface of cortex which provided clear presentation of the superior temporal and lateral sulci (Figure IV.2.1.) The site of electrode recording was determined to be on the surface of the superior temporal gyrus adjacent to the most posterior aspect of the lateral sulcus. A rendered surface of the animal's head confirms the extreme lateral positioning of the chamber and aids in the visualization of the recording site (Figure IV.2.2.)

Electrode tracks from monkeys R and S are depicted in cross section (Figures IV.2.3 and IV.2.4) and by a deep plane (Figures IV.2.5 and IV.2.6). The cross-sectional images show the extent of the chamber walls and the central axis of the chambers, representing the span of cortical surface on either side of the midline available for recording. The deep planes represent the whole area of the chamber shown in reference to the surrounding sulci. For monkeys R and S, deep levels (~8-10 mm) were chosen to clearly show the arcuate, primary and central sulci. Three-dimensional rendering of each animal (Figures IV.2.7 and IV.2.8) allows the recording sites to be compared easily and with additional physiologic cues.

IV.2.5 Summary

Anatomical imaging using a 3T Siemens Trio MRI system was performed on three macaque monkeys previously used in cortical electrophysiology experiments. All three

subjects had a previously mounted head restraint containing a recording chamber. For the purposes of imaging, the chamber was filled with a gadolinium contrast agent (as gadopentetate dimeglumine) which facilitated visualization of the inner volume. Images were reconstructed in plane with the axis of the chamber and rendered in 2D flat slices and 3D whole head reconstructions. Projections of the extent of the chamber walls were used to determine the central point of the chamber, which would directly correspond to microdrive coordinates used in experimental placement of the electrode. Multiple sites of electrode positions could be discerned by examination of the images for small susceptibility defects left along the track of a recording penetration. Comparison between animals with chambers thought to be positioned similarly allows for the clear and precise determination of variations of placement and anatomy between the subjects. For measurements taken at the surface of cortex, a deep plane was used for actual localization due to the ease in viewing the relative positions of surrounding landmarks. The 3D rendered images sacrifice an orthogonal presentation of the image plane for additional information such as easy visualization of the anterior-posterior orientation which may aid a viewer. Additionally, visualization of recording chambers placed at extreme angles may benefit from the 3D reconstruction as 2D images are likely to be wholly different from commonly understandable stereotaxic sections.

IV.2.6 Acknowledgement

Thanks go to Betty Gillikin, Kelsie Pejara and Lea Martin for assistance with animal handling. Steve Flaherty provided technical assistance during the scanning sessions. This

work was funded in part by a James G Boswell Professorship, a medical scientist training program grant from the National Institutes of Health and the UCLA Aesculapians, and an ARCS Fellowship.

IV.3 IMPLANTABLE MRI SENSITIVE FIDUCIAL BEADS

If an experimental animal is to be scanned repeatedly over the course of months or years, it is often advantageous to register the images to determine the effects of growth or other concerns on cortical anatomy. Biologic landmarks can change rapidly, particularly with young animals or areas subject to a disease process, and are therefore unsuitable for registration targets. Metal implants typically survive through the experimental life of the subject, barring the total replacement of a head cap, but are difficult to precisely localize on images due to susceptibility artifacts. Filling a recording chamber with contrast media aids in registration, but such a device is not always present, and is clearly not usable if the chamber is replaced or repositioned. Fortunately, the space on an existing or new animal head cap may be used for the placement of fiducial markers. A set of implantable glass beads filled with contrast media were developed for such use and placed in the head cap material of an experimentally active macaque as an alternative to conventional temporary markers (Figure IV.3.1). The beads were visible upon imaging with standard MRI techniques and provided permanent fiducials for registration of future images (Figure IV.3.2).

IV.3.1 Methods

IV.3.1.1 Fiducial Beads

Common glass capillaries were flame sealed at one end and blown to a bead size of approximately 3 mm in diameter. The bead was detached and filled with a solution of 50 mg/mL gadopentetate dimeglumine (tradename Magnevist from Berlex Laboratories, Wayne, NJ). The bead was then sealed with a small amount of epoxy to prevent loss of the solution.

IV.3.1.2 Bead Implantation

Wells large enough in diameter to accommodate the bead and approximately 1 cm deep were excavated in the dental acrylic head cap material. The fiducial was placed in the well and sealed in place with a colored acrylic to identify position of the bead for ease of possible future head cap modifications.

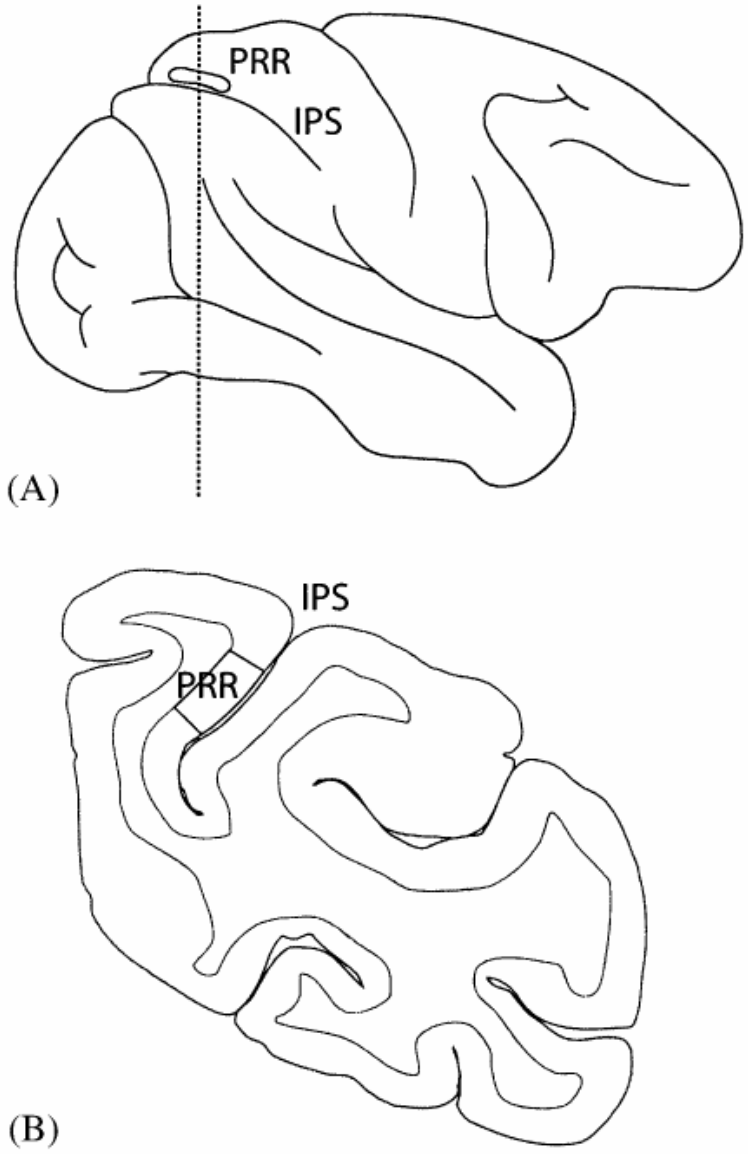

Figure IV.1.1

Lateral view and coronal section of a macaque brain. A: Lateral view. Gray mark: cortical surface area above the parietal reach region (PRR). B: Coronal section of one cortical hemisphere (6 mm posterior of inter-aural line; marked by dotted line in A). Gray area: PRR, located in the medial bank of the intraparietal sulcus (IPS).

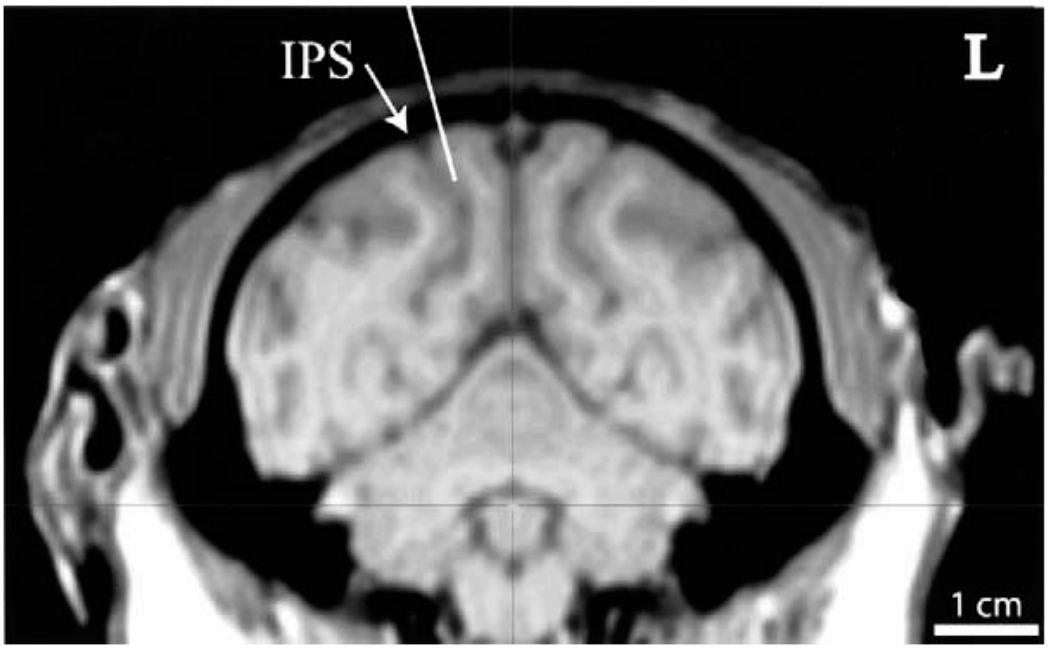

Figure IV.1.2

Magnetic resonance image, coronal section (6 mm posterior of inter-aural line). White line: intended electrode array insertion with the tip of the electrodes located in the medial bank of the intraparietal sulcus (IPS), about 4.5 mm below the cortical surface. L: left side. Scale: 1 cm. Fine dark lines: stereotaxic coordinate frame axes.

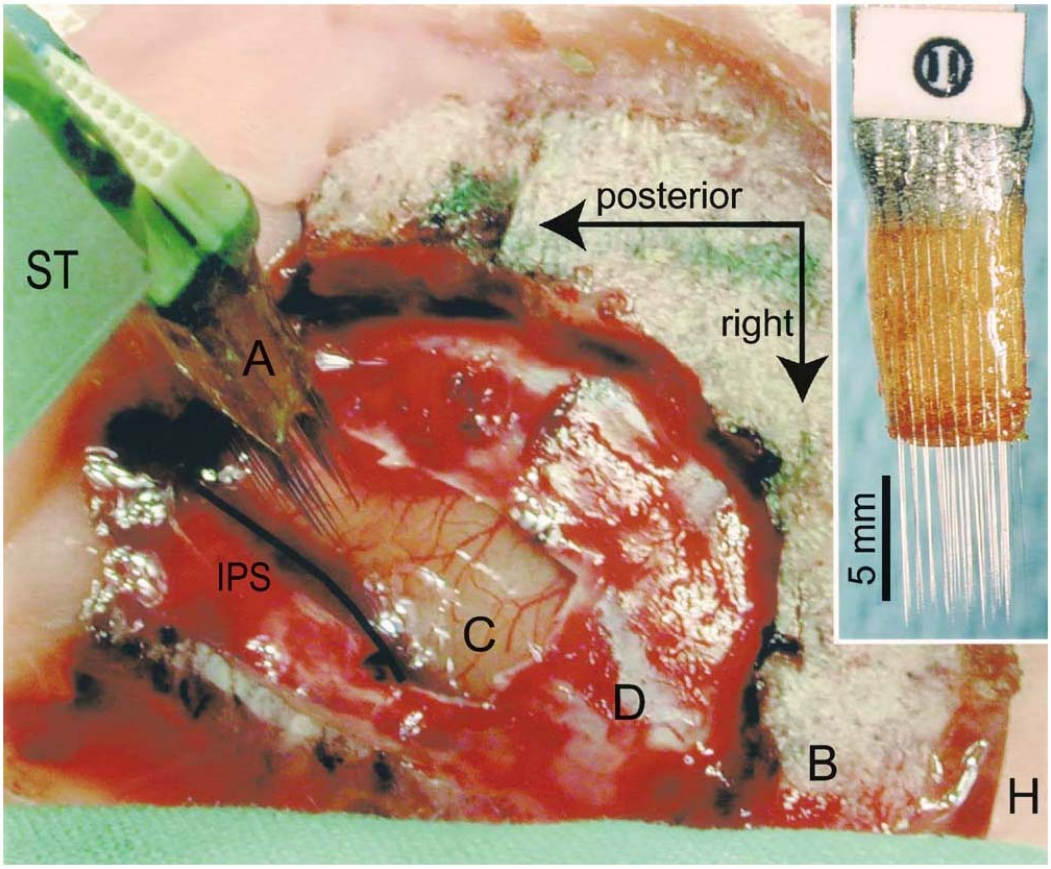

Figure IV.1.3

Intra-surgical view of microwire electrode insertion. Surgical layers from center to periphery: cortex (C), dura (D), skull bone (B), and dental acrylic head cap (H). Horizontal arrow: posterior direction at midline, downward arrow: rightward direction. Curved thick line: right intraparietal sulcus (IPS). Electrode array (A) is connected to a stereotaxic holding apparatus (ST) with its electrode tips penetrating the medial bank of the IPS. Inset: Microwire array (MicroProbe Inc.) with 32 recording electrodes.

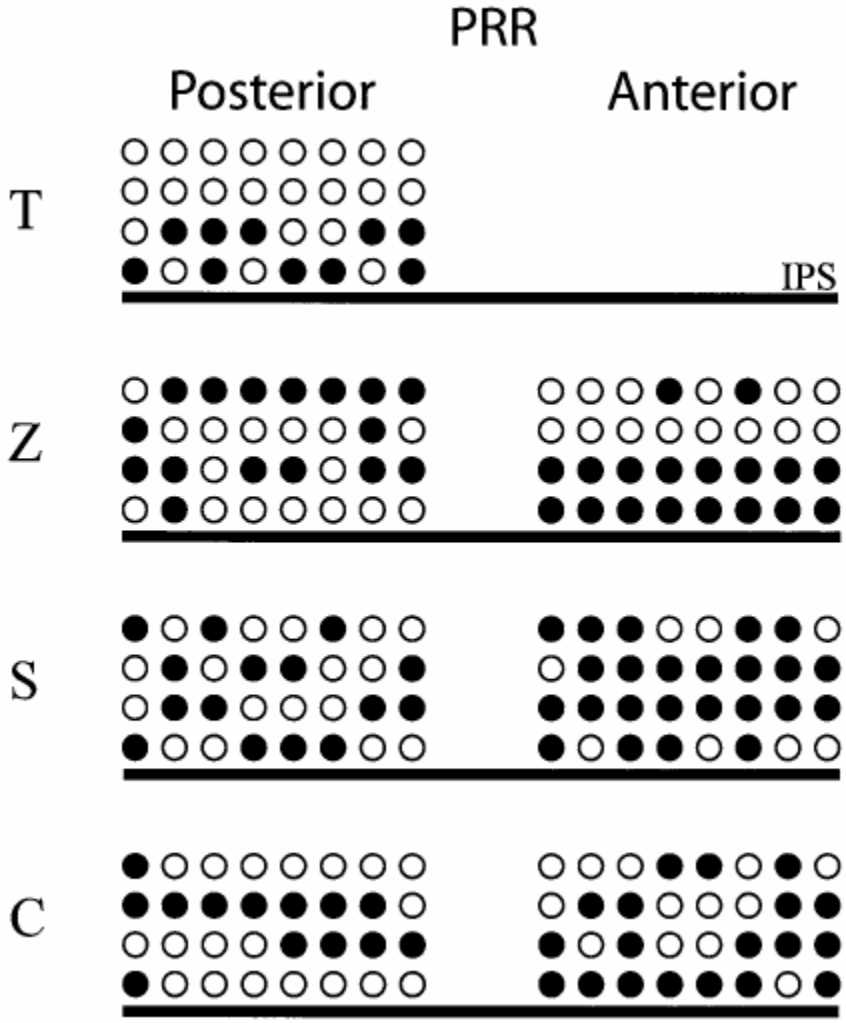

Figure IV.1.4

Spatial distribution of electrodes with spiking activity. Implanted PRR electrode arrays (one in animal T, two each in animals Z, S, and C) are presented as array schematics (8x4 circles) that are positioned according to the array location within PRR (posterior or anterior) and the IPS (black line). Filled circles: electrodes that presented spiking activity at least for one day during the first two post-operative months. Open circles: electrodes with no spiking activity.

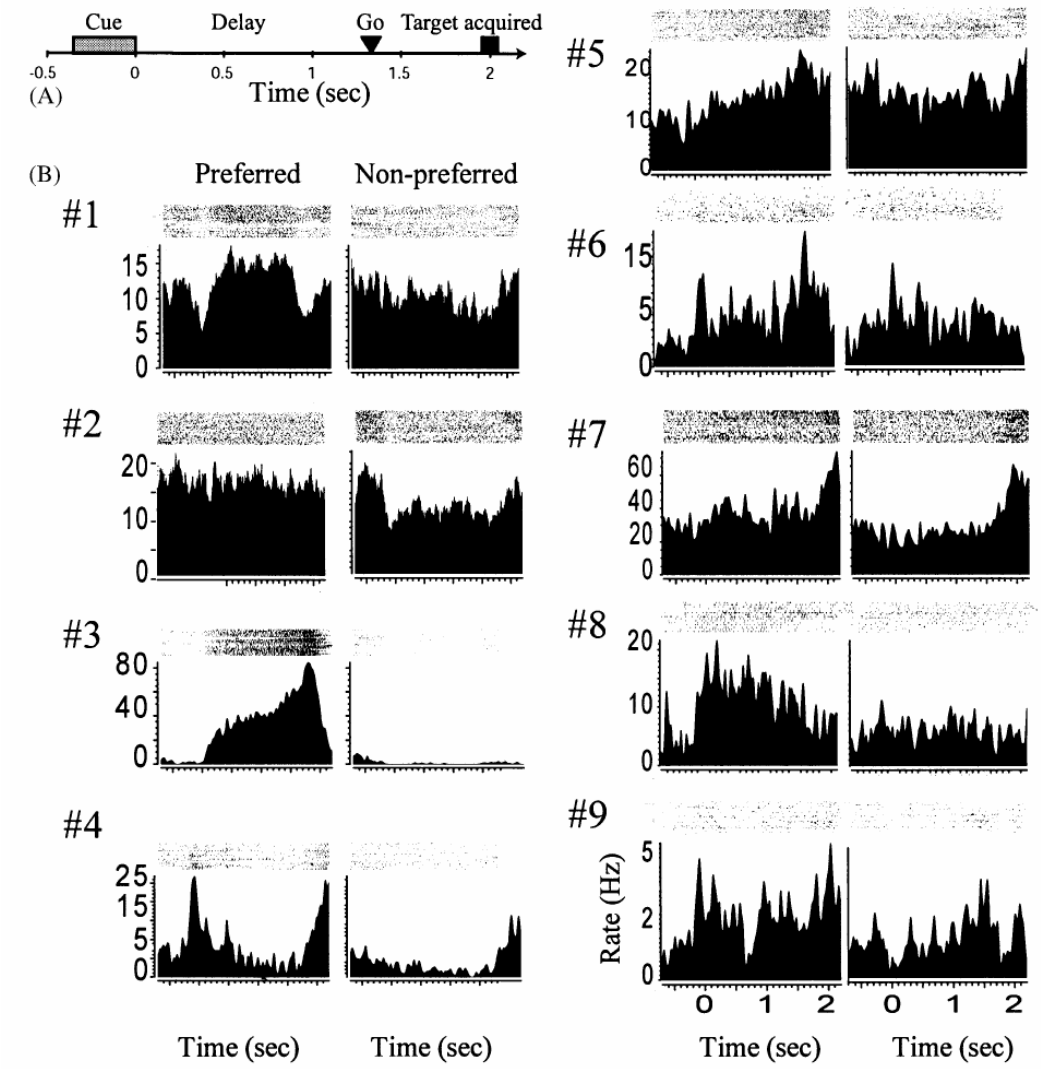

Figure IV.1.5

Spiking activity during the delayed reaching task. (A) Time axis of the delayed center-out reach movement task. After the animal fixated and touched a central fixation point (not shown), a visual cue was presented in 1 out of 8 possible target locations for 0.3 sec (gray horizontal bar). In a variable delay period (1.2–1.5 sec), the animal then had to plan, but not execute, a reach movement to that target, until the central fixation point was extinguished, which served as a Go-signal (arrowhead) for the start of the movement

(square: mean time when target was acquired). Target directions were randomly interleaved in subsequent trials. (B) Example of 9 simultaneously recorded spiking units (#1–9) that show spatial tuning during this task. Spiking activity is presented in the preferred and non-preferred direction of each unit. In each panel, spike rasters (with individual rows of dots depicting the timing of action potentials during one trial) are presented on top of a peristimulus time histogram that illustrates the trial-averaged spiking activity (at least 40 trials). Spike rasters and histograms are aligned to the cue offset (0 sec). All units show significant tuning in the cue, delay, or movement period.

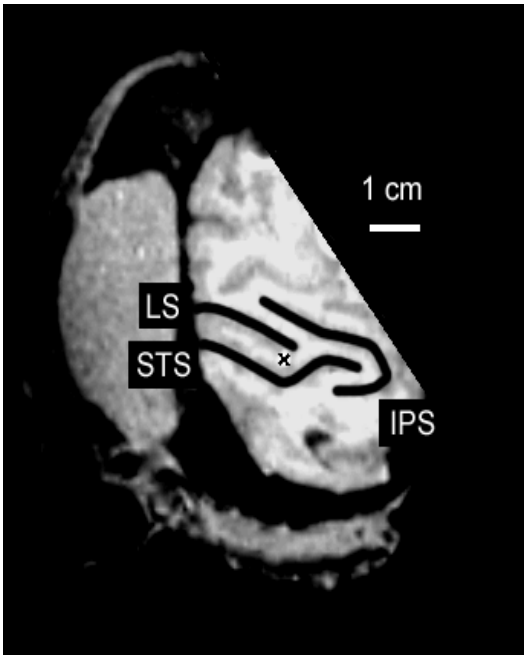

Figure IV.2.1

MRI image of cortex of monkey T taken at a plane perpendicular to the long axis of the recording chamber. Image is aligned such that the top of the figure is in the direction of chamber north. Major sulci near the site of electrode penetration are identified: superior temporal sulcus (STS), lateral sulcus (LS) and intraparietal sulcus (IPS.) Main site of electrode penetrations is identified proximal to the posterior extent of the lateral sulcus (X.)

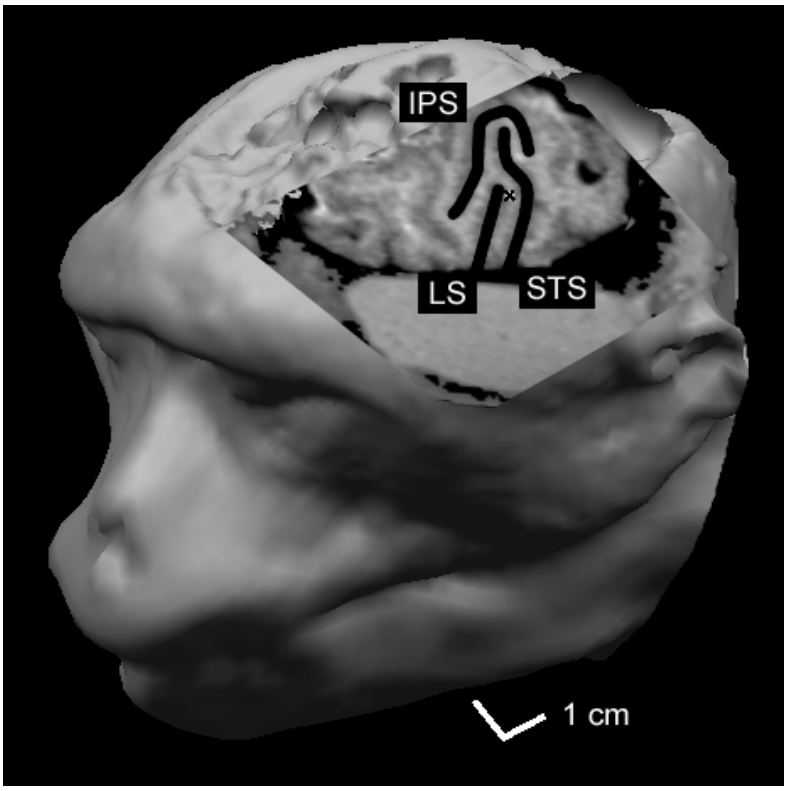

Figure IV.2.2

Three dimensional rendering of entire head of monkey T. Image cut out is in plane with Figure IV.2.1, and is perpendicular to the long axis of the recording chamber. Major sulci near the site of electrode penetration are identified: superior temporal sulcus (STS), lateral sulcus (LS) and intraparietal sulcus (IPS.) Main site of electrode penetrations is identified proximal to the posterior extent of the lateral sulcus (X.) The rough surface at the crown of the animal's cranium represents artifact introduced by the hardware of the head fixation apparatus and is not indicative of actual topology.

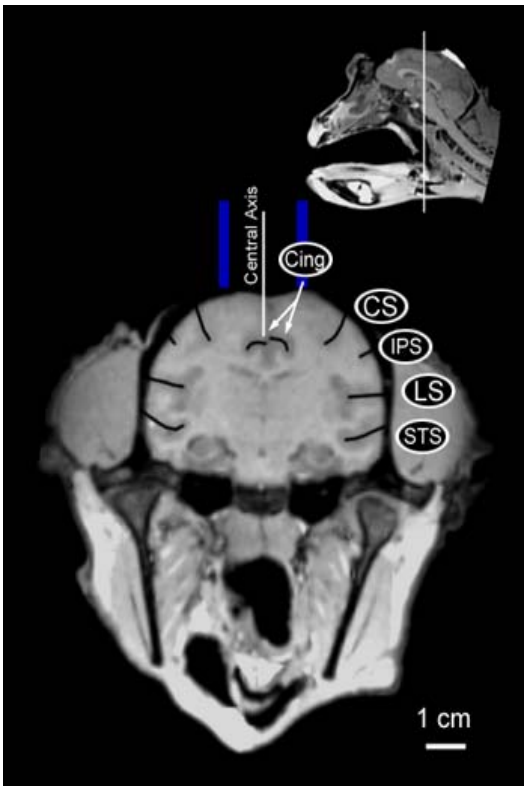

Figure IV.2.3

Coronal image of monkey R, aligned to present a cross section parallel to the center of the recording chamber. Inset shows level of image on a midline sagittal image. Blue bars indicate the extent of the recording chamber walls. The central axis of the recording chamber is represented to depict the point at which an electrode would contact the surface of cortex. Length of central axis projection is for clarity only and does not represent the depth at which measurements were made as most were surface recordings. Major sulci are identified: cingulate sulcus (Cing), central sulcus (CS), intraparietal sulcus (IPS), lateral sulcus (LS) and superior temporal sulcus (STS.)

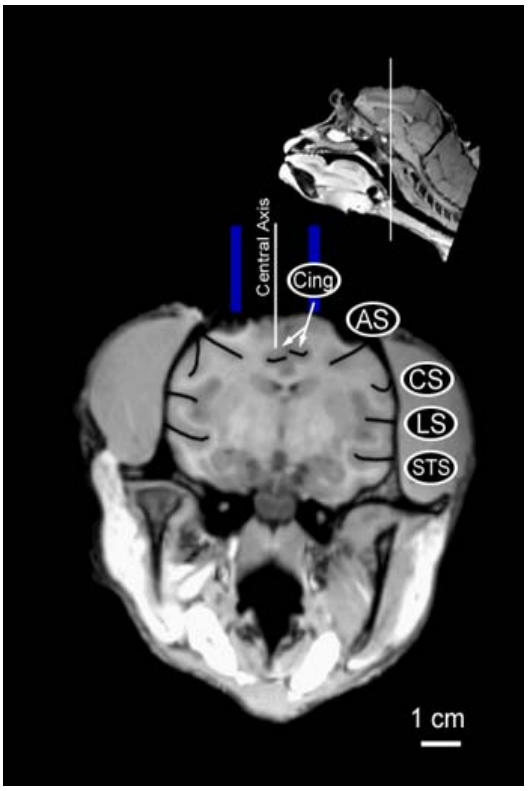

Figure IV.2.4

Coronal image of monkey S, aligned to present a cross section parallel to the center of the recording chamber. Inset shows level of image on a midline sagittal image. Blue bars indicate the extent of the recording chamber walls. The central axis of the recording chamber is represented to depict the point at which an electrode would contact the surface of cortex. Length of central axis projection is for clarity only and does not represent the depth at which measurements were made as most were surface recordings. Major sulci are identified: cingulate sulcus (Cing), arcuate sulcus (AS), central sulcus (CS), lateral sulcus (LS) and superior temporal sulcus (STS.)

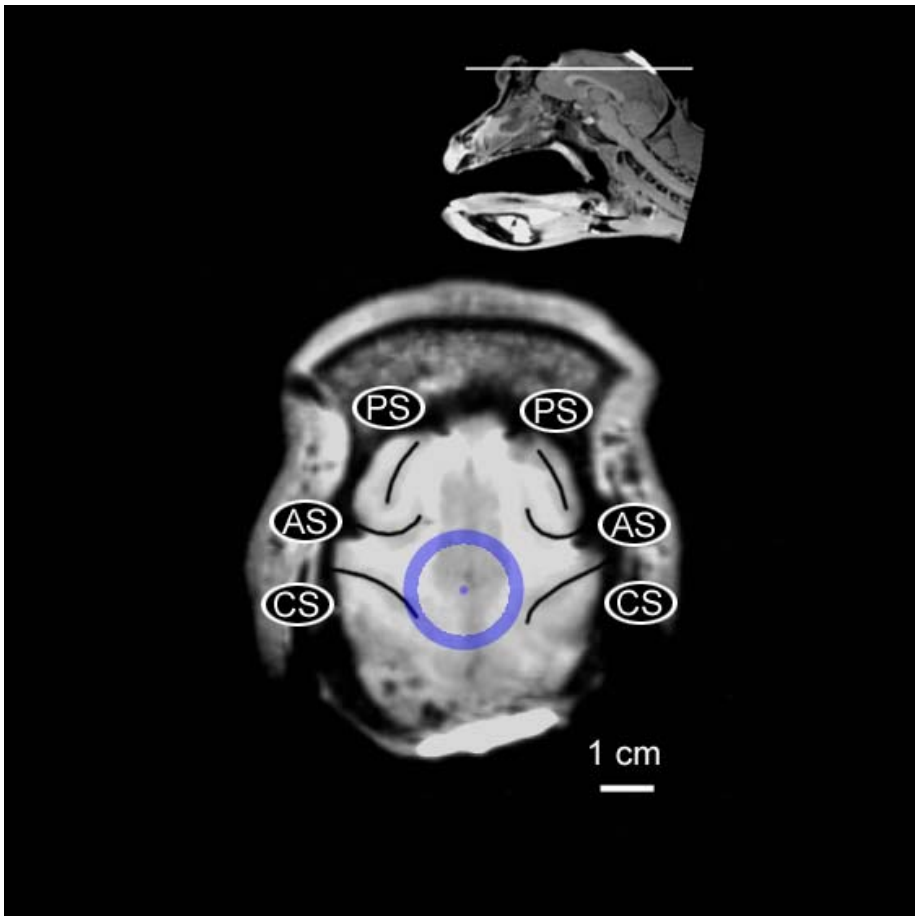

Figure IV.2.5

Axial image of monkey R, aligned to show orthogonal cross section of the recording chamber. Image is aligned such that the top of the image corresponds to chamber north. Chamber wall is represented by the blue circle, with the central axis of the chamber shown by a blue point. Level of image (see inset) was chosen to clearly represent surrounding sulci: central sulcus (CS), arcuate sulcus (AS) and principal sulcus (PS.) Luminosity at the posterior aspect of the image is due to contrast media present in the secondary parietal chamber.

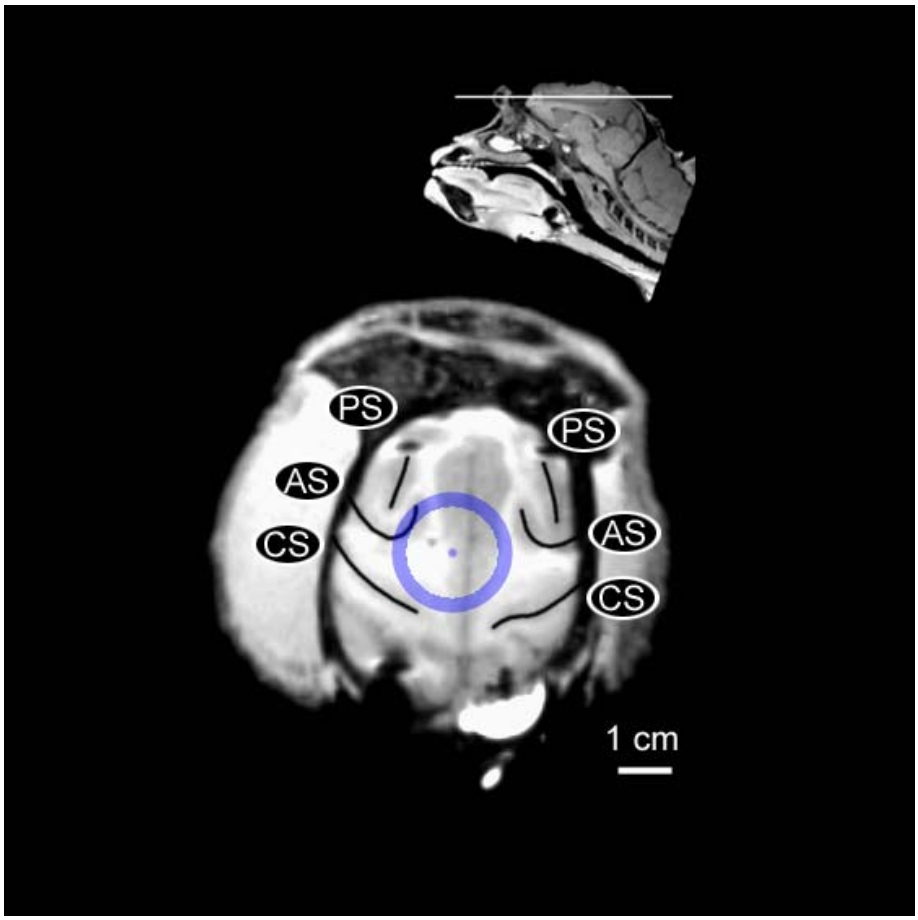

Figure IV.2.6

Axial image of monkey S, aligned to show orthogonal cross section of the recording chamber. Image is aligned such that the top of the image corresponds to chamber north. Chamber wall is represented by the blue circle, with the central axis of the chamber shown by a blue point. Level of image (see inset) was chosen to clearly represent surrounding sulci: central sulcus (CS), arcuate sulcus (AS) and principal sulcus (PS.) Luminosity at the posterior aspect of the image is due to contrast media present in the secondary parietal chamber.

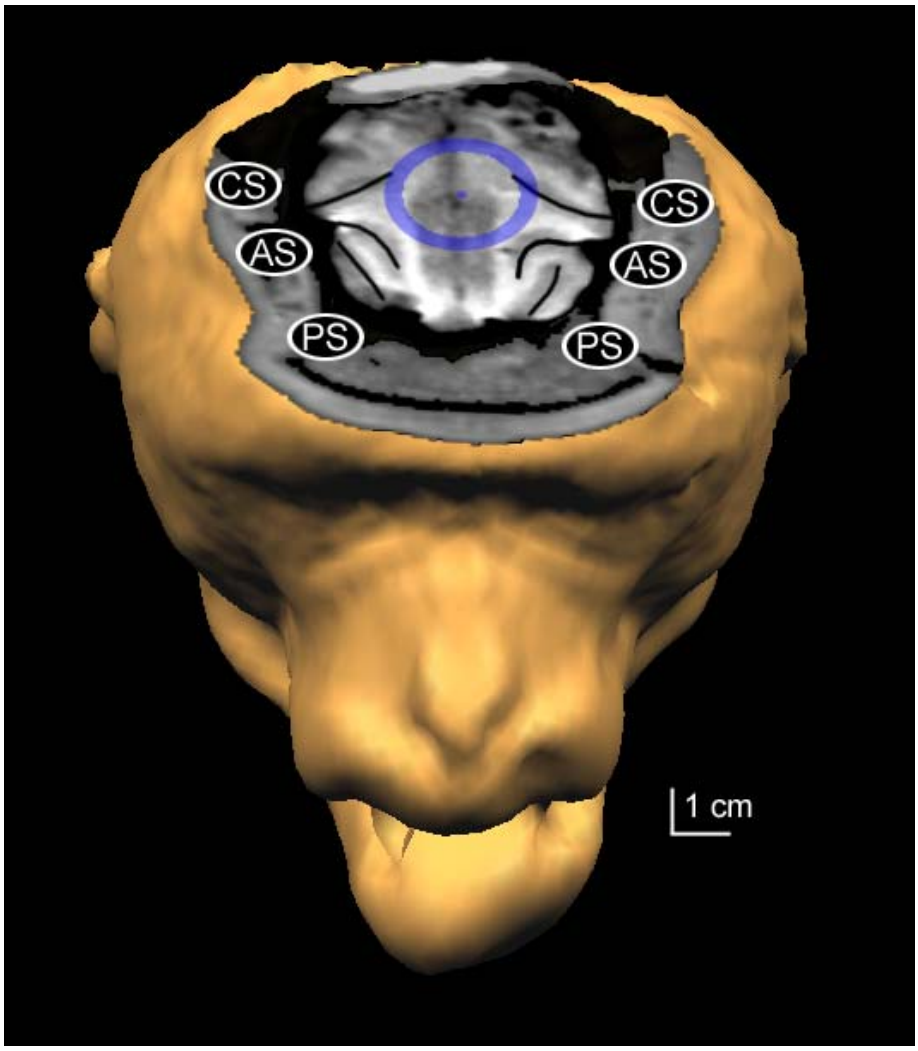

Figure IV.2.7

Three dimensional rendering of the whole head of monkey R, with a plane cut level with Figure IV.2.5 and orthogonal to the recording chamber. Chamber wall is represented by the blue circle, with the central axis of the chamber shown by a blue point. Scale bars differ in horizontal and vertical dimensions as the image is a perspective view. Major sulci are identified: central sulcus (CS), arcuate sulcus (AS) and principal sulcus (PS.)

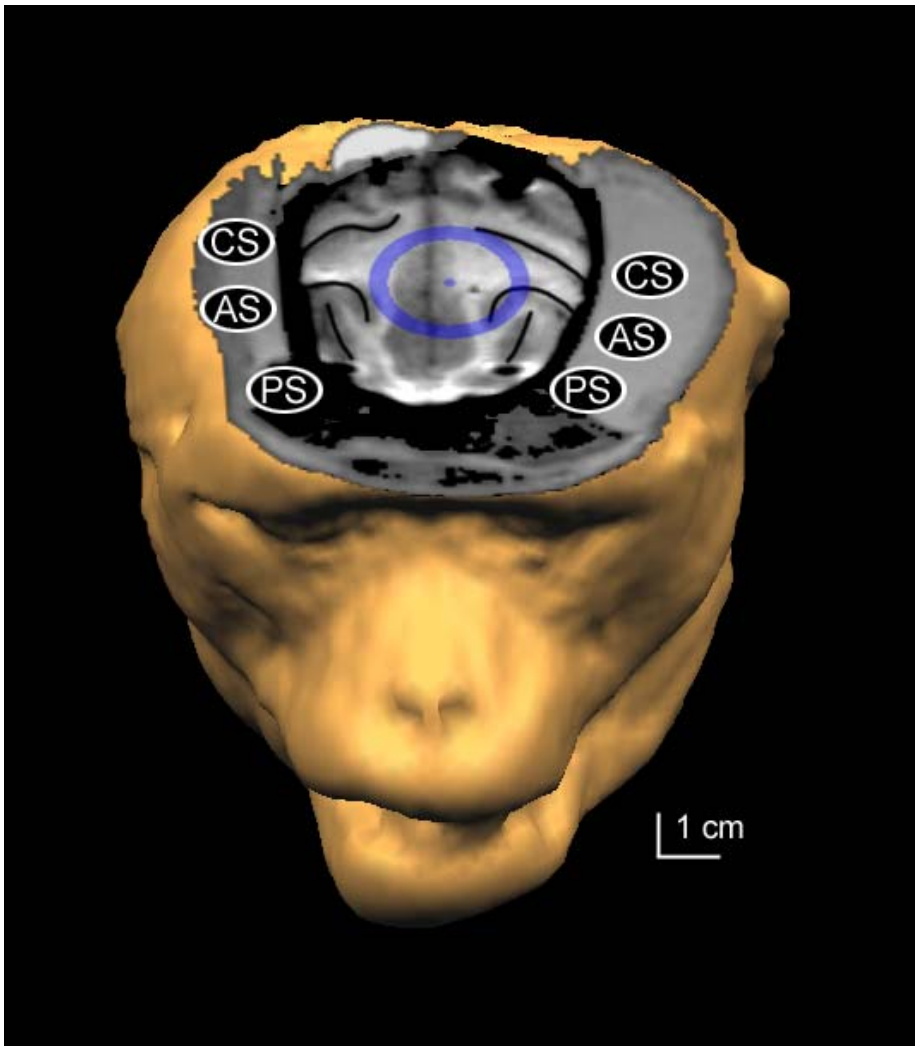

Figure IV.2.8

Three dimensional rendering of the whole head of monkey S with a plane cut level with Figure IV.2.6 and orthogonal to the recording chamber. Chamber wall is represented by the blue circle, with the central axis of the chamber shown by a blue point. Scale bars differ in horizontal and vertical dimensions as the image is a perspective view. Major sulci are identified: central sulcus (CS), arcuate sulcus (AS) and principal sulcus (PS.)

Figure IV.3.1

Fiducial markers visible with T1 weighted MRI image acquisition. Left: a commercially available “donut” marker consisting of a sealed plastic casing with adhesive backing containing a small amount of contrast media and a soft sponge. Right: a custom-made glass bead blown from a capillary and sealed, containing an aqueous solution of gadopentetate dimeglumine (~50 mg/mL).

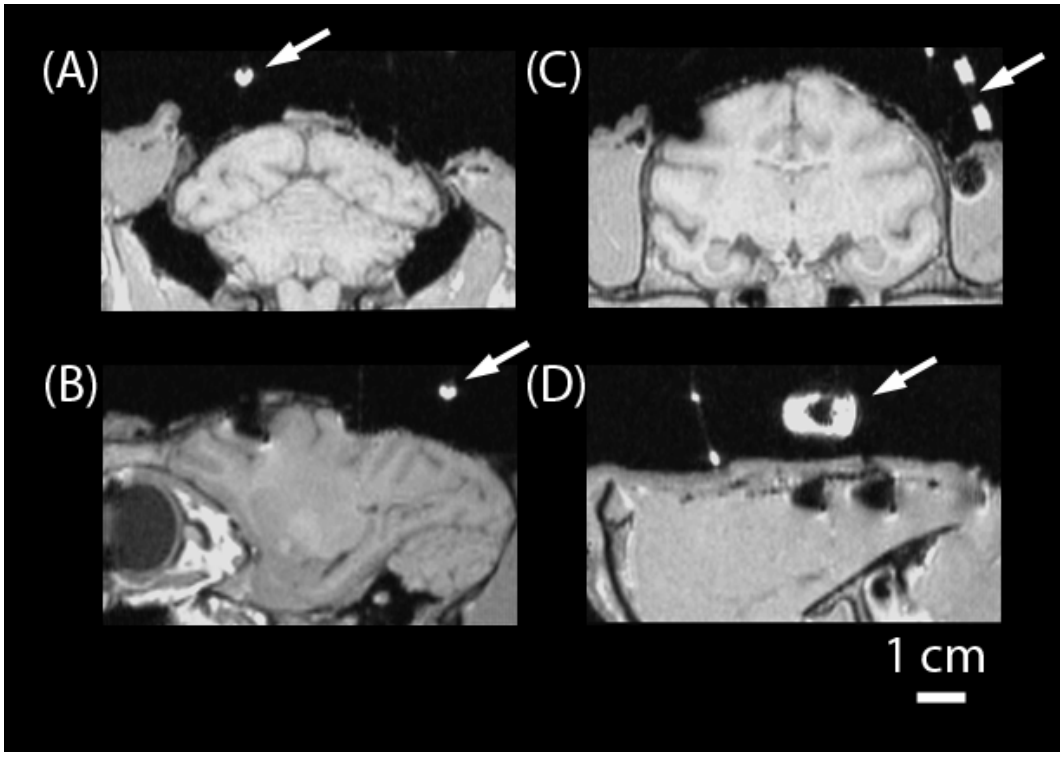

Figure IV.3.2

T1 weighted anatomical images acquired on a 1.5 T Siemens Magnetom Vision clinical MRI scanner. Arrows indicate a glass bead fiducial marker (A, B) implanted in the head cap material of the animals restraint, and a "donut" fiducial marker (C, D) adhered to the surface of the head cap. Images are of a stereotaxic orientation of a coronal (A, C) and sagittal (B, D) plane through the center point of each marker.

CHAPTER V: Summary and Future Directions

V.1 THE ROLE OF MRI IN THE NEUROSCIENCES

Magnetic resonance imaging (MRI) is a phenomenally useful tool for the neurosciences with wide application in a variety of fields. This document represents four years of investigation into the technology, application and development of MRI for functional and structural imaging. Furthermore, two separate species – human and macaque – were used as experimental subjects for imaging, each with their own special requirements and idiosyncrasies for investigative success.

V.1.1 Human Subjects

In the human population, a blood oxygen level dependent (BOLD) contrast functional imaging study was performed. The use of such a paradigm greatly enhances the ease with which subjects may be recruited as the entire procedure is completely noninvasive. However, ethical and safety concerns do play a prominent role in studies using human subjects. Proper institutional approval and assurance that the high magnetic field environment of the magnet is suitable for the volunteer are vital concerns. Developing such a study requires knowledge and application of these principles. Creating a task for evaluation in an imaging session requires adapting experimental design to the constrictive and limiting environment of a high field superconducting electromagnet. Limited space dictates what stimuli may be presented and where, while the strong magnetic field limits

the equipment which may be used. Training a human subject to perform an experimental task is usually straightforward, in sharp contrast to laboratory animals.

V.1.2 Macaque Subjects

When working with live animals, in this case the macaque monkey (*Macaca mulatta*), a different but equally important set of ethical and safety rules and procedures apply. Acquiring institutional approval to work with the animals and to use them in a particular experiment requires working closely with animal technicians and the veterinary staff to meet all the animal's health and welfare requirements. As an experimenter, the animal's handler becomes intimately involved in maintaining nearly all aspects of the macaque's daily routine. This requires knowledge of the animal's physiology and behavior, factors which may differ greatly between individual subjects. Furthermore, all the experimental development constraints for human studies apply, along with the added necessity of routinely training the animal. Depending on the difficulty of the task, this could require months to years of preparation time and continual maintenance of a training regimen. One of the greatest obstacles to working with live animals, this often requires vast expenditures of time and patience. However, this investment is not without reward. There are many avenues of research which can be explored in a macaque which would be difficult or prohibitive in human subjects. Prime examples are the use of various contrast materials and electrode recordings for functional studies, and the capacity to perform anesthetized studies on demand for precise anatomical imaging.

V.1.3 Functional Imaging

Functional MRI allows the investigation of cortical responses to various tasks and stimuli. Presently, the technique centers on the analysis of vascular changes by fast imaging of changing local magnetic fields in the blood vessels and surrounding tissue. Such an analysis may be conducted noninvasively by leveraging the variation of magnetic properties of a tissue and blood volume, based on relative volume of blood, vascular flow and oxygenation state of hemoglobin. Alternatively, an exogenous contrast media may be injected intravenously to replace the signal arising from blood and subsequently imaged in a similar fashion. Both methods of functional imaging are represented in this study.

V.1.4 Anatomical Imaging

There is no technique, save perhaps actual physical dissection, which gives a greater understanding of the physical morphology of the central nervous system than MRI. The unparalleled volume resolution of the images allow the submillimeter investigation of any intracortical region. Whether used for clinical surgical planning, the evaluation of evolutionary changes in anatomy or to aid the localization of a functional volume, MRI provides enormous benefits as an anatomical technique. Limited only by uncommon medical conditions which would affect the health of affected individuals, almost any organism with a brain may undergo anatomical analysis using MRI.

V.1.5 Investigation of the Motion Aftereffect

The visual motion aftereffect (MAE) is a compelling and readily demonstrable visual illusion that has profound implications concerning the cortical processing of visual motion. After well over a century of scientific investigation of the effect, still the precise mechanisms and involved brain areas are unknown (Mather et al., 1998). Some electrode recording data suggests that the adaptation of neurons to a particular direction of motion may affect the discharge rate of the cells to a subsequently presented stimulus (Petersen et al., 1985). Functional imaging has located and correlated the activation of motion-sensitive areas in the visual processing stream to the percept of illusory motion when a MAE paradigm is used (Tootell et al., 1995). This study contributes to this understanding by investigation of the relative response in two subregions of motion-sensitive cortex, pMT and pMST, and suggests that pMST contributes more to MAE functional activation than pMT.

V.1.6 Use of an Iron Oxide Contrast Agent

Contrast agents are widely used in anatomical imaging but may also be used to evaluate a functional response. This study adapts the conventional clinical iron oxide agent Feridex for use as an intravascular functional contrast and presents the first use of iron oxide functional imaging in the macaque. Use of Feridex in this fashion provided three times the contrast to noise ratio of conventional BOLD imaging at the cost of decreased temporal resolution. Feridex remains in the blood pool for an extended period of time, with a half life of 198 minutes, making it possible to prepare the animal for an imaging study hours before acquisition. Subsequent independent development of iron oxide agents has made

their use frequent in the imaging of the macaque to improve functional localization (Denys et al., 2004).

V.1.7 Guidance of Microwire Placement

The implantation of microwire electrodes for chronic neuronal recording has been used to record spiking and local field potential activity during repeated experimental sessions (Donoghue et al., 1998). A major pitfall in their use, singly or in array, is the need to accurately target the cortical structures of interest from which recordings will be made. This difficulty is exacerbated by the fixed placement of the electrodes – unlike acute recordings, the chronic electrodes are immobile after implantation. This study evaluates the use of MRI images to facilitate surgical implantation of microwire arrays in macaque posterior parietal cortex. Implantation of electrodes using this technique resulted in the successful placement of microwire arrays which demonstrated multichannel activity, the function of which suggested the cortical area of interest had been accurately targeted. This method could be developed for uses such as the control of a neural prosthetic (Isaacs et al., 2000a) by macaque or, ultimately, human subjects.

V.1.8 Determining Chamber Coordinates and Electrode Localization

After an animal has been used for multiple single electrode electrophysiology experiments, it is vital to know the cortical regions from whence the data originated. This localization is particularly important in the investigation of novel areas. A previous method has used tungsten wires implanted prior to imaging as a guide for the placement of recording

chambers (Asahi et al., 2003). This study eliminates the need for a separate surgical procedure and allows the visualization of electrode penetration locations in any animal with an existing chamber. Using anatomical MRI images of the experimental animals aligned orthogonal to the electrode penetration paths, this study provides methods for reconstructing the sites of recording and visualizing the data by 2D and 3D rendering. Application of this technique allows the anatomical verification of electrode placement while allowing the subject to remain in active experimental use.

V.1.9 Implantable Fiducial Markers

Finally, an advance in the hardware used in imaging was developed in the form of implantable glass beads filled with contrast media. Unlike commonly available fiducial markers for MRI, which are designed to be temporary and disposable, the implantable beads could be a permanent part of the experimental hardware used in the construction of a head cap for an animal subject. When placed in such a manner, the fiducials guarantee accuracy and the ability to coregister images acquired at different periods of the experimental life of the animal. Through such a method, growth related changes in the morphology of the animal's central nervous system could be monitored and the effects on electrode placement and the location of structures of interest could be evaluated.

V.1.10 Final Words

MRI has served as an excellent unifying theme for learning the principles of neuroscience. The high-resolution of the technique allows the user to develop a familiarity with the gross

anatomy and variations of cortical morphology between subjects. After years of such use, a sound understanding of the physiology of the brain is gained, serving as a welcome foundation for learning the intricacies of neural function. Similarly, functional imaging provides experience in viewing the activation and interconnection of multiple brain areas as they act in concert to respond to a stimulus. It is a broad perspective which is gained, sacrificing the intimate knowledge of individual neuronal responses for the ability to understand the wider responses of brain function. In closing, I am grateful for my experiences with MRI, and look forward to the challenges and rewards of its future development.

V.2 VERTICAL BORE SYSTEMS FOR MACAQUE fMRI

With the advent of vertical bore MRI scanners, it is now possible to situate a macaque within the imaging volume in a more natural position. When a conventional horizontal bore magnet is used, the animal must first be placed prone to accommodate the volume and axis of the bore. Further, to establish an optical path so that the monkey can view a presented stimulus, the head must be inclined such that the animal is viewing down the axis of the bore. This position is uncomfortable and unnatural, predisposing the animal to move and shift position during the experiment which can only lead to image degradation and loss of signal to noise. In contrast, a vertical bore magnet allows the animal to be seated in an upright position similar to commonly used primate chairs and closely approximating the natural posture adopted on an unconstrained perch. Beyond increasing the comfort of the position, it could be conceived that proper head to trunk positioning could be vital to some

visual planning experiments. Finally, allowing the animal to sit on its hind legs in a chair or perch within the vertical bore frees the forelimbs of the monkey for tasks such as reaching and arm positioning. Increased use of vertical bore magnet systems for macaque functional imaging will improve the ease with which studies are conducted and expand the range of possible experimental paradigms.

V.3 MERGING FUNCTIONAL AND ANATOMICAL IMAGING

In clinical and academic neuroscience, functional and anatomical imaging currently occupy two distinct and largely isolated roles. Functional imaging is used to identify areas in the brain responding to a given type of stimuli while anatomical imaging is used to locate areas of cortex based on physical structure. A new frontier presents itself in the combination of these techniques, which would impact the way in which stereotaxic surgery is performed. Currently, in stereotaxic surgery, as in the study presented above, high-resolution structural MRI images are used to guide the location of recording or stimulating electrodes or to plan surgical removal of pathologic tissue. While the anatomical localization needs of these procedures are well served, consider the further application of functional activation to the images available for surgical planning. In the laboratory, this might take the form of guiding electrodes now not to a purely anatomical site, but to a location verified to have relevant activation in the subject by a functional scan. Clinically, surgical planning might take advantage of functional mapping to avoid or otherwise preserve areas of cortex with a vital function, such as speech or motor planning. The tools and techniques for making both aspects of imaging useful have been developed largely independently. In the immediate

future, it is both likely and beneficial that hybridization of functional and structural imaging will occur.

REFERENCES

Addams R (1834) An account of a peculiar optical phenomenon seen after having looked at a moving body. London and Edinburgh Phiolosophical Magazine and Journal of Science 5:373-374.

Ahrens ET, Dubowitz DJ (2001) Peripheral somatosensory fMRI in mouse at 11.7 T. NMR Biomed 14:318-324.

Allman JM (1999) Evolving brains. New York: Scientific American Library : Distributed by W.H. Freeman.

Andersen RA, Snyder LH, Bradley DC, Xing J (1997) Multimodal representation of space in the posterior parietal cortex and its use in planning movements. Annu Rev Neurosci 20:303-330.

Andersen RA, Shenoy KV, Crowell JA, Bradley DC (2000) Neural mechanisms for self-motion perception in area MST. Int Rev Neurobiol 44:219-233.

Andersen RA, Snyder LH, Batista AP, Buneo CA, Cohen YE (1998) Posterior parietal areas specialized for eye movements (LIP) and reach (PRR) using a common coordinate frame. In: Novartis Foundation Symposium 218: Sensory Guidance of Movement. (Goode JA, ed), pp 109-128. Chichester: Wiley.

Asahi T, Tamura R, Eifuku S, Hayashi N, Endo S, Nishijo H, Ono T (2003) A method for accurate determination of stereotaxic coordinates in single unit recording studies in monkeys by high-resolution three-dimensional magnetic resonance imaging. Neurosci Res 47:255-260.

Attwell D, Iadecola C (2002) The neural basis of functional brain imaging signals. Trends Neurosci 25:621-625.

Baker SN, Philbin N, Spinks R, Pinches EM, Wolpert DM, MacManus DG, Pauluis Q, Lemon RN (1999) Multiple single unit recording in the cortex of monkeys using independently moveable microelectrodes. J Neurosci Methods 94:5-17.

Barlow HB, Hill RM (1963) Evidence for a Physiological Explanation of the Waterfall Phenomenon and Figural after-Effects. Nature 200:1345-1347.

Becker TA, Kipke DR, Brandon T (2001) Calcium alginate gel: a biocompatible and mechanically stable polymer for endovascular embolization. J Biomed Mater Res 54:76-86.

Belliveau JW, Kennedy DN, Jr., McKinstry RC, Buchbinder BR, Weisskoff RM, Cohen MS, Vevea JM, Brady TJ, Rosen BR (1991) Functional mapping of the human visual cortex by magnetic resonance imaging. Science 254:716-719.

Bernheim RA, Brown TH, Gutowsky HS, Woessner DE (1959) Temperature dependence of proton relaxation times in aqueous solutions of paramagnetic ions. Journal of Chemical Physics 30:950-956.

Blaizot X, Meguro K, Le Mestric C, Constans JM, Luet D, Baron JC, Chavoix C (1999) Combined use of T1-weighted MRI and MRA for stereotaxic lesioning of the nonhuman primate brain: application to the rhinal cortex. Exp Brain Res 126:31-40.

Bloch F (1946) Nuclear Induction. Phys Rev 70:460-474.

Bloembergen N, Purcell, E. M., and Pound, R. V. (1948) Relaxation Effects in NuclearMagnetic Resonance Absorption. Phys Rev 73:679-712.

Brewer AA, Press WA, Logothetis NK, Wandell BA (2002) Visual areas in macaque cortex measured using functional magnetic resonance imaging. J Neurosci 22:10416-10426.

Buneo CA, Jarvis MR, Batista AP, Andersen RA (2002) Direct visuomotor transformations for reaching. Nature 416:632-636.

Butler T, Brown B, Dysko R, Ford E, Hoskins D, Klein H, Levin J, Murray K, Rosenberg D, Southers J, Swensen R (1995) Medical Management. In: Nonhuman Primates in Biomedical Research: Biology and Management (Bennett C, Abee R, eds), pp 257-334. London: Academic Press.

Chapin JK, Moxon KA, Markowitz RS, Nicolelis ML (1999) Real-time control of a robot arm using simultaneously recorded neurons in the motor cortex. Nature Neuroscience 2:664-670.

Coleman T, Li Y (1996) An interior trust region approach for nonlinear minimization subject to bounds. SIAM J Optim 6:418-445.

Cox RW (1996a) AFNI: software for analysis and visualization of functional magnetic resonance neuroimages. Comput Biomed Res 29:162-173.

Cox RW (1996b) AFNI: Software for analysis and visualization of functional magnetic resonance neuroimages. Computers and Biomedical Research 29:162-173.

Cox RW, Hyde JS (1997) Software tools for analysis and visualization of fMRI data. NMR Biomed 10:171-178.

Cox RW, Jesmanowicz A (1999) Real-time 3D image registration for functional MRI. Magn Reson Med 42:1014-1018.

Culham JC, Verstraten FA, Ashida H, Cavanagh P (2000) Independent aftereffects of attention and motion. Neuron 28:607-615.

Culham JC, Dukelow SP, Vilis T, Hassard FA, Gati JS, Menon RS, Goodale MA (1999) Recovery of fMRI activation in motion area MT following storage of the motion aftereffect. J Neurophysiol 81:388-393.

Dale AM (1999) Optimal experimental design for event-related fMRI. Hum Brain Mapp 8:109-114.

Deadwyler SA, Bunn T, Hampson RE (1996) Hippocampal ensemble activity during spatial delayed-nonmatch-to-sample performance in rats. J Neurosci 16:354-372.

Denys K, Vanduffel W, Fize D, Nelissen K, Peuskens H, Van Essen D, Orban GA (2004) The processing of visual shape in the cerebral cortex of human and nonhuman primates: a functional magnetic resonance imaging study. J Neurosci 24:2551-2565.

Desimone R, Ungerleider LG (1986) Multiple visual areas in the caudal superior temporal sulcus of the macaque. J Comp Neurol 248:164-189.

Donoghue JP, Sanes JN, Hatsopoulos NG, Gaal G (1998) Neural discharge and local field potential oscillations in primate motor cortex during voluntary movements. J Neurophysiol 79:159-173.

Dubowitz DJ (2002a) Functional Magnetic Resonance Imaging in Rhesus Macaque Monkeys. In: Computation and Neural Systems. Pasadena, CA: California Institute of Technology.

Dubowitz DJ (2002b) Functional Magnetic Resonance Imaging in Rhesus Macaque Monkeys. In: Ph.D. thesis in Computation and Neural Systems. Pasadena: California Institute of Technology.

Dubowitz DJ, Martinez A, McDowell J (1999) A simple set-up for tracking eye position during fMRI. In: 7th International Society of Magnetic Resonance in Medicine. Philadelphia, PA, USA.

Dubowitz DJ, Bernheim KA, Chen DY, Bradley Jr WG, Andersen RA (2001a) Enhancing fMRI contrast in awake-behaving primates using intravascular magnetite dextran nanopartieles. Neuroreport 12:2335-2340.

Dubowitz DJ, Chen DY, Atkinson DJ, Grieve KL, Gillikin B, Bradley WG, Jr., Andersen RA (1998) Functional magnetic resonance imaging in macaque cortex. Neuroreport 9:2213-2218.

Dubowitz DJ, Chen DY, Atkinson DJ, Scadeng M, Martinez A, Andersen MB, Andersen RA, Bradley WJ (2001b) Direct comparison of visual cortex activation in human and non-human primates using functional magnetic resonance imaging. J Neurosci Methods 107:71-80.

Dukelow SP, DeSouza JF, Culham JC, van den Berg AV, Menon RS, Vilis T (2001) Distinguishing subregions of the human MT+ complex using visual fields and pursuit eye movements. J Neurophysiol 86:1991-2000.

Fee MS, Leonardo A (2001) Miniature motorized microdrive and commutator system for chronic neural recording in small animals. J Neurosci Methods 112:83-94.

Fryer TB, Sandler H (1974) A review of implant telemetry systems. Biotelemetry 1:351-374.

Gati JS, Menon RS, Ugurbil K, Rutt BK (1997) Experimental determination of the BOLD field strength dependence in vessels and tissue. Magn Reson Med 38:296-302.

Gray CM, Konig P, Engel AK, Singer W (1989) Oscillatory responses in cat visual cortex exhibit inter-columnar synchronization which reflects global stimulus properties. Nature 338:334-337.

Gries H, Miklautz H (1984) Some physicochemical properties of the gadolinium-DTPA complex, a contrast agent for MRI. Physiol Chem Phys Med NMR 16:105-112.

Hamel W, Schrader B, Weinert D, Herzog J, Volkmann J, Deuschl G, Muller D, Mehdorn HM (2002) MRI- and skull x-ray-based approaches to evaluate the position of deep brain stimulation electrode contacts--a technical note. Zentralbl Neurochir 63:65-69.

Hatsopoulos NG, Ojakangas CL, Paninski L, Donoghue JP (1998) Information about movement direction obtained from synchronous activity of motor cortical neurons. Proc Natl Acad Sci U S A 95:15706-15711.

He S, Cohen ER, Hu X (1998) Close correlation between activity in brain area MT/V5 and the perception of a visual motion aftereffect. Curr Biol 8:1215-1218.

Huk AC, Ress D, Heeger DJ (2001) Neuronal basis of the motion aftereffect reconsidered. Neuron 32:161-172.

Humphrey DR, Schmidt EM, Thompson WD (1970) Predicting measures of motor performance from multiple cortical spike trains. Science 170:758-762.

Isaacs RE, Weber DJ, Schwartz AB (2000a) Work toward real-time control of a cortical neural prothesis. IEEE Trans Rehabil Eng 8:196-198.

Isaacs RE, Weber DJ, Schwartz AB (2000b) Work toward real-time control of a cortical neural prothesis. IEEE Trans Rehabil Eng 8:196-198.

Kalaska JF (1996) Parietal cortex area 5 and visuomotor behavior. Can J Physiol Pharmacol 74:483-498.

Kennan RP, Scanley BE, Innis RB, Gore JC (1998) Physiological basis for BOLD MR signal changes due to neuronal stimulation: separation of blood volume and magnetic susceptibility effects. Magn Reson Med 40:840-846.

Koyama M, Hasegawa I, Osada T, Adachi Y, Nakahara K, Miyashita Y (2004) Functional magnetic resonance imaging of macaque monkeys performing visually guided saccade tasks: comparison of cortical eye fields with humans. Neuron 41:795-807.

Kralik JD, Dimitrov DF, Krupa DJ, Katz DB, Cohen D, Nicolelis MA (2001) Techniques for long-term multisite neuronal ensemble recordings in behaving animals. Methods 25:121-150.

Kruger J, Bach M (1981) Simultaneous recording with 30 microelectrodes in monkey visual cortex. Exp Brain Res 41:191-194.

Kwong KK, Belliveau JW, Chesler DA, Goldberg IE, Weisskoff RM, Poncelet BP, Kennedy DN, Hoppel BE, Cohen MS, Turner R, et al. (1992) Dynamic magnetic resonance imaging of human brain activity during primary sensory stimulation. Proc Natl Acad Sci U S A 89:5675-5679.

Lambert JB, Mazzola EP (2004) Nuclear magnetic resonance spectroscopy : an introduction to principles, applications, and experimental methods. Upper Saddle River, N.J.: Pearson Education.

Lauterbur PC (1986) NMR imaging in biomedicine. Cell Biophys 9:211-214.

Leniger-Follert E, Lubbers DW (1976) Behavior of microflow and local PO2 of the brain cortex during and after direct electrical stimulation. A contribution to the problem of metabolic regulation of microcirculation in the brain. Pflugers Arch 366:39-44.

Logothetis NK (2002) The neural basis of the blood-oxygen-level-dependent functional magnetic resonance imaging signal. Philos Trans R Soc Lond B Biol Sci 357:1003-1037.

Logothetis NK (2003) The underpinnings of the BOLD functional magnetic resonance imaging signal. J Neurosci 23:3963-3971.

Logothetis NK, Wandell BA (2004) Interpreting the BOLD Signal. Annu Rev Physiol 66:735-769.

Logothetis NK, Guggenberger H, Peled S, Pauls J (1999a) Functional imaging of the monkey brain. Nat Neurosci 2:555-562.

Logothetis NK, Guggenberger H, Peled S, Pauls J (1999b) Functional imaging of the monkey brain. Nat Neurosci 2:555-562.

Lotze M, Laubis-Herrmann U, Topka H, Grodd W (1999) Reorganization in the primary motor cortex after spinal cord injury - a functional magnetic resonance (fMRI) study. Restorative Neurology and Neuroscience 14:183-187.

Maffei L, Fiorentini A, Bisti S (1973) Neural correlate of perceptual adaptation to gratings. Science 182:1036-1038.

Mandeville JB, Moore J, Chesler DA, Garrido L, Weissleder R, Weisskoff RM (1997) Dynamic liver imaging with iron oxide agents: effects of size and biodistribution on contrast. Magn Reson Med 37:885-890.

Mandeville JB, Marota JJ, Kosofsky BE, Keltner JR, Weissleder R, Rosen BR, Weisskoff RM (1998) Dynamic functional imaging of relative cerebral blood volume during rat forepaw stimulation. Magn Reson Med 39:615-624.

Mansfield P, Maudsley AA (1977) Medical imaging by NMR. Br J Radiol 50:188-194.

Mather G, Verstraten F, Anstis SM (1998) The motion aftereffect : a modern perspective. Cambridge, Mass: The MIT Press.

Meeker D, Cao S, Burdick JW, Andersen RA (2002) Rapid plasticity in the parietal reach region demonstrated with a brain - computer interface. Society of Neuroscience Abstracts 28: 357.7.

Merzenich MM, Nelson RJ, Stryker MP, Cynader MS, Schoppmann A, Zook JM (1984) Somatosensory cortical map changes following digit amputation in adult monkeys. J Comp Neurol 224:591-605.

Nicolelis MA, Ghazanfar AA, Faggin BM, Votaw S, Oliveira LM (1997) Reconstructing the engram: simultaneous, multisite, many single neuron recordings. Neuron 18:529-537.

Nicolelis MAL, Stambaugh CR, Brisben A, Laubach M (1999) Methods for simultaneous multisite ensemble recordings in behaving primates. In: Methods for Neural

Ensemble Recordings (Nicolelis MAL, ed), pp 121-156. Boca Raton, London, New York: CRC Press.

Ogawa S, Lee TM, Kay AR, Tank DW (1990) Brain magnetic resonance imaging with contrast dependent on blood oxygenation. Proc Natl Acad Sci U S A 87:9868-9872.

O'Keefe J, Bouma H (1969) Complex sensory properties of certain amygdala units in the freely moving cat. Experimental Neurology 23:384.

Paradiso MA (1999) Monkey business builds a bridge to the human brain. Nat Neurosci 2:491-492.

Percival DB, Walden AT (1993) Spectral analysis for physical applications - multitaper and conventional univariate techniques. Cambridge, MA: Cambridge University Press.

Pesaran B, Pezaris JS, Sahani M, Mitra PP, Andersen RA (2002) Temporal structure in neuronal activity during working memory in macaque parietal cortex. Nat Neurosci 5:805-811.

Petersen SE, Baker JF, Allman JM (1985) Direction-specific adaptation in area MT of the owl monkey. Brain Res 346:146-150.

Pezaris JS, Dubowitz DJ (1999a) MRI Localization of Extracellular Electrodes Using Metallic Deposition at 1.5T. In: 7th International Society of Magnetic Resonance in Medicine. Philadelpha, PA, USA.

Pezaris JS, Dubowitz DJ (1999b) MRI Localization of Extracellular Electrodes Using Metallic Deposition at 1.5T. In: Proc of Int Soc Magn Res Med, p 968.

Price RE, Leeds NE, Hazle JD, Jackson EF, Stephens LC, Ang KK (1997) Magnetic resonance imaging of the central nervous system of the rhesus monkey. Lab Anim Sci 47:304-312.

Raiguel S, Van Hulle MM, Xiao DK, Marcar VL, Lagae L, Orban GA (1997) Size and shape of receptive fields in the medial superior temporal area (MST) of the macaque. Neuroreport 8:2803-2808.

Rees G, Friston K, Koch C (2000) A direct quantitative relationship between the functional properties of human and macaque V5. Nat Neurosci 3:716-723.

Saunders RC, Aigner TG, Frank JA (1990) Magnetic resonance imaging of the rhesus monkey brain: use for stereotactic neurosurgery. Exp Brain Res 81:443-446.

Scheffler K, Seifritz E, Haselhorst R, Bilecen D (1999) Titration of the BOLD effect: separation and quantitation of blood volume and oxygenation changes in the human cerebral cortex during neuronal activation and ferumoxide infusion. Magn Reson Med 42:829-836.

Scherberger H, Andersen RA (2003) Senosorimotor transformations. In: The Visual Neurosciences (Werner JS, ed), pp 1324-1336. Cambridge, MA: MIT Press.

Scherberger H, Jarvis M, Andersen RA (2001) Properties of the local field potential in the macaque posterior parietal cortex during arm-reaching movements. In: 11th annual meeting of the Society for the Neural Control of Movement. (http://www-ncm.cs.umass.edu).

Scherberger H, Fineman I, Musallam S, Dubowitz DJ, Bernheim KA, Pesaran B, Corneil BD, Gilliken B, Andersen RA (2003) Magnetic resonance image-guided

implantation of chronic recording electrodes in the macaque intraparietal sulcus. J Neurosci Methods 130:1-8.

Schmidt EM (1999) Electrodes for many single neuron recordings. In: Methods for Neural Ensemble Recordings (Nicolelis MAL, ed), pp 1-23. Boca Raton, London, New York: CRC Press.

Seiffert AE, Somers DC, Dale AM, Tootell RB (2003) Functional MRI studies of human visual motion perception: texture, luminance, attention and after-effects. Cereb Cortex 13:340-349.

Seifritz E, Bilecen D, Hanggi D, Haselhorst R, Radu EW, Wetzel S, Seelig J, Scheffler K (2000) Effect of ethanol on BOLD response to acoustic stimulation: implications for neuropharmacological fMRI. Psychiatry Res 99:1-13.

Serruya MD, Hatsopoulos NG, Paninski L, Fellows MR, Donoghue JP (2002) Brain-machine interface: Instant neural control of a movement signal. Nature 416:141-142.

Shen T, Weissleder R, Papisov M, Bogdanov A, Jr., Brady TJ (1993) Monocrystalline iron oxide nanocompounds (MION): physicochemical properties. Magn Reson Med 29:599-604.

Shenoy KV, Meeker D, Cao S, Kureshi SA, Pesaran B, Buneo CA, Batista AP, Mitra PP, Burdick JW, Andersen RA (2003) Neural prosthetic control signals from plan activity. Neuroreport 14:591-596.

Silva AC, Lee SP, Iadecola C, Kim SG (2000) Early temporal characteristics of cerebral blood flow and deoxyhemoglobin changes during somatosensory stimulation. J Cereb Blood Flow Metab 20:201-206.

Snyder LH, Batista AP, Andersen RA (1997) Coding of intention in the posterior parietal cortex. Nature 386:167-170.

Snyder LH, Batista AP, Andersen RA (1998) Change in motor plan, without a change in the spatial locus of attention, modulates activity in posterior parietal cortex. J Neurophysiol 79:2814-2819.

Stefanacci L, Reber P, Costanza J, Wong E, Buxton R, Zola S, Squire L, Albright T (1998) fMRI of monkey visual cortex. Neuron 20:1051-1057.

Strumwasser F (1958) Long-term recording from single neurons in brain of unrestrained mammals. Science 127:469.

Takechi H, Onoe H, Imamura K, Onoe K, Kakiuchi T, Nishiyama S, Yoshikawa E, Mori S, Kosugi T, Okada H, et al. (1994) Brain activation study by use of positron emission tomography in unanesthetized monkeys. Neurosci Lett 182:279-282.

Tanaka K, Sugita Y, Moriya M, Saito H (1993) Analysis of object motion in the ventral part of the medial superior temporal area of the macaque visual cortex. J Neurophysiol 69:128-142.

Tanaka K, Hikosaka K, Saito H, Yukie M, Fukada Y, Iwai E (1986) Analysis of local and wide-field movements in the superior temporal visual areas of the macaque monkey. J Neurosci 6:134-144.

Taylor DM, Tillery SI, Schwartz AB (2002) Direct cortical control of 3D neuroprosthetic devices. Science 296:1829-1832.

Thompson P, Wright J (1994) The role of intervening patterns in the storage of the movement aftereffect. Perception 23:1233-1240.

Tootell RB, Nelissen K, Vanduffel W, Orban GA (2004) Search for Color 'Center(s)' in Macaque Visual Cortex. Cereb Cortex 14:353-363.

Tootell RB, Reppas JB, Dale AM, Look RB, Sereno MI, Malach R, Brady TJ, Rosen BR (1995) Visual motion aftereffect in human cortical area MT revealed by functional magnetic resonance imaging. Nature 375:139-141.

Tsao DY, Freiwald WA, Knutsen TA, Mandeville JB, Tootell RB (2003) Faces and objects in macaque cerebral cortex. Nat Neurosci 6:989-995.

Turner R, Jezzard P, Wen H, Kwong KK, Le Bihan D, Zeffiro T, Balaban RS (1993) Functional mapping of the human visual cortex at 4 and 1.5 tesla using deoxygenation contrast EPI. Magn Reson Med 29:277-279.

Van Wezel RJ, Britten KH (2002) Motion adaptation in area MT. J Neurophysiol 88:3469-3476.

Vanduffel W, Fize D, Peuskens H, Denys K, Sunaert S, Todd JT, Orban GA (2002) Extracting 3D from motion: differences in human and monkey intraparietal cortex. Science 298:413-415.

Vanduffel W, Fize D, Mandeville JB, Nelissen K, Van Hecke P, Rosen BR, Tootell RB, Orban GA (2001) Visual motion processing investigated using contrast agent-enhanced fMRI in awake behaving monkeys. Neuron 32:565-577.

Vautin RG, Berkley MA (1977) Responses of single cells in cat visual cortex to prolonged stimulus movement: neural correlates of visual aftereffects. J Neurophysiol 40:1051-1065.

Verstraten FA, Fredericksen RE, Grusser OJ, van de Grind WA (1994) Recovery from motion adaptation is delayed by successively presented orthogonal motion. Vision Res 34:1149-1155.

Villringer A, Rosen BR, Belliveau JW, Ackerman JL, Lauffer RB, Buxton RB, Chao YS, Wedeen VJ, Brady TJ (1988) Dynamic imaging with lanthanide chelates in normal brain: contrast due to magnetic susceptibility effects. Magn Reson Med 6:164-174.

Wessberg J, Stambaugh CR, Kralik JD, Beck PD, Laubach M, Chapin JK, Kim J, Biggs J, Srinivasan MA, Nicolelis MAL (2000) Real-time prediction of hand trajectory by ensembles of cortical neurons in primates. Nature 408:361-365.

Westergaard GC, Champoux M, Suomi SJ (1997) Hand preference in infant rhesus macaques (Macaca mulatta). Child Dev 68:387-393.

White DL, Aicher KP, Tzika AA, Kucharczyk J, Engelstad BL, Moseley ME (1992) Iron-dextran as a magnetic susceptibility contrast agent: flow-related contrast effects in the T2-weighted spin-echo MRI of normal rat and cat brain. Magn Reson Med 24:14-28.

Wohlgemuth A (1911) On the after-effect of seen movement. British Journal of Psycology (Supp) 1:1-117.

Wu CW-H, Kaas JH (1999) Reorganization in primary motor cortex of primates with long-standing therapeutic amputations. Journal of Neuroscience 19:7679-7697.

Zhang Z, Andersen AH, Avison MJ, Gerhardt GA, Gash DM (2000) Functional MRI of apomorphine activation of the basal ganglia in awake rhesus monkeys. Brain Res 852:290-296.

APPENDIX A: Stimulus Generation

A.1 STIM.C

A.1.1 Description

This stimulus application is written in ANSI C using common OpenGL routines for graphical rendering. It provides for the display of a central fixation target with eight surrounding radial targets, each of which can be displayed in a variety of colors and for varying lengths of time. Support is included for altering the position of the stimulus dynamically during runtime, and for varying the distance between fixation and target and the sizes of the independent cues. Every effort has been made to ensure portability of the code between the Linux operating system and the Cygwin compiler to facilitate using the application under Microsoft Windows.

A.1.2 Use

After invoking the application from the command line, use the “f” and “w” keys to toggle full screen mode, and the “t” key to bring up a test image of all cues. The position of the stimulus may be changed by clicking and dragging with the left mouse button. Recenter the stimulus by pressing the “z” key. The absolute size of the stimulus may be changed by clicking and dragging with the right mouse button. To change the distance between targets and fixation, use the “+” and “-” keys. To change the size of the fixation cue independent of the target cues, use the “,” and “.” keys. A trial may be restarted at any time by pressing the “0” (zero) key. Pressing ESC terminates execution.

A.1.3 Code

```
/*
 *    Copyright 2004 Kyle A. Bernheim, California Institute of Technology
 */

#include <windows.h>
#include <GL/glut.h>
#include <stdio.h>
#include <stdlib.h>
#include <time.h>

#define SEED 12312

#define STIM_FIXDOT 0
#define STIM_REACH 1
#define STIM_LOOK 2
#define STIM_BLACK 3

#define EPOCH_LENGTH    40.0
#define PULSES_PER_EPOCH 40.0
#define PULSE_LENGTH     ( EPOCH_LENGTH / PULSES_PER_EPOCH )

#define PERCENT_TIME_TILL_FLASH    ( 1.0 / 4.0 )
#define PERCENT_TIME_IN_FLASH    ( 1.0 / 4.0 )
#define PERCENT_TIME_AFTER_FLASH( 2.0 / 4.0 )

#define TIME_TILL_FLASH     ( PERCENT_TIME_TILL_FLASH * PULSE_LENGTH )
#define FLASH_LENGTH    ( PERCENT_TIME_IN_FLASH * PULSE_LENGTH )
#define MEMORY_LENGTH    ( PERCENT_TIME_AFTER_FLASH * PULSE_LENGTH )

#define INITIAL_DOT_SIZE  20.0

#define POSITIVE_PERCENTAGE 0.9

double HZ;
LARGE_INTEGER clockcounter;
LARGE_INTEGER statestart;
LARGE_INTEGER statestartn;
int pos;
int stimulusstate;
int stateiteration;
int fixflash;
float doweflash;
float xorigin;
float yorigin;
int moving;
int xmouse;
int ymouse;
float xoriginold;
float yoriginold;
float zoomlevel;
```

```
float zoomlevelold;
float dotdistance;
float fixdotsize;
int fixdoton;
int targeton;
int testpattern;

void calibrateclock()
{
  LARGE_INTEGER freq;

  printf( "Calibrating chip speed, please wait...\n\r" );

  QueryPerformanceFrequency(&freq);

  HZ = (double)freq.QuadPart;

/* For variable clock rate processors */
//HZ = 700 * 1e6;

  printf( "%u\n\r", HZ );
}

void init( void )
{
  glClearColor( 0.0, 0.0, 0.0, 0.0 );
}

void draw_fixdot( void )
{
  GLUquadricObj* q;

  glPushMatrix();
  q = gluNewQuadric();
  gluDisk( q, 0, INITIAL_DOT_SIZE + fixdotsize + zoomlevel, 100, 1 );
  glPopMatrix();
}

void draw_dot( void )
{
  GLUquadricObj* q;

  glPushMatrix();
  glColor4f( 1.0, 1.0, 0.0, 1.0 );
  q = gluNewQuadric();
  gluDisk( q, 0, INITIAL_DOT_SIZE + zoomlevel, 100, 1 );
  glPopMatrix();
}

void display( void )
{
  glClear( GL_COLOR_BUFFER_BIT );
```

```
if( stimulusstate == STIM_BLACK )
{
  glutSwapBuffers();
  return;
}

glPushMatrix();
glTranslatef( (float)xorigin, (float)yorigin, -10.0 );
glColor4f( 1.0, 0.0, 0.0, 1.0 );

if( stimulusstate == STIM_REACH && doweflash < POSITIVE_PERCENTAGE )
{
  glColor4f( 1.0, 0.0, 0.0, 1.0 );
}
else if( stimulusstate == STIM_LOOK && doweflash < POSITIVE_PERCENTAGE )
{
  glColor4f( 0.0, 0.0, 1.0, 1.0 );
}
else if( stimulusstate == STIM_REACH )
{
  glColor4f( 0.0, 0.0, 1.0, 1.0 );
}
else if( stimulusstate == STIM_LOOK )
{
  glColor4f( 1.0, 0.0, 0.0, 1.0 );
}

if( testpattern || fixdoton || stimulusstate == STIM_FIXDOT )
{
  draw_fixdot();
}

if( testpattern )
{
  glTranslatef( 0.0, 5.0 * ( INITIAL_DOT_SIZE + zoomlevel) + dotdistance, 0.0 );
  draw_dot();
  glTranslatef( 0.0, -2.0 * ( 5.0 * ( INITIAL_DOT_SIZE + zoomlevel) + dotdistance), 0.0 );
  draw_dot();
  glTranslatef( 0.0, 5.0 * ( INITIAL_DOT_SIZE + zoomlevel) + dotdistance, 0.0 );
  glRotatef( 45.0, 0.0, 0.0, 1.0 );
  glTranslatef( 0.0, 5.0 * ( INITIAL_DOT_SIZE + zoomlevel) + dotdistance, 0.0 );
  draw_dot();
  glTranslatef( 0.0, -2.0 * ( 5.0 * ( INITIAL_DOT_SIZE + zoomlevel) + dotdistance), 0.0 );
  draw_dot();
  glTranslatef( 0.0, 5.0 * ( INITIAL_DOT_SIZE + zoomlevel) + dotdistance, 0.0 );
  glRotatef( 45.0, 0.0, 0.0, 1.0 );
  glTranslatef( 0.0, 5.0 * ( INITIAL_DOT_SIZE + zoomlevel) + dotdistance, 0.0 );
  draw_dot();
  glTranslatef( 0.0, -2.0 * ( 5.0 * ( INITIAL_DOT_SIZE + zoomlevel) + dotdistance), 0.0 );
  draw_dot();
  glTranslatef( 0.0, 5.0 * ( INITIAL_DOT_SIZE + zoomlevel) + dotdistance, 0.0 );
  glRotatef( 45.0, 0.0, 0.0, 1.0 );
  glTranslatef( 0.0, 5.0 * ( INITIAL_DOT_SIZE + zoomlevel) + dotdistance, 0.0 );
```

```
  draw_dot();
  glTranslatef( 0.0, -2.0 * ( 5.0 * ( INITIAL_DOT_SIZE + zoomlevel) + dotdistance), 0.0 );
  draw_dot();
}
else
{
  switch( pos )
  {
    case 0: default:
      glRotatef( -45.0, 0.0, 0.0, 1.0 );
      break;
    case 1:
      glRotatef( 0.0, 0.0, 0.0, 1.0 );
      break;
    case 2:
      glRotatef( 45.0, 0.0, 0.0, 1.0 );
      break;
    case 3:
      glRotatef( 90.0, 0.0, 0.0, 1.0 );
      break;
    case 4:
      glRotatef( 135.0, 0.0, 0.0, 1.0 );
      break;
    case 5:
      glRotatef( 180.0, 0.0, 0.0, 1.0 );
      break;
    case 6:
      glRotatef( 225.0, 0.0, 0.0, 1.0 );
      break;
    case 7:
      glRotatef( 270.0, 0.0, 0.0, 1.0 );
      break;
  }

  glTranslatef( 0.0, 5.0 * ( INITIAL_DOT_SIZE + zoomlevel) + dotdistance, 0.0 );

  if( targeton )
  {
    switch( stimulusstate )
    {
      case STIM_FIXDOT: default:
        break;
      case STIM_REACH:
        draw_dot();
        break;
      case STIM_LOOK:
        draw_dot();
        break;
    }
  }
}

glPopMatrix();
```

```
  glutSwapBuffers();
}

void reshape( int w, int h )
{
  glViewport( 0, 0, w, h );
  glMatrixMode( GL_PROJECTION );
  glLoadIdentity();
  if( w == 0 )
  {
    glOrtho(-125.0f, 125.0f, -125.0f, 125.0f, 100.0, -100.0);
  }
  else
  {
    glOrtho(-0.5f * w, 0.5f * w, -0.5f * h, 0.5f * h, 100.0, -100.0);
  }
  glMatrixMode( GL_MODELVIEW );
  glLoadIdentity();
}

void mouse( int button, int state, int x, int y )
{
  if ( button == GLUT_LEFT_BUTTON && state == GLUT_DOWN )
  {
    xmouse = x;
    ymouse = y;
    moving = 1;
  }

  if ( button == GLUT_LEFT_BUTTON && state == GLUT_UP )
  {
    xoriginold = xorigin;
    yoriginold = yorigin;
    moving = 0;
  }

  if ( button == GLUT_RIGHT_BUTTON && state == GLUT_DOWN )
  {
    xmouse = x;
    ymouse = y;
    moving = 2;
  }

  if ( button == GLUT_RIGHT_BUTTON && state == GLUT_UP )
  {
    zoomlevelold = zoomlevel;
    moving = 0;
  }
}

void motion( int x, int y )
{
  if( moving == 1 )
```

```
  {
    xorigin = xoriginold + (float)((x - xmouse));
    yorigin = yoriginold + (float)((-1) * (y - ymouse));
    glutPostRedisplay();
  }

  if( moving == 2 )
  {
    zoomlevel = zoomlevelold + (float)((-1.0) * (y - ymouse)) * 0.02;
    glutPostRedisplay();
  }
}

void idle_func( void )
{
  LARGE_INTEGER currenttick, timesince;
  double timesinced;

  QueryPerformanceCounter(&statestartn);

  timesince.QuadPart = statestartn.QuadPart - clockcounter.QuadPart;

  timesinced = (double)timesince.QuadPart;

  if( timesinced / 10 < HZ )
  {
    stimulusstate = STIM_FIXDOT;
  }
  else if( timesinced / 50 < HZ )
  {
    if( stimulusstate != STIM_REACH )
    {
      statestart = statestartn;
      stateiteration = 1;
      doweflash = rand() / (float)RAND_MAX;
      printf( "%f\n\r", doweflash );
      pos = rand() / (float)RAND_MAX*8;
      stimulusstate = STIM_REACH;
    }
  }
  else if( timesinced / 90 < HZ )
  {
    if( stimulusstate != STIM_LOOK )
    {
      statestart = statestartn;
      stateiteration = 1;
      doweflash = rand() / (float)RAND_MAX;
      printf( "%f\n\r", doweflash );
      pos = rand() / (float)RAND_MAX*8;
      stimulusstate = STIM_LOOK;
    }
  }
  else if( timesinced / 130 < HZ )
```

```
{
  if( stimulusstate != STIM_REACH )
  {
    statestart = statestartn;
    stateiteration = 1;
    doweflash = rand() / (float)RAND_MAX;
    printf( "%f\n\r", doweflash );
    pos = rand() / (float)RAND_MAX*8;
    stimulusstate = STIM_REACH;
  }
}
else if( timesinced / 170 < HZ )
{
  if( stimulusstate != STIM_LOOK )
  {
    statestart = statestartn;
    stateiteration = 1;
    doweflash = rand() / (float)RAND_MAX;
    printf( "%f\n\r", doweflash );
    pos = rand() / (float)RAND_MAX*8;
    stimulusstate = STIM_LOOK;
  }
}
else if( timesinced / 210 < HZ )
{
  if( stimulusstate != STIM_REACH )
  {
    statestart = statestartn;
    stateiteration = 1;
    doweflash = rand() / (float)RAND_MAX;
    printf( "%f\n\r", doweflash );
    pos = rand() / (float)RAND_MAX*8;
    stimulusstate = STIM_REACH;
  }

}
else if( timesinced / 220 < HZ )
{
  stimulusstate = STIM_FIXDOT;
}
else
{
  stimulusstate = STIM_BLACK;
}

QueryPerformanceCounter(&statestartn);

timesince.QuadPart = statestartn.QuadPart - statestart.QuadPart;

timesinced = (double)timesince.QuadPart;

if( timesinced / (PULSE_LENGTH * stateiteration) < HZ || stimulusstate == STIM_FIXDOT )
{
```

```
  }
  else
  {
    pos = rand() / (float)RAND_MAX*8;
    doweflash = rand() / (float)RAND_MAX;
    printf( "%f\n\r", doweflash );
    stateiteration++;
  }

  if( timesinced < HZ * ( TIME_TILL_FLASH + ( PULSE_LENGTH * ( stateiteration - 1 ) ) ) )
  {
    fixdoton = 1;
    targeton = 0;
    fixflash = 0;
  }
  else if( timesinced < HZ * ( ( TIME_TILL_FLASH + FLASH_LENGTH ) + ( PULSE_LENGTH * (
stateiteration - 1 ) ) ) )
  {
    fixdoton = 1;
    targeton = 1;
    fixflash = 1;
  }
  else if( timesinced < HZ * ( ( TIME_TILL_FLASH + FLASH_LENGTH + MEMORY_LENGTH ) + (
PULSE_LENGTH * ( stateiteration - 1 ) ) ) )
  {
    fixdoton = 1;
    targeton = 0;
    fixflash = 0;
  }
  else
  {
    fixdoton = 0;
    targeton = 0;
  }

  glutPostRedisplay();
}

void keyboard( unsigned char key, int x, int y )
{
  int i;

  switch( key )
  {
    case 27:
      exit( 0 );
      break;
    case 'f':
      glutFullScreen();
      break;
    case 't':
      if( testpattern )
        testpattern = 0;
```

```
      else
        testpattern = 1;
      break;
    case 'w':
      glutReshapeWindow ( 250, 250 );
      break;
    case '0':
      QueryPerformanceCounter(&clockcounter);
      stimulusstate = STIM_FIXDOT;
      fixdoton = 1;
      targeton = 0;
      testpattern = 0;
      glutPostRedisplay();
      break;
    case 'z':
      xorigin = 0.0;
      yorigin = 0.0;
      zoomlevel = 0.0;
      dotdistance = 0.0;
      fixdotsize = 0.0;
      break;
    case '+':
      dotdistance = dotdistance + 0.2;
      break;
    case '-':
      dotdistance = dotdistance - 0.2;
      break;
    case '.':
      fixdotsize = fixdotsize + 0.2;
      break;
    case ',':
      fixdotsize = fixdotsize - 0.2;
      break;
    default:
      break;
  }
}

int main( int argc, char** argv )
{
  srand( time( NULL ));
  calibrateclock();

  xorigin = 0.0;
  yorigin = 0.0;
  zoomlevel = 0.0;
  dotdistance = 0.0;
  fixdotsize = 0.0;

  fixdoton = 1;
  targeton = 0;

  testpattern = 0;
```

```
  QueryPerformanceCounter(&clockcounter);
  stimulusstate = STIM_FIXDOT;

  glutInit( &argc, argv );
  glutInitDisplayMode( GLUT_RGB | GLUT_DOUBLE );
  glutInitWindowSize( 250, 250 );
  glutCreateWindow( argv[0] );
  init();
  glutReshapeFunc( reshape );
  glutMotionFunc( motion );
  glutMouseFunc( mouse );
  glutKeyboardFunc( keyboard );
  glutDisplayFunc( display );
  glutIdleFunc( idle_func );
  glutMainLoop();
  return 0;
}
```

APPENDIX B: Image Processing

B.1 SIEMENSMAGNETOMVISION.H

B.1.1 Description

This header file serves as a type descriptor for the commonly encountered Siemens data header present on image files with a IMA extension. It was created by conforming the data descriptors enumerated by David A. Clunie into C language variable types. It is suitable for use in all programs needing to read or write such a data header, such as the automatic analysis program described below.

B.1.2 Use

This code is not executable, and should only be used as a data descriptor.

B.1.3 Code

```
/*
** Copyright 2004 Kyle A. Bernheim, California Institute of Technology
**
** Siemens Magnetom Vision data structure and labels courtesy of
** David A. Clunie and the Medical Image Format FAQ of 6 February, 2001
*/

struct mri_header
{
  u_int   SiemensStudyDateYYYY;
  u_int   SiemensStudyDateMM;
  u_int   SiemensStudyDateDD;
  u_int   AcquisitionDateYYYY;
  u_int   AcquisitionDateMM;
  u_int   AcquisitionDateDD;
  u_int   ImageDateYYYY;
```

```
u_int    ImageDateMM;
u_int    ImageDateDD;
u_int    SiemensStudyTimeHH;
u_int    SiemensStudyTimeMM;
u_int    SiemensStudyTimeSS;
u_int    intunknown1;
u_int    AcquisitionTimeHH;
u_int    AcquisitionTimeMM;
u_int    AcquisitionTimeSS;
u_int    intunknown2;
u_int    ImageTimeHH;
u_int    ImageTimeMM;
u_int    ImageTimeSS;
char   charunknown1[16];
char   Manufacturer[7];
char   charunknown2[2];
char   InstitutionName[25];
char   charunknown3[56];
char   Annotation[4];
char   charunknown4[91];
char   ModelName[15];
char   charunknown5[116];
u_int    LastMoveDateYYYY;
u_int    LastMoveDateMM;
u_int    LastMoveDateDD;
u_int    LastMoveTimeHH;
u_int    LastMoveTimeMM;
u_int    LastMoveTimeSS;
char   charunknown6[332];
char   PatientName[25];
char   charunknown7[2];
char   PatientID[12];
char   charunknown8[1];
u_int    DOBYYYY;
u_int    DOBMM;
u_int    DOBDD;
char   charunknown9[31];
char   PatientAge[3];
char   PatientAgeUnits[1];
char   charunknown10[197];
u_int    RegistrationDateYYYY;
u_int    RegistrationDateMM;
u_int    RegistrationDateDD;
u_int    RegistrationTimeHH;
u_int    RegistrationTimeMM;
u_int    RegistrationTimeSS;
char   charunknown11[468];
double   SliceThickness;
double   doubleunknown1;
double   RepetitionTime;
double   EchoTime;
double   doubleunknown2;
double   doubleunknown3;
```

```
double   FrequencyMHz;
char   charunknown12[39];
char   Station[5];
char   charunknown13[68];
u_int   CalibrationDateYYYY;
u_int   CalibrationDateMM;
u_int   CalibrationDateDD;
u_int   CalibrationTimeHH;
u_int   CalibrationTimeMM;
u_int   CalibrationTimeSS;
char   charunknown14[31];
char   ReceivingCoil[16];
char   charunknown15[45];
char   ImagedNucleus[4];
char   charunknown16[280];
double   FlipAngle;
char   charunknown17[440];
double   MagneticFieldStrength;
char   charunknown18[296];
u_int   DisplayMatrixSize;
char   charunknown19[76];
char   SequencePrgName[65];
char   SequenceWkcName[65];
char   SequenceAuthor[9];
char   SequenceType[8];
char   charunknown20[653];
double   FOVRow;
double   FOVColumn;
double   doubleunknown4;
double   CenterPointX;
double   CenterPointY;
double   CenterPointZ;
double   NormalVectorX;
double   NormalVectorY;
double   NormalVectorZ;
double   DistanceFromIsocenter;
double   doubleunknown5;
double   RowVectorX;
double   RowVectorY;
double   RowVectorZ;
double   ColumnVectorX;
double   ColumnVectorY;
double   ColumnVectorZ;
char   OrientationSet1Top[3];
char   charunknown21[1];
char   OrientationSet1Left[3];
char   charunknown22[1];
char   OrientationSet1Back[3];
char   charunknown23[1];
char   OrientationSet2Down[3];
char   charunknown24[1];
char   OrientationSet2Right[3];
char   charunknown25[1];
```

```
char   OrientationSet2Front[3];
char   charunknown26[1];
char   SequenceName[32];
char   charunknown27[1064];
double   PixelSizeRow;
double   PixelSizeColumn;
char   charunknown28[488];
char   TextPatientID[12];
char   charunknown29[1];
char   TextPatientSex[1];
char   TextPatientAge[3];
char   TextPatientAgeUnits[1];
char   charunknown30[7];
char   TextPatientPosition[7];

char   charunknown31[5];
char   TextImageNumberFlag[5];
char   TextImageNumber[3];
char   charunknown32[10];
char   TextDateDD[2];
char   charunknown33[1];
char   TextDateMM[3];
char   charunknown34[1];
char   TextDateYYYY[4];
char   charunknown35[1];
char   TextTimeHH[2];
char   charunknown36[1];
char   TextTimeMM[2];
char   charunknown37[1];
char   TextAcquisitionTimeFlag[2];
char   charunknown38[4];
char   TextAcquisitionTimeMM[2];
char   charunknown39[1];
char   TextAcquisitionTimeSS[2];
char   charunknown40[13];
char   TextAnnotation[4];
char   charunknown41[50];
char   TextOrganization[25];
char   charunknown42[2];
char   TextStation[5];
char   charunknown43[8];
char   TextAcquisitionMatrixPhase[3];
char   TextAcquisitionMatrixPhaseAxis[1];
char   charunknown44[1];
char   TextAcquisitionMatrixFreq[3];
char   TextAcquisitionMatrixFreqO[1];
char   TextAcquisitionMatrixFreqS[1];
char   charunknown45[1];
char   TextSequence[8];
char   TextFlipAngle[3];
char   charunknown46[1];
char   TextScanNumberFlag[4];
char   charunknown47[1];
```

```
char  TextScanNumberA[3];
char  TextScanNumberB[3];
char  charunknown48[1];
char  TextRepetitionTimeFlag[2];
char  charunknown49[2];
char  TextRepetitionTime[7];
char  charunknown50[1];
char  TextEchoTimeFlag[2];
char  charunknown51[2];
char  TextEchoTime[5];
char  charunknown52[1];
char  TextEchoNumber[1];
char  charunknown53[37];
char  TextSliceThicknessFlag[2];
char  charunknown54[2];
char  TextSliceThickness[7];
char  charunknown55[1];
char  TextSlicePositionFlag[2];
char  charunknown56[2];
char  TextSlicePosition[7];
char  charunknown57[1];
char  TextAngleFlag1[3];
char  TextAngleFlag2[1];
char  TextAngleFlag3[3];
char  TextAngle[4];
char  charunknown58[13];
char  TextFOVFlag[3];
char  charunknown59[1];
char  TextFOVH[3];
char  charunknown60[1];
char  TextFOVV[3];
char  charunknown61[25];
char  TextTablePositionFlag[2];
char  charunknown62[2];
char  TextTablePosition[7];
char  charunknown63[53];
char  TextStudyNumberFlag[5];
char  TextStudyNumber[2];
char  charunknown64[11];
char  TextDOBDD[2];
char  charunknown65[1];
char  TextDOBMM[3];
char  charunknown66[1];
char  TextDOBYYYY[4];
char  charunknown67[25];
char  TextStudyNumberFlag2[3];
char  charunknown68[1];
char  TextImageNumberFlag2[3];
char  TextStudyNumber2[2];
char  charunknown69[1];
char  TextImageNumber2[2];
char  charunknown70[9];
char  TextStudyImageNumber3[5];
```

```
  char   charunknown71[13];
  char   TextModelName[15];
  char   charunknown72[12];
  char   TextPatientName[25];
  char   charunknown73[2];
  char   TextScanStartTimeHH[2];
  char   charunknown74[1];
  char   TextScanStartTimeMM[2];
  char   charunknown75[1];
  char   TextScanStartTimeSS[2];
  char   charunknown76[51];
};
```

B.2 TAGS.C

B.2.1 Description

This application, given its amusing name The Automatic Graduate Student (TAGS) by my predecessor David Dubowitz, came to be the workhorse for processing data from the original Siemens Magnetom Vision scanner commonly used at the Long Beach facility. TAGS provides for the complete automation of image processing from the raw data files provided from the scanner to the creation of AFNI compatible image files. The program first copies all data files from a source location, typically a recordable compact disc, to a local directory then sorts the files by imaging session and sequence type. Common sequence types for anatomical and functional imaging are supported and may be updated if other protocols become commonly used. Image sizes and voxel volumes are automatically computed and used to pass a command to AFNI utilities which register the images and create usable three and four (time-series) dimensioned image files.

B.2.2 Use

After compilation with an ANSI C compiler, invoke TAGS from the command line as follows:

tags [options] inputdir outputdir basesession

Where “inputdir” is the location of source files, “outputdir” is the desired location of processed files, and “basesession” is a time point within functional data to which all other volumes should be registered. Three options are provided to facilitate the subsequent analysis of data. The use of the option “-noaverage” will prevent functional time series from being signal averaged into a separate data file. The use of the option “-noregister” will prevent the three-dimensional volume alignment routine from being invoked. The use of the command “-nosetup” will cause the program to assume that it has already been run once and should not fetch raw data files from the source directory.

To make use of the signal averaging routines, a separate file must be created using the filename “batch.txt” which contains a list of the desired session numbers to be averaged. The format of the file is a simple list of session numbers, one per line, terminated with the number zero on a line by itself, followed by a title for the filename of the averaged data on a line by itself. For example:

1
2
3
0
average_of_three

B.2.3 Code

```
/*
** Copyright 2004 Kyle A. Bernheim, California Institute of Technology
*/

#include <stdlib.h>
#include <stdio.h>
#include <glob.h>
#include <math.h>
#include "SiemensMagnetomVision.h"

#define ReEndianInt( location )  ((( location >> 8  ) & 0x00ff     ) |        \
                                 (( location << 8  ) & 0xff00     ))
#define ReEndianLong( location ) ((( location >> 24 ) & 0x000000ff ) |        \
                                 (( location >> 8  ) & 0x0000ff00 ) |        \
                                 (( location << 8  ) & 0x00ff0000 ) |        \
                                 (( location << 24 ) & 0xff000000 ))

// #define HIRESANAT "/data/harty_anatomical/hartyanathires+orig"

double ReEndianDouble( double wrongendian )
{
  double rightendian;
  char *readptr;
  char *writeptr;
  int ptrloc;

  readptr = (char *)&wrongendian;
  writeptr = (char *)&rightendian;

  for( ptrloc = 0; ptrloc < 8; ptrloc++ )
  {
    writeptr[ ptrloc ] = readptr[ 7 - ptrloc ];
  }
  return rightendian;
}

main(int argc, char *argv[]) {

int i, j, k, l, m;
int patientnumber, firstpatient, lastpatient;
int sessionnumber, firstsession, lastsession;
int scannumber, firstscan, lastscan;
int firstslabimage, lastslabimage;
int sequenceisanat, sequenceexists;
int headersize;
int basesession;
int nosetup, noregister, noaverage;
```

```
double firstslab;
double lastslab;
double xfieldofview;
double yfieldofview;

char buf[65000];
char imalocation[255];
char destlocation[255];
char globarg[255];
char newdirname[255];
char calcfiles[65000];
char calcexpr[65000];
char argument[255];
char argument1[255];
char argument2[255];
char argument3[255];

char zorientfirst, zorientlast;

struct mri_header header;

FILE *fp;

glob_t filelist;

firstpatient = 65000;
firstsession = 65000;
firstscan = 65000;
firstslab = 1000.0;
lastpatient = 0;
lastsession = 0;
lastscan = 0;
lastslab = (-1)*1000.0;
nosetup = 0;
noregister = 0;
noaverage = 0;

sequenceisanat = 0;
sequenceexists = 0;

buf[0] = '\0';
imalocation[0] = '\0';
destlocation[0] = '\0';
globarg[0] = '\0';
newdirname[0] = '\0';
calcfiles[0] = '\0';
calcexpr[0] = '\0';
argument1[0] = '\0';
argument2[0] = '\0';
argument3[0] = '\0';

headersize = sizeof( struct mri_header );
```

```
j = 0;

for( i = 1; i < argc; i++ )
{
  argument[0] = '\0';
  sprintf( argument, "%s", argv[i] );
  if( !strcmp( argument, "-noaverage" ) ) noaverage = 1;
  else if( !strcmp( argument, "-noregister" ) ) noregister = 1;
  else if( !strcmp( argument, "-nosetup" ) ) nosetup = 1;
  else
  {
    if( j == 0 ) sprintf( imalocation, "%s", argv[i] );
    else if( j == 1 ) sprintf( destlocation, "%s", argv[i] );
    else if( j == 2 ) basesession = atoi( argv[i] );
    j++;
  }
}

if( j != 3 )
{
  printf( "\n" );
  printf( "Use: tags [options] inputdir outputdir basesession#\n" );
  printf( "Options: -noaverage  do not perform batch averaging\n" );
  printf( "         -noregister do not register runs w/ 3dvolreg\n" );
  printf( "         -nosetup    do not copy files and create dirs\n" );
  exit(1);
}

if( imalocation[(strlen(imalocation)-1)] != '/' )
{
  imalocation[(strlen(imalocation)+1)] = '\0';
  imalocation[(strlen(imalocation))] = '/';
}

if( destlocation[(strlen(destlocation)-1)] != '/' )
{
  destlocation[(strlen(destlocation)+1)] = '\0';
  destlocation[(strlen(destlocation))] = '/';
}

if( !nosetup )
{
  sprintf( buf, "cp -r %s* %s", imalocation, destlocation );
  system( buf );

  sprintf( buf, "chmod -f 644 %s*", destlocation );
  system( buf );

  sprintf( buf, "mkdir -p %srawdata", destlocation );
  system( buf );

  sprintf( buf, "mkdir -p %srawdata/anatomy", destlocation );
  system( buf );
```

```
  sprintf( buf, "mkdir -p %sraw", destlocation );
  system( buf );

  sprintf( buf, "mkdir -p %savg", destlocation );
  system( buf );

  sprintf( buf, "mkdir -p %sreg-all", destlocation );
  system( buf );

  sprintf( buf, "mv -f %s*.ima %srawdata", destlocation, destlocation );
  system( buf );
}

sprintf( globarg, "%srawdata/*.ima", destlocation );
glob( globarg, 0, NULL, &filelist );

for( i = 0; i < filelist.gl_pathc; i++ )
{
   for( j = ( strlen( filelist.gl_pathv[i] ) - 1 ); j >= 0 &&                \
       filelist.gl_pathv[i][j] != '/'; j-- ) {}
   j++;

   sscanf( &filelist.gl_pathv[i][j], "%d-%d-%d.ima", &patientnumber,         \
         &sessionnumber, &scannumber );

   if( patientnumber < firstpatient ) firstpatient = patientnumber;
   if( sessionnumber < firstsession ) firstsession = sessionnumber;
   if( scannumber < firstscan ) firstscan = scannumber;
   if( patientnumber > lastpatient ) lastpatient = patientnumber;
   if( sessionnumber > lastsession ) lastsession = sessionnumber;
   if( scannumber > lastscan ) lastscan = scannumber;
}

for( i = firstpatient; i <= lastpatient; i++ )
{
  if( !nosetup )
  {
  for( j = firstsession; j <= lastsession; j++ )
  {
    sequenceisanat = 0;
    sequenceexists = 0;

    sprintf( globarg, "%srawdata/%d-%d-*.ima", destlocation, i, j );
    glob( globarg, 0, NULL, &filelist );

    for( k = 0; k < filelist.gl_pathc; k++ )
    {
      for( l = ( strlen( filelist.gl_pathv[k] ) - 1 ); l >= 0 &&         \
            filelist.gl_pathv[k][l] != '/'; l-- ) {}
      l++;

      sprintf( buf, "%srawdata/%s", destlocation,                        \
```

```
            &filelist.gl_pathv[k][l] );

if( ( fp = fopen( buf, "rb" ) ) != NULL )
{
  sequenceexists = 1;

  fread( &header, headersize, 1, fp );
  fclose( fp );
  sscanf( &filelist.gl_pathv[k][l], "%d-%d-%d.ima",              \
              &patientnumber, &sessionnumber, &scannumber );
  if( !strcmp( header.SequenceType, "mpr" ) ||
     !strcmp( header.SequenceType, "fl3d" ) )
  {
    sequenceisanat = 1;
    if( scannumber < 10 )
    {
      sprintf( buf,                                    \
      "mv -f %srawdata/%s %srawdata/anatomy/%d-%d-000%d.ima",\
      destlocation, &filelist.gl_pathv[k][l], destlocation,  \
      patientnumber, sessionnumber, scannumber );
    }
    else if( scannumber < 100 )
    {
      sprintf( buf,                                    \
      "mv -f %srawdata/%s %srawdata/anatomy/%d-%d-00%d.ima", \
      destlocation, &filelist.gl_pathv[k][l], destlocation,  \
      patientnumber, sessionnumber, scannumber );
    }
    else if( scannumber < 1000 )
    {
      sprintf( buf,                                    \
      "mv -f %srawdata/%s %srawdata/anatomy/%d-%d-0%d.ima",  \
      destlocation, &filelist.gl_pathv[k][l], destlocation,  \
      patientnumber, sessionnumber, scannumber );
    }
    else
    {
      sprintf( buf,                                    \
      "mv -f %srawdata/%s %srawdata/anatomy/%d-%d-%d.ima",   \
      destlocation, &filelist.gl_pathv[k][l], destlocation,  \
      patientnumber, sessionnumber, scannumber );
    }
    system( buf );
  }
  else if( !strcmp( header.SequenceType, "mos_lbw" ) )
  {
  }
  else
  {
    sequenceexists = 0;
  }
  if( atof( header.TextSlicePosition ) < firstslab )
  {
```

```
      firstslab = atof( header.TextSlicePosition );
      firstslabimage = scannumber;
    }
    if( atof( header.TextSlicePosition ) > lastslab )
    {
      lastslab = atof( header.TextSlicePosition );
      lastslabimage = scannumber;
    }
  }
}
if( sequenceisanat && sequenceexists )
{
  xfieldofview = atof( header.TextFOVH );
  yfieldofview = atof( header.TextFOVV );

  zorientfirst = header.OrientationSet2Front[0];
  zorientlast = header.OrientationSet1Back[0];

  if( zorientfirst == 'A' ) zorientfirst = 'R';
  if( zorientfirst == 'P' ) zorientfirst = 'L';

  if( zorientlast == 'A' ) zorientlast = 'R';
  if( zorientlast == 'P' ) zorientlast = 'L';


  sprintf( buf, "cat %srawdata/anatomy/%d-%d-* >"                  \
            " %srawdata/anatomy/anat.cat", destlocation, i, j,       \
            destlocation );
  system( buf );

  sprintf( buf, "to3d -anat -2swap -session"                       \
            " %srawdata/anatomy/ -prefix anatomy%d -xFOV %.2fA-P"    \
            " -yFOV %.2fS-I -zSLAB %.2f%c-%.2f%c"                    \
            " 3D:0:%d:%d:%d:%d:%srawdata/anatomy/anat.cat",          \
            destlocation, j, ( xfieldofview / 2 ),                   \
            ( yfieldofview / 2 ), fabs( firstslab ), zorientlast,    \
            fabs( lastslab ), zorientfirst, headersize,              \
            (int)(ReEndianDouble(header.FOVRow)/                     \
            ReEndianDouble(header.PixelSizeRow)),                    \
            (int)(ReEndianDouble(header.FOVColumn)/                  \
            ReEndianDouble(header.PixelSizeColumn)), k,              \
            destlocation );
  system( buf );

  sprintf( buf, "rm -f %srawdata/anatomy/anat.cat", destlocation );
  system( buf );

  sprintf( buf,                                                    \
        "3drefit -xorigin %.2f %srawdata/anatomy/anatomy%d+orig", \
        (fabs( ReEndianDouble(header.CenterPointY) ) +             \
        ( xfieldofview / 2 )), destlocation, j );
  system( buf );
```

```
                sprintf( buf,                                           \
                        "3drefit -yorigin %.2f %srawdata/anatomy/anatomy%d+orig", \
                        (fabs( ReEndianDouble(header.CenterPointZ) ) +          \
                        ( yfieldofview / 2 )), destlocation, j );
                system( buf );

        sprintf( buf, "ln -s ../rawdata/anatomy/anatomy%d+orig.BRIK %savg",\
                j, destlocation );
        system( buf );

        sprintf( buf, "ln -s ../rawdata/anatomy/anatomy%d+orig.HEAD %savg",\
                j, destlocation );
        system( buf );

#ifdef HIRESANAT
        sprintf( buf, "3dvolreg -verbose -twopass -twodup -clipit -base "  \
                        "%srawdata/anatomy/anatomy%d+orig -prefix "          \
                        "%savg/anatomyhires%d %s", destlocation, j,         \
                        destlocation, j, HIRESANAT );
        system( buf );
#endif
      }
      else if( sequenceexists )
      {
        if( basesession == 0 ) basesession = j;

        sprintf( buf, "thorm %srawdata/%d -%d run%d -afni",       \
                destlocation, i, j, j );
        system( buf );

        sprintf( buf, "mv -f %srun%d+* %sraw", destlocation, j,           \
                destlocation );
        system( buf );
      }
    }
    }
    if( !noregister )
    {
    for( j = firstsession; j <= lastsession; j++ )
    {
      sprintf( buf, "3dvolreg -clipit -twodup -prefix"                    \
              " %sreg-all/vol_run%d"                                      \
              " -base '%sraw/run%d+orig[20]' -verbose -Fourier -dfile"     \
              " %sinfo/info_run%d %sraw/run%d+orig",                      \
              destlocation, j, destlocation, basesession, destlocation, j,  \
              destlocation, j );
      system( buf );
    }
    }
/*
** Read Job Control File (batch.txt in destination directory)
**
** Job Control File is composed of a series of numbers, each on its own
```

```
** line, denoting a run number to be included in an averaged dataset
**
** A 0 (zero) denotes the end of a series, the line following the zero
** denotes the name for the dataset
*/
  if( !noaverage )
  {
  sprintf( buf, "%sbatch.txt", destlocation );
  if( ( fp = fopen( buf, "r" ) ) != NULL )
  {
    k = 0;
    m = 1;
    sprintf( calcfiles, "" );
    sprintf( calcexpr, "" );
    sprintf( newdirname, "" );

    while( fgets( buf, 255, fp ) != NULL )
    {
      buf[strlen(buf)] = '\0';

      j = atoi( buf );
      if( j >= 0 )
      {
        if( j == 0 )
        {
          if( fgets( newdirname, 255, fp ) )
          {
            while( ( newdirname[(strlen(newdirname) - 1)]          \
                  == '\n' ) || ( newdirname[(strlen(newdirname)   \
                  - 1)] == '\r' ) )
            {
              newdirname[(strlen(newdirname) - 1)] = '\0';
            }
          }

          if( newdirname == NULL )
          {
            sprintf( newdirname, "noname%d", m );
          }

          sprintf( calcexpr, "\"(" );

          for( l = 1; l < k; l++ )
          {
            sprintf( calcexpr, "%s%c+", calcexpr, (96 + l) );
          }

          sprintf( calcexpr, "%s%c)/%d\"", calcexpr, (96 + l), l );

          sprintf( buf, "3dcalc -verbose -session %savg -prefix"     \
                  " avg_%s %s -expr %s",  destlocation, newdirname,  \
                  calcfiles, calcexpr );
          system( buf );
```

```
          sprintf( buf, "mv -f %sreg %sreg-%s", destlocation,       \
                destlocation, newdirname );
          system( buf );

          k = 0;
          sprintf( calcfiles, "" );
          sprintf( calcexpr, "" );
          sprintf( newdirname, "" );
          m++;
        }
        else
        {
          if( k == 0 )
          {
            sprintf( buf, "mkdir -p %sreg", destlocation );
            system( buf );
          }

          k++;

          sprintf( buf, "ln -s ../reg-all/vol_run%d+orig.HEAD %sreg",\
                j, destlocation );
          system( buf );

          sprintf( buf, "ln -s ../reg-all/vol_run%d+orig.BRIK %sreg",\
                j, destlocation );
          system( buf );

          sprintf( calcfiles, "%s -%c %sreg/vol_run%d+orig",        \
                calcfiles, (96 + k), destlocation, j );
        }
      }
    }
  }
  }
}
```